The Eyeball ROV: An Underwater Remotely Operated Vehicle Featuring Advances in Rotational Actuation, Communication, and Localization

by
Ian Charles Rust

B.S., Mechanical Engineering, Massachusetts Institute of Technology, 2010

Submitted to the Department of Mechanical Engineering in Partial Fulfillment of the Requirements for the Degree of

Master of Science
in
Mechanical Engineering

at the

MASSACHUSETTS INSTITUTE OF TECHNOLOGY

September 2011

Signature of Author.....
Department of Mechanical Engineering
August 5, 2011

Certified by .....
H. Harry Asada
Ford Professor of Mechanical Engineering
Thesis Supervisor

Accepted by .....
David E. Hardt
Chairman, Department Committee on Graduate Studies
Department of Mechanical Engineering

The Eyeball ROV: An Underwater Remotely Operated Vehicle Featuring Advances in Rotational Actuation, Communication, and Localization

by

Ian Charles Rust

Submitted to the Department of Mechanical Engineering
on August 5, 2011 in Partial Fulfillment of the
Requirements for the Degree of Master of Science in
Mechanical Engineering

ABSTRACT

The design for a spherical Remotely Operated Vehicle (ROV) with a camera, called the Eyeball ROV due to motions similar to the human eye, is presented in this thesis. The ROV features an actuation scheme that utilizes a two-axis gimbal for changing the location of the center of mass of the ROV. This creates continuous and unlimited rotations in place on the part of the ROV, allowing the camera to be panned and tilted. A model of the ROV is presented, and control was tested in both simulation and experiments. In addition, a dual-use system for both communication and localization of the ROV is presented. This novel dual-use system uses visible blue light (~470nm) to relay data in addition to providing a beacon with which the orientation and position in space of the ROV was estimated. This localization algorithm was implemented using an Extended Kalman Filter (EKF), and was tested in both simulations and experiments.

Thesis Supervisor: H. Harry Asada
Title: Ford Professor of Mechanical Engineering

Acknowledgments

I would firstly like to thank Mitsubishi Heavy Industries, and my contact there, Mr. Jun Fujita, for funding the research presented in this thesis.

I would also like to thank Professor H. Harry Asada for his guidance in completing this thesis. We have had an academic relationship since my time as an undergraduate, and I have found no one better to help me shape my ideas into reality. Several undergraduate students have also helped with various portions of this project, so I would like to thank both Ashley Fletcher and Hellen Lopez for their invaluable help.

In addition, I would like to like to thank my parents, Greg and Kathleen Rust. From an early age they taught me the importance of clear and logical thought, the value of intellectual creativity, and the importance of dedication and hard work. Without such lessons, constant words of encouragement, and equally constant boxes of cookies sent through the mail, I would doubtlessly not have been as well equipped to perform the presented research.

Lastly, I would like to thank Karen Dubbin for reminding me of the reason why I spent all those late nights working and the reason why I came home at the end of them.

Table of Contents

List of Figures

List of Tables

Chapter 1

Introduction

1.1. The Need for Inspection of Nuclear Reactors

Nuclear energy has gained prominence as a possible short term solution to the building energy crisis. Because of this, the amount of power supplied by nuclear power, i.e. nuclear capacity, is expected to grow at a rate of 2.3% from now until 2030 [1]. In addition, there already exist more the 400 nuclear reactors worldwide. More than 100 of these are in the United States. These statistics alone highlight the need for stringent safety measures to be taken during the operation of these reactors. However, with the recent disaster in Fukushima, the question of the safety of nuclear power has been thrust into the world's attention, and the need for advanced safety methods and standards has become apparent. In addition, according to the US Nuclear Regulatory Commission 52 of the approximately 100 reactors in the US are more than 30 years old [2]. As such, it can be concluded that there is a wide need for these advanced safety methods and standards in the United States. For a map showing the location and ages of these reactors, refer to Figure 1 [2].

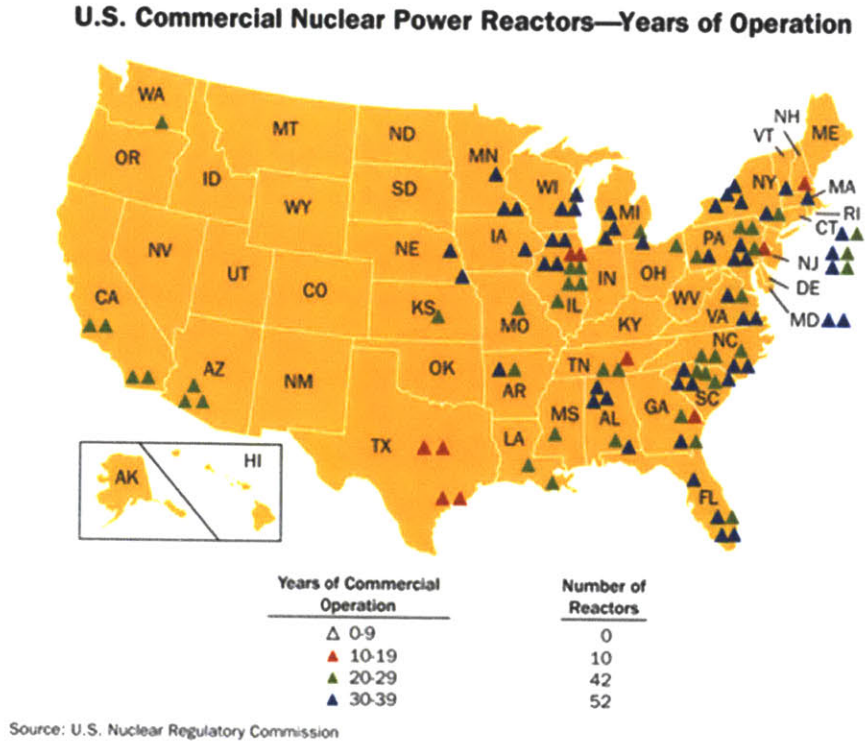

Figure 1 – Map of the United States, with the locations and ages of Nuclear Reactors marked [2].

With so many aging reactors and the memory of the tragedy in Fukushima, the need for regular inspection of reactors is apparent. In this thesis, we present a mobile underwater robot for use in the inspection of the primary cooling cycle of Pressurized Water Reactors, a common form of nuclear reactor.

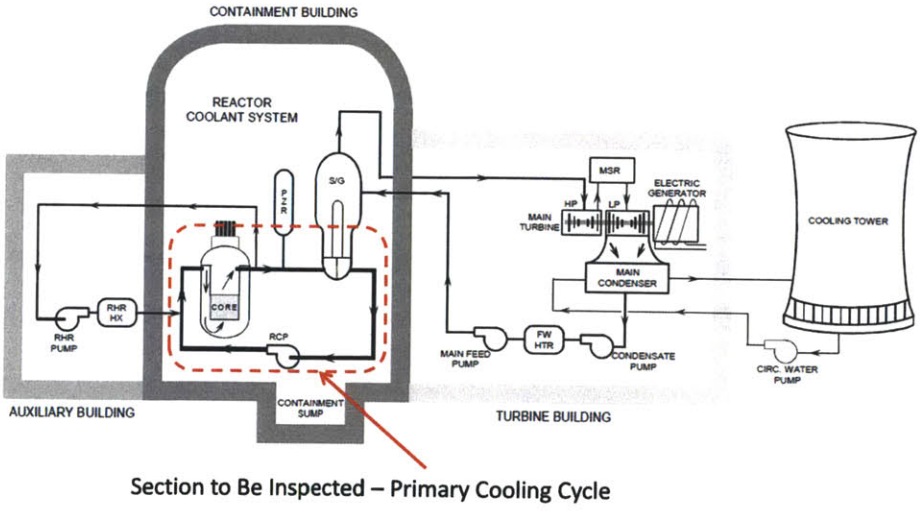

Figure 2 - Diagram of a Pressurized Water Reactor (PWR). Note that the section of the reactor to be inspected, namely the primary cooling cycle, is circled [3].

1.2. Inspection Strategies

Because the entire environment inside the reactor is filled with water, regular inspection necessitates one of three strategies. One would be that the reactor is drained, and human inspectors check for corroded weld lines, broken sensors, etc. This is an undesirable option, since the reactor is irradiated, even after the water is drained. In addition certain parts are too small in geometry or otherwise physically inaccessible by humans. For example, some sections of pipe are completely buried, are highly susceptible to corrosion, and need regular maintenance and inspection [4], [5]. Also, draining the reactor would cause lengthy downtimes in the reactors operation, something that is unacceptable with growing power demands.

The other option would be to implement non-invasive, imaging based inspection strategies. At the moment, current strategies include ultrasonic imaging, eddy current imaging, infrared thermal imaging, and voltage gradient tests [6], [7], [8]. However, some of these strategies require removal of insulation around piping as well as other destructive procedures which increase downtime of the reactor [6]. In addition, these strategies do not offer a direct image from inside the pipe and of the inspection sites but rather extrapolated images based on the algorithms for interpreting the signals from the ultrasonic transducers, eddy current sensors, etc.

The last option, which the robot in this thesis is designed for, is that of robotic inspection. If inspection is done using an underwater robot, then the reactor would not have to be drained. This would allow for quicker, more frequent inspections. As an added advantage, a sufficiently small and agile enough robot would be able to navigate the small piping systems inaccessible to humans. There are some existing robotic strategies for inspection of nuclear reactors. These include wall climbing robots [9], [10], snake-like wheeled robots [11], robots that climb on the outside of the piping system [12], wheeled robots that inspect the outer structures of the reactor, and multi-linkage arm robots [13].

However, these lack the mobility of an underwater robot. In this way, an underwater Remote Operated Vehicle (ROV) is an ideal candidate for the inspection of this hazardous, complex environment. Using this application as a motivation for the research presented in this thesis, we present a design for a spherical ROV with an attached camera for visual inspection. The motions of the vehicle, turning in place to point the camera at different inspection items, are reminiscent of the human eye. As such it is called the Eyeball ROV.

There are some existing ROV's for inspection of nuclear reactors. These include the Kepro VT ROV [14], the Yamamoto ROV [15], and the URSULA ROV [16], as examples. These ROVs are all tethered, however, and feature external geometries and actuation schemes that would make maneuvering through piping systems overly complex. The Eyeball ROV features a simple yet safe and effective design and actuation scheme, as well as an untethered communication architecture. As such, it is an improvement on previous ROV designs.

1.3. Outline of the Work Presented

First, the mechanical design for this ROV is presented in this thesis. The primary focus of this study is the orientation actuation. This is done using what will be named an Eccentric Mass Steering System, the details of which will follow in the sections to come. In addition, we present a simplified dynamic model for this vehicle, which allows us to make accurate simulations of the vehicle. Feedback control is also applied in both experiment and simulation.

Once the mechanical design, modeling, and control are presented, the strategies for wireless communications between the ROV and distal operator are explored. This is a particularly important exploration, since wireless underwater communications are somewhat of an unsolved problem, with radio communications being handicapped in terms of range and acoustic communications handicapped in terms of bandwidth (the two most prominent forms of wireless communication). For this reason, a study of visible light communications is made, as visible light systems are shown to be capable of both extended ranges (~40m) as well as high bandwidths (~1Gbps) [17].

The main contribution of this study however, lies not with the communication system itself. This field, over the past several years, has been studied extensively [17], [18], [19], [20], [21]. Instead this thesis presents a novel scheme for a system that allows for both communication and localization of the ROV. As such it is a dual use system. The localization algorithms presented use the visible light signal itself to gain information about the position and orientation of the ROV in space, using parameters such as signal strength and orientation sensors in the form of photodiode arrays. This is important due to the reliance of these visible light communications on line of sight and "aiming" of the light-emitting transmitter and photodetector receiver. In

addition, the localization of mobile robots in general has many applications as an important component of feedback control. This work, then, seeks to improve upon existing visible light communication systems by providing a feedback signal of the position and orientation (i.e. localization) of the ROV. This would allow for feedback control of the "aiming" of the components of the communication system, thus creating a more reliable data link with a distant receiver.

With these two bodies of research, the mechanical design, modeling, and control as well as the visible light communication and localization algorithms, we present a technological foundation for a wireless underwater ROV for use in nuclear reactor inspection. The applications of the technologies presented are wide, however. They can be applied to any underwater robot with need of robust wireless communication and agile maneuvering and orientation control.

Chapter 2

The Eyeball ROV

2.1. Design Requirements

The ROV presented in this thesis is designed to navigate the complex environment of a nuclear reactor and the associated piping systems associated with the primary cooling cycle. As its primary functional requirement, the ROV must be able to navigate through both the reactor and associated piping systems and gather visual inspection data of certain key components, including weld lines, which are susceptible to corrosion, and temperature and pressure sensors, which are equally vulnerable to failure. As such, any robot designed to carry out this task must be able to position a camera in order to capture video of these inspection items. These items can be on the top, bottom, and sides of the pipe, and thus the ROV must be able to point the camera in a wide variety of directions in an agile and stable manner.

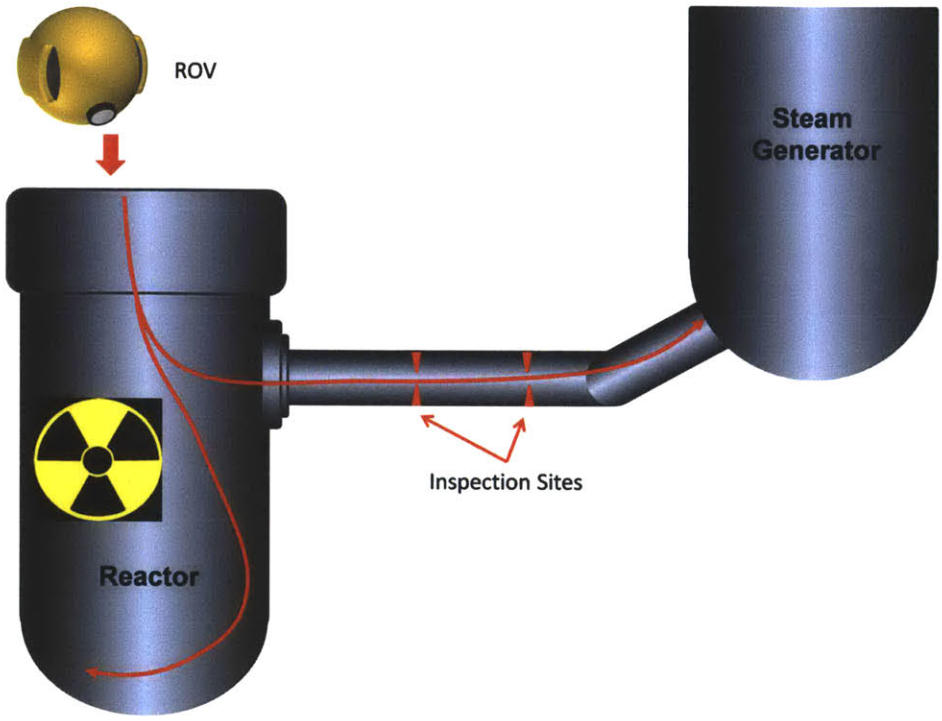

Figure 3 - Diagram detailing the general inspection task undertaken by the ROV. It must swim through both the reactor and associated piping systems in order to acquire video data of various inspection sites.

The workspace of the ROV, the reactor and various associated piping systems, is a complex environment. This complexity arises from a variety of factors. Firstly, the diameters of the piping systems are small, on the order of 80cm. As such, a robot must be sufficiently small and agile enough to navigate the small pipes and tight turns of the piping system. In addition, these piping systems have numerous sensors for monitoring the state of the reactor protruding into the pipe. These sensors, along with being points of inspection, are also obstacles to be avoided during inspection.

Any sort of contact with these sensors risks damaging the sensors. Damage to the sensors would be far more costly than a single inspection, since it would require replacement of the sensor, something that would mean extended reactor downtime. Because of this it is important for the external geometry of the vehicle to be completely smooth and unobtrusive, as to not catch on or interfere with protruding sensors. This also prohibits the use of a tether for communication with the operator, since this tether could wrap around or otherwise disturb the fragile sensors in the pipes. Wireless communication, then, must be used in order to remove the need of the tether.

In addition, the movements of the ROV must be controlled to minimize potential contact with these sensors. What is meant by this is that the robot must be able to move a camera through the pipes and capture video inspection data for the operator. In these motions, specifically the positioning and pointing of the camera to inspect various elements, the robot must have a minimal chance to contact the protruding sensors.

The final requirement of the robot would be overall reliability. Two common failure modes are actuator failure and battery failure. The robot design must be one that maximizes efficiency in order to extend battery life. The design should also reduce the number of actuators, in order to reduce the likelihood of actuator failure. As an added note, a reduced number of actuators help with the overall monetary cost of the ROV. This is important due to the fact that the ROV is moving through an irradiated environment, and must be disposed of after every inspection. Therefore, a simple and inexpensive ROV would be ideal to make regular inspection an affordable course of action for reactor operators.

Therefore, the design of this ROV has several functional requirements:

1. A simple external geometry for avoidance of protruding obstacles in the workspace (such as sensors).
2. Pan and tilt motion for the camera fixed to the body of the ROV.
3. Limited actuator numbers, for increased reliability.
4. A small form factor for accessibility of narrow channels and complex structures (i.e. <20cm diameter).
5. Total system simplicity to increase reliability and decrease cost (the ROV is to be disposable).

The design proposed seeks to meet these requirements.

2.2. Mechanical Design

In order to meet the design requirements for this underwater ROV, we propose a spherical ROV, with a camera fixed to the outer hull of the vehicle. The spherical shape allows for rotational motions to be made without changing the space occupied by the vehicle (turning in

place). This ability to turn in place allows for the operator to "look" with the camera in any direction by moving the vehicle as a whole, much like the motion of an eyeball. The name of the ROV, the "Eyeball ROV" follows directly from this feature. For a visual explanation of the motions of the ROV, see Figure 4.

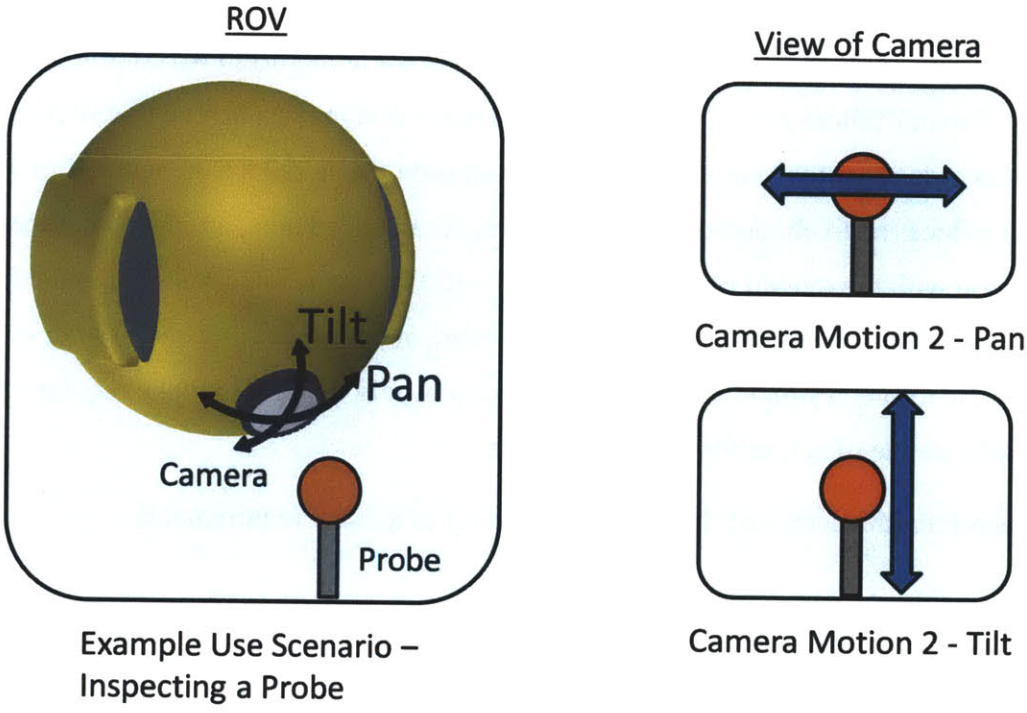

Figure 4 - Demonstration of the two required camera motions, Pan and Tilt.

This ability to point the camera in any direction could not be achieved by using a servo-positioned camera on a stationary ROV, since the orientation range of the camera would be constrained by the mechanical range of motion of the servo mechanism, creating blind spots. With the Eyeball ROV, rotations of the ROV can carry on continuously, allowing for the camera to be pointed in an arbitrary direction. With a simple servo-actuated camera aboard a conventional ROV, there is a more complex relationship between coarse and fine positioning of the camera. Fine positioning of the camera is done simply with the servo mechanisms. However, if large changes in orientation are required, the robot itself must be moved. By eliminating this hybrid positioning scheme with a scheme in which the ROV and camera are rotated as one, increased range of camera motion, mechanical simplicity, and more direct mapping of operator pan and tilt commands are gained.

Most importantly, a spherical outer shape and the ability to turn in place contribute to the ability of the vehicle to avoid collisions with protruding obstacles and sensors. This is because a spherical outer shape is rotationally symmetric about any-axis. This means that in any arbitrary rotation, without any translation (turning in place), the robot will occupy the same volume in space. This is important, because this means that in any rotation, the ROV stands no risk of colliding with obstacles unseen by the camera. This is not the case for any other external geometry, and as such a spherical outer shape is optimal for this application.

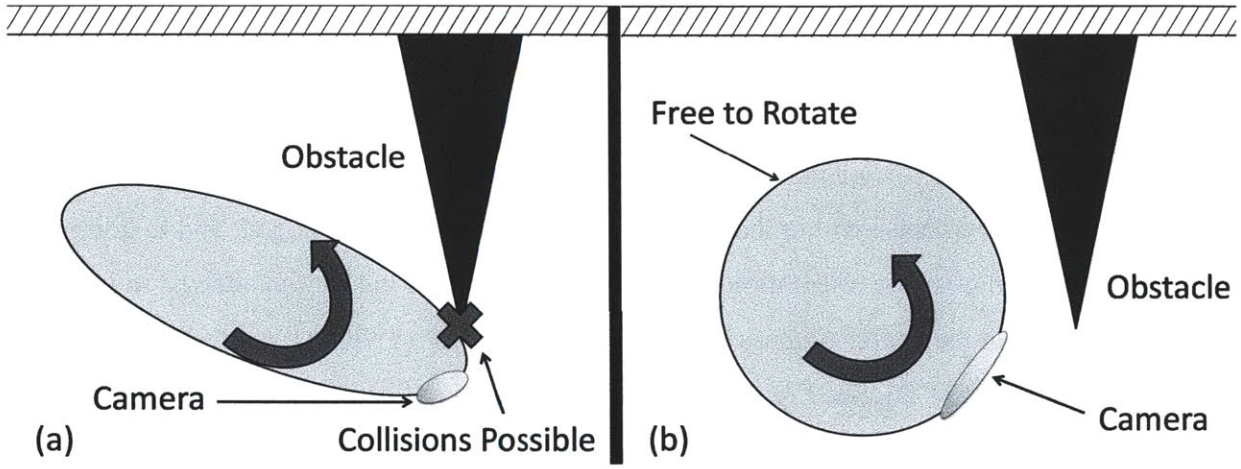

Figure 5 - Illustration of the collision avoidance advantages of a spherical ROV. With a camera fixed to the body of the ROV, a non-spherical vehicle (in (a)) can collide with unseen obstacles. However, a spherical vehicle (in (b)) can turn in place with no danger of collision.

A spherical outer shape is a trivial feature to enact in a mechanical design. The ability to turn in place, however, is complex, and there are many possible methods to enact these sorts of motion. In this thesis, we present an actuation scheme which results in an ability to turn in place using not only a minimal number of actuators, but also with actuators entirely internal to the vehicle. This is done through the use of hydrostatic effects, specifically in the way that the center of buoyancy and center of mass of a body interact when submersed in a fluid, in this case water. If the cumulative effects of the hydrostatic force on the surface of the vehicle are reduced to a single force vector, the point at which this force would act is defined as the center of buoyancy. This point is defined as such:

$$\vec{r}_{cm} = \frac{\oint_A \vec{r}_A P \bullet d\vec{A}}{F_B} \tag{1}$$

In this equation, P is the external pressure on the body, $d\vec{A}$ is an infinitesimal area onto which this pressure is acting to create a force, $\vec{r}_A$ is the vector to each of these sections, and F_B is the total buoyant force (defined as $\oint_A P \bullet d\vec{A}$).

For a spherical body, the center of buoyancy is always at the center of that sphere. By placing a center of mass eccentric to the center of the sphere, we can then produce a stable orientation for the ROV. This is because the center of mass (when the body is completely submerged) of a body will always provide what is called a "righting moment" to the body, coercing the body to keep the center of mass below the center of buoyancy. By changing the location of the center of mass within the body, this stable point can be changed, and in doing so we can enact control over the orientation of the vehicle, as well as the camera affixed to it. This is done by displacing the center of mass of the vehicle (CM) from a vertical centerline through the center of buoyancy (CB). See Figure 6a. As a result of this deflection, the ROV rotates counteractively to this deflection, with the center of mass eventually aligning with the vertical centerline. See Figure 6b. This occurs with minimal net force, assuming the buoyant force and weight of the vehicle are equivalent. Figure 6 shows the effects of a deflection about the *y*-axis, which produces a moment about the same axis (the pitch axis). A moment can also be produced about the *x*-axis by inducing a deflection about the *x*-axis (the roll axis). However, there is no way for a moment to be produced about the z-axis.

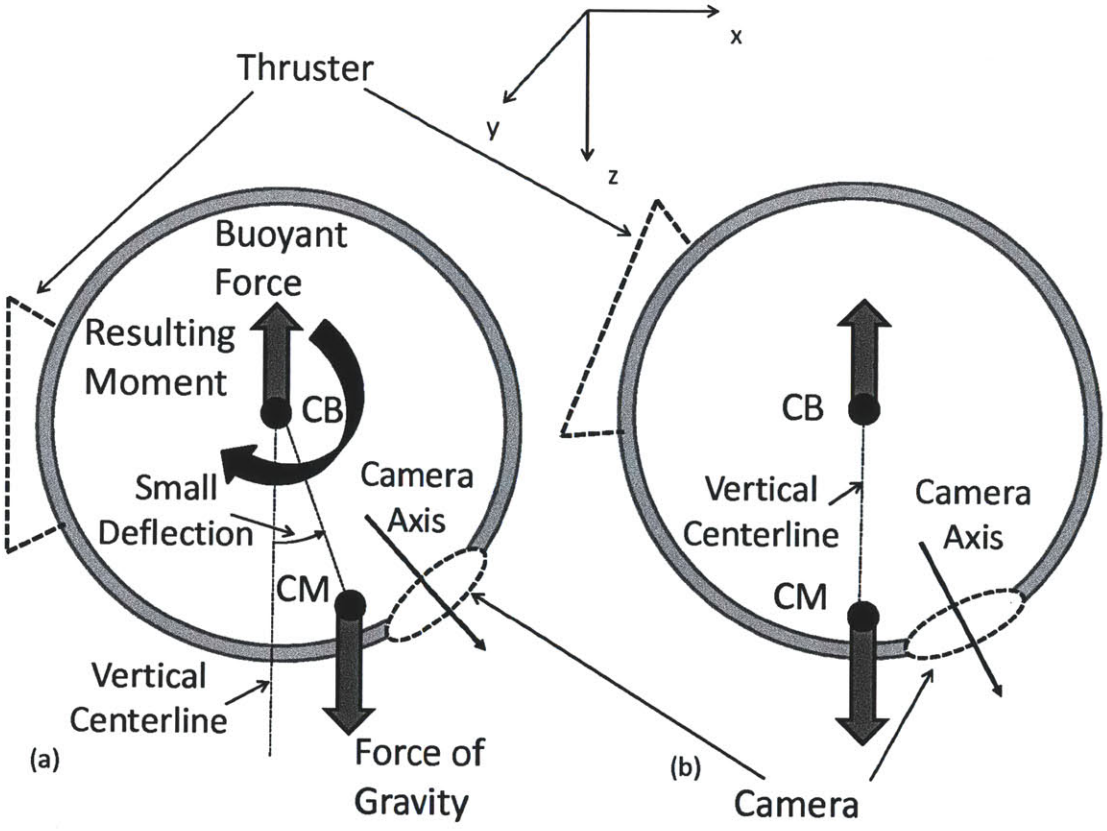

Figure 6 - Moment produced by small deflections of an eccentric center of mass from the vertical centerline and resulting orientation change. Note that no net force is produced, because the ROV is assumed to be neutrally buoyant.

In order to enact this movement of the center of mass of the vehicle, a two-axis gimbal is placed in the center of the vehicle. A large steel mass is in turn placed eccentrically in this mechanism. With this, the center of mass can be placed in any arbitrary configuration.

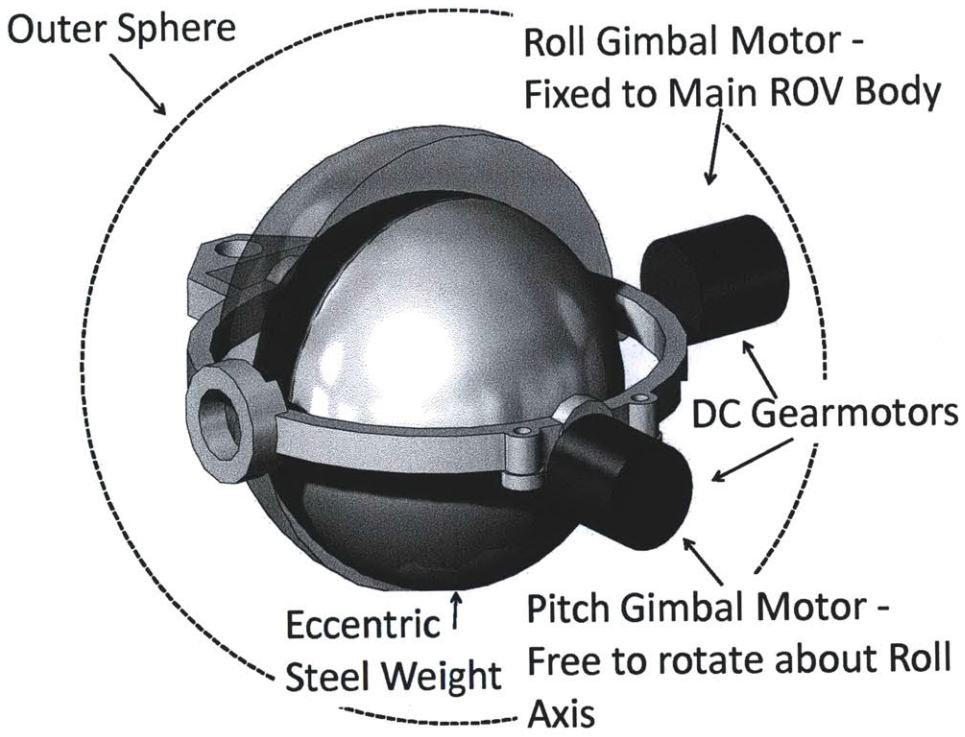

Figure 7 - Two-axis gimbal used for changing the location of the center of mass of the ROV. This is done by moving a large steel weight, eccentrically placed, with a two axis gimbal. This is actuated using two DC motors.

This strategy of shifting an internal mass in order to enact orientation control has been used in several other applications. Firstly, it has been used in several spherical ground vehicles in order to roll the vehicles [22], [23]. A more similar application is in underwater gliders. A common method of pitch and roll control in these gliders is to shift the mass of the battery pack of the vehicle in order to the pitch the glider up or down to dive or roll the vehicle left or right to turn in either direction. These gliders include the SLOCUM, Spray, and Seaglider gliders [24], [25], [26]. The key differences between the actuation strategy in these gliders and the design presented in this thesis include the fact that the Eyeball ROV is capable of unlimited rotations due to the ability for unlimited rotations on the part of the 2-axis gimbal. These gliders are severely limited in terms of the range in which they are capable in pitching and rolling, due to mechanical limits in the battery-shifting mechanisms. Lastly, the Eyeball ROV is capable of turning in place. The control moments provided by the gimbal are essentially uncoupled to a translational force. Underwater gliders require some forward velocity in order to create lift, and as such the control moments provided are coupled to forward motion.

In order to control pan and tilt motion of the camera in any orientation, three moments are needed. This is because the two moments produced by the eccentric mass are fixed in the inertial frame. For an explanation of the frames of reference used in this thesis, refer to Figure 10 (found later in this thesis). Only when pan and tilt rotations are identical to inertial roll and pitch rotations will these two moments alone suffice. Thus, a third moment in the yaw direction is missing.

However, yaw motion in the inertial frame is exceedingly complex to control using the moments about the pitch and roll axes [27]. To create this moment an array of two thrusters is used (shown in Figure 8).

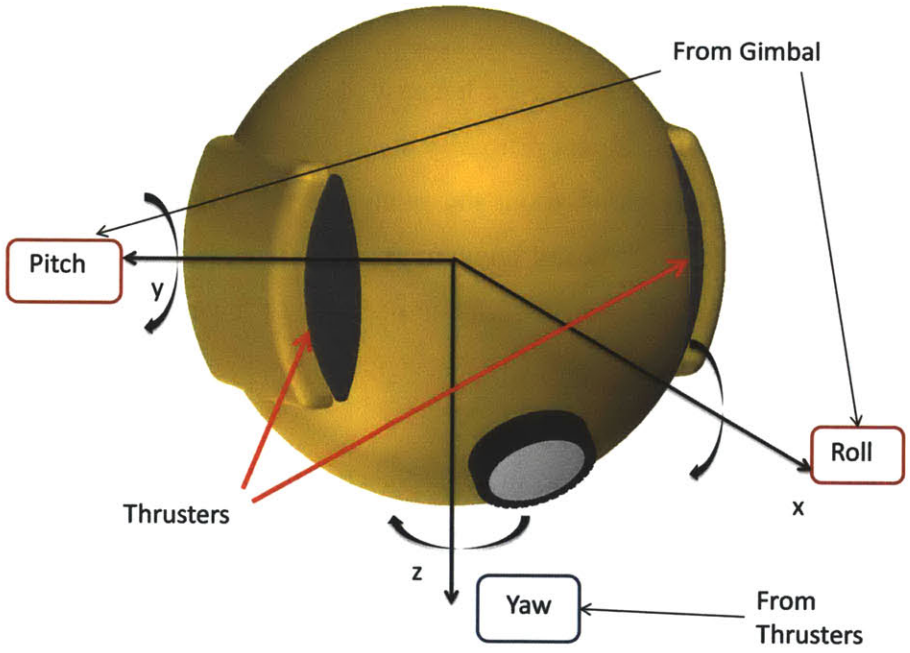

Figure 8 - Diagram of the moments provided by the outboard thrusters and internal gimbal. Note that the gimbal provides moments in the x and y directions (roll and pitch), and the thrusters provide a moment in the z direction (yaw).

This also provides the necessary linear force for translation in the forward direction (the surge direction). Thus, a combination of moments from the eccentric mass and pair of thrusters is used to control pan, tilt, and forward motion.

An advantage of the internal eccentric mass is that it contributes to reliability since fewer actuators are used to produce moments, as compared to conventional thrusters. For normal

propellers or water jet thrusters, one actuator can be used to induce a moment. However, this moment will be coupled to a linear force. Two thrusters must be used to produce one moment uncoupled from translation. The gimbal mechanism presented can produce two uncoupled moments using two actuators, in this case two DC motors. Using fewer actuators creates a more robust design, since there will be a smaller opportunity for actuator failure.

In regard to creating a small form factor for accessibility of narrow channels and complex structures, this design has the feature of being highly scalable in terms of physical dimensions. The current design features an external diameter of approximately 12cm. While adequate, this can be improved upon easily by merely scaling the internal gimbal mechanism.

In summary, this design will have the following salient features:

1. Passive collision avoidance behavior because of a simple spherical shape.
2. Pan and tilt control of a camera primarily using actuators internal to the vehicle.
3. Passively stable orientations about the pitch and roll axes from eccentricity of the center of mass from the center of buoyancy.
4. Increased reliability and lower cost due to presence of few actuators.
5. A readily scalable design.

As an added note, this design results in an underactuated ROV. While translations in the sway (y direction) and heave (z direction) directions in the body-fixed frame are not actuated, rotations in place can be made to "point" the ROV in any direction, and then move forward. However, as analysis presented later in this thesis shows, these directions experience minimal force as well. As such, the vehicle can be seen as essentially a non-holonomic one, constrained to move only back and forth in one direction, but able to change that direction. This is exceedingly similar to the way a wheeled vehicle is non-holonomic.

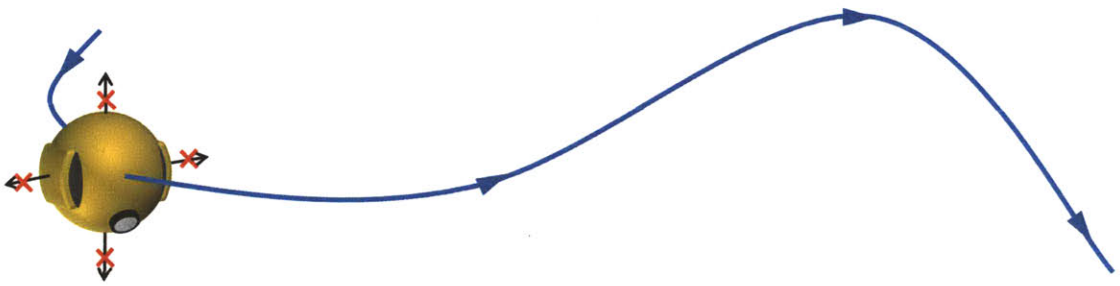

Figure 9 - The Eyeball ROV as a non-holonomic ROV, allowed to rotate about any-axis and only able to translate in the x direction.

2.3. Dynamic Modeling

In order to begin modeling the dynamics of this design, we must define two frames of reference. The first is the body-fixed frame, which is fixed to the robot itself. The origin of this frame is coincident with the center of buoyancy of the body, and as such is coincident with the center of the sphere that defines the outer shape of the ROV. The other frame is the inertial frame.

With these frame defined, we can define the states of the vehicle. $\boldsymbol{\nu} = [u \quad v \quad w]^T$ is defined as the linear velocities of the vehicle in a coordinate frame fixed to the vehicle (the body-fixed frame), and $\boldsymbol{\omega} = [p \quad q \quad r]^T$ is defined as the angular velocities (in the pitch, roll, and yaw directions) of the vehicle in the same frame.

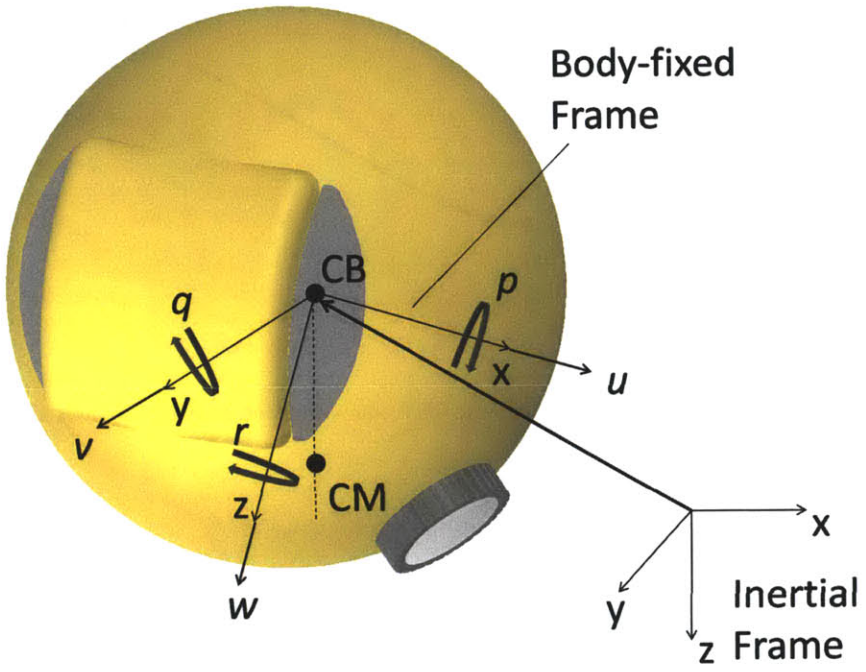

Figure 10 - Choice of reference frames. The body-fixed frame is fixed to the body such that the thrusters "point" in the *x* direction. Note that the body-fixed frame is centered upon the center of buoyancy (i.e., the center of the sphere).

Ignoring hydrodynamic effects, the equations of motion are given by [28], [29]:

$$\begin{bmatrix} mI_{3x3} & ms(r_c^b) \\ ms(r_c^b) & R_e^b J\left(R_e^b\right)^T \end{bmatrix} \begin{bmatrix} \dot{\nu} \\ \dot{\omega} \end{bmatrix} + \begin{bmatrix} ms(\omega) & 0 \\ ms\left(r_c^b\right)s(\omega) & s(\omega)R_e^b J\left(R_e^b\right)^T \end{bmatrix} \begin{bmatrix} \nu \\ \omega \end{bmatrix} = B_1\tau_1 \qquad (2)$$

The dynamics are derived assuming a non-rigid body due to the fact that the center of mass moves within the body. This causes the inertia, along with other terms, to no longer be constant. The assumption is made that the deflections of the center of mass are small enough that the center of mass can be modeled as remaining on the vertical centerline. This simplifies the dynamics in order to facilitate the study of the system. It does so by removing the angles of the gimbal relative to the body of the ROV as system states. Because this assumption ignores the inertial effects of making small deflections from the vertical centerline, gimbal motor torques are included in τ_1 as if they were external torques.

In the equations of motion, m is the mass of the ROV and $J = diag\left(\begin{bmatrix} J_x & J_y & J_z \end{bmatrix}\right)$ is the inertia matrix of the ROV in the inertial frame. The inertia matrix is in the inertial frame

because the center of mass will always be almost directly vertically below the center of buoyancy in the inertial frame (ignoring the small deflections used to control the ROV). In addition, this inertia matrix does not take into account the rotations of the inner weight that is moved by the 2-axis gimbal. This is once again because of the assumption that the center of mass of the vehicle is always inertially downward prohibits rotations of the inner mass, making any rotational inertial contributions inconsequential.

Additionally, B_1 is the input matrix, and τ_1 is the control input (a detailed definition of this control input will be defined in full later in this thesis). $s(c)$ is a cross product matrix defined as:

$$s(c) = \begin{bmatrix} 0 & -c_3 & c_2 \\ c_3 & 0 & -c_1 \\ -c_2 & c_1 & 0 \end{bmatrix} \tag{3}$$

where $c = [c_1 \quad c_2 \quad c_3]^T$ is an arbitrary vector (e.g., $\omega \times v = s(\omega)v$). This is useful because it allows for a cross product to be reduced to matrix multiplication.

Assuming that the center of mass always stays vertically downward in the inertial frame, $r_c^{\,b}$, the location of the center of mass in the body-fixed frame, is defined as such [29]:

$$r_c^{\,b} = R_e^{\,b} r_c^{\,e} \tag{4}$$

The position vector of the center of mass used in (2) and (4) is:

$$r_c^{\,e} = [0 \quad 0 \quad L] \tag{5}$$

where L is the distance from the center of mass to the center of buoyancy. For the dynamics, this vector is assumed to be constant (assuming small control deflections used to induce moments).

$R_e^{\,b}$ is a rotation matrix from the inertial frame to the body-fixed frame [17].

$$R_e^{\,b} = \begin{bmatrix} c_\psi c_\theta & s_\psi c_\theta & -s_\theta \\ -s_\psi c_\phi + c_\psi s_\theta s_\phi & c_\psi c_\phi + s_\psi s_\theta s_\phi & s_\phi c_\theta \\ s_\psi s_\phi + c_\psi s_\theta c_\phi & -c_\psi s_\phi + s_\psi s_\theta c_\phi & c_\phi c_\theta \end{bmatrix} \tag{6}$$

where c_x and s_x refer to $\cos(x)$ and $\sin(x)$, respectively. All angles are Euler angles representing the orientation of the body-fixed frame in the inertial frame. They are defined in the following table in relation to the states of the vehicle defined previously.

Table 1 - Vehicle states

Body-Fixed Axis	Orientation Angle	Rotational Velocity		Linear Velocity	
x	ϕ	u	Roll	p	Surge
y	θ	v	Pitch	q	Sway
z	ψ	w	Yaw	r	Heave

The equations of motion are then reduced to the following linear form for simplicity:

$$M_{ne}\dot{V} + C_{ne}V = B_1\tau_1 \tag{7}$$

where $V = \begin{bmatrix} \nu^T & \omega^T \end{bmatrix}^T$.

Hydrodynamic effects must be considered as well. Firstly, an added mass matrix, M_a, must be added to the mass matrix M_{ne}. In addition, there is an added mass centripetal matrix C_a, a drag matrix D_{drag}, and a lift matrix D_{lift}, which all must be added to C_{ne}. These additional hydrodynamic matrices are defined below. Note that for a spherical body all added mass terms are equal to 50% of the mass of the fluid displaced by the body [29], [30].

$$M_a = \frac{1}{2}\rho \not{V} \cdot diag\left(\begin{bmatrix} 1 & 1 & 1 & 0 & 0 & 0 \end{bmatrix}\right) \tag{8}$$

$$C_a = \frac{1}{2}\rho \not{V} \begin{bmatrix} 0_{3\times3} & s(\nu) \\ -s(\nu)^T & 0_{3\times3} \end{bmatrix} \tag{9}$$

$$D_{drag} = \frac{1}{2}\rho A \cdot diag\left(\begin{bmatrix} c_{d,lin} & c_{d,lin} & c_{d,lin} & c_{d,rot} & c_{d,rot} & c_{d,rot} \end{bmatrix}\right) \tag{10}$$

$$D_{lift} = \frac{1}{2}\rho A c_{lift} \begin{bmatrix} s(\omega) & 0_{3\times3} \\ 0_{3\times3} & 0_{3\times3} \end{bmatrix} \tag{11}$$

In these, $\not{V}$ is the volume of the ROV, ρ is the density of water, $c_{d,lin}$ is the linear damping coefficient, $c_{d,rot}$ is the rotational damping coefficient, and c_{lift} is the lift coefficient [29], [31]. With these hydrodynamic effects considered, the dynamics become:

$$M_T\dot{V} + C_T V = B_1\tau_1 \tag{12}$$

where $M_T = M_{ne} + M_a$ and $C_T = C_{ne} + C_a + D_{drag} + D_{lift}$.

2.3.1. Gravitational Forces

Gravitational forces contribute to the dynamics of the system due to the displacement of the center of mass. This is ignored for the initial formulation of the dynamics of the vehicle, however since it does provide a control moment, we model the effects of gravity as an external moment, and thus is treated as a control input. This moment is defined as $T_c^{\,b}$, which is calculated in the following manner:

$$T_c^{\,b} = R_e^{\,b} \cdot W \times \left(\left(R_e^{\,b}\right)^{-1} R_m^{\,b} r_c^{\,m}\right) \tag{13}$$

In this, the rotation matrix $R_m^{\,b}$ is used to transform the position of the center of mass relative to the gimbal motors ($r_c^{\,m}$) into the body-fixed frame. It is defined as:

$$R_m^{\,b} = \begin{bmatrix} c_{\theta_c} & s_{\theta_c} s_{\phi_c} & s_{\theta_c} c_{\phi_c} \\ 0 & c_{\phi_c} & -s_{\phi_c} \\ -s_{\theta_c} & c_{\theta_c} s_{\phi_c} & c_{\theta_c} c_{\phi_c} \end{bmatrix} \tag{14}$$

In this equation, ϕ_c is the roll gimbal motor position, and θ_c is the pitch gimbal motor position. The zero positions for each of these angles correspond to the center of the eccentric mass being along the *z*-axis in the body-fixed frame. In addition, $r_c^{\,m}$ is defined as:

$$r_c^{\,m} = \begin{bmatrix} 0 & 0 & L \end{bmatrix}^T \tag{15}$$

Once in the body-fixed frame, the location of the center of mass is rotated into the inertial frame by multiplying for the inverse rotation matrix $\left(R_e^{\,b}\right)^{-1}$.

With this vector in the inertial frame, it is then crossed with the weight vector W.

$$W = \begin{bmatrix} 0 & 0 & mg \end{bmatrix}^T \tag{16}$$

This vector defines the gravitational force acting at the center of mass (g is the acceleration due to gravity).

After this cross product, the result is a moment in the inertial frame. This is then rotated back into the body-fixed frame using the rotation matrix R_e^b. Once the hydrodynamics and gravitational effects are included, the dynamics can be reduced to the following:

$$M_T\dot{V} + C_T V - G_T = B_1\tau_1 \tag{17}$$

where $G_T = \begin{bmatrix} 0 & \left(T_c^b\right)^T \end{bmatrix}^T$.

Since T_c^b can be seen as a control input (the motors deflect the eccentric mass), it is lumped with the control input τ_1, which is made up of the gimbal motor torques and thruster forces. The equations of motion therefore become:

$$M_T\dot{V} + C_T V = B_1\tau_1 + G_T = B\tau \tag{18}$$

This final form is useful, as it is in a classical form. This allows for us to implement classical control on the system, even though the control input is a sum of the usual motor torques and gravitational forces. In this way, the control strategy can be seen a form of Partial Feedback Linearization (PFL). While not all dynamics are "cancelled out" and replaced by artificial dynamics, as is the case with conventional PFL, the effects of gravity are offset when they are lumped with the motor torques. The exact way in which these moments are lumped together is described in the subsequent section. Later, when the system is simulated, the effects of gravity are considered in order to model the motions of the gimbal within the ROV.

2.3.2. Actuator Singularity

The actuation scheme presented and modeled in this analysis contains one key problem. This problem arises from the fact that the thrusters are fixed to the hull of the ROV, and thus can only ever provide a moment about a single axis in the body-fixed frame. In the current configuration, this is the z-axis. However, the gravitational moments provided by internal gimbal mechanism can only provide moments about the x and y axes in the inertial frame. This means that when the z-axis in the body-fixed frame is parallel to the x-y plane in the inertial frame, the thrusters provide a redundant moment to the gravitational effects of the shifting of the internal gimbal.

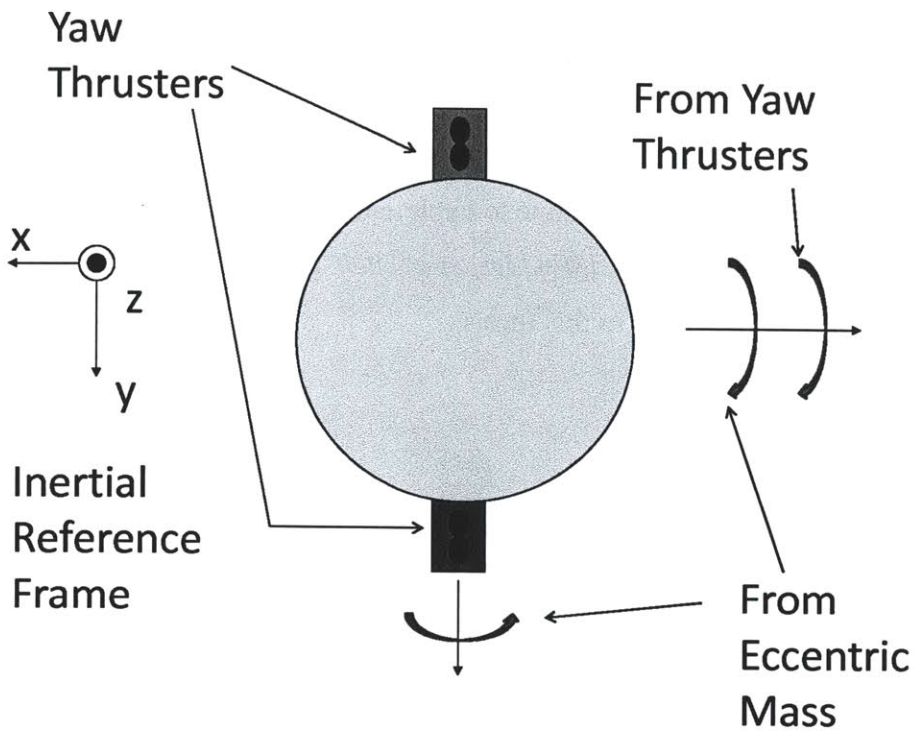

Figure 11 - Example orientation that constitutes actuator singularity.

This situation can be said to occur when the following relationship is true. This corresponds to the z-axis of the body-fixed frame being parallel to the x-y plane in the inertial frame.

$$\underline{e}_Z \bullet \left(R_e^{\ b}\right)^T \underline{e}_z = 0 \tag{19}$$

In this $\underline{e}_Z$ is the unit vector in the direction of the inertial z-axis, and $\underline{e}_z$ is the unit vector in the direction of the body-fixed z-axis.

This singular situation occurs when either of the third entries in the first and second rows in $R_e^{\ b}$ is unity. These entries are: $r_{13} = -s_\theta$ and $r_{23} = s_\phi c_\theta$ (r_{xx} is an entry in $R_e^{\ b}$). These are equal to 1 when:

$$\theta = \pm\frac{(2n+1)\pi}{2} \; or \; \phi = \pm\frac{(2n+1)\pi}{2} \text{ and } \theta = \pm 2\pi n \tag{20}$$

Therefore, these orientations correspond to situations of "actuator singularity".

Fortunately, these singularities are not detrimental. One reason is that in many of these configurations, the motor torques will still contribute to the yaw moment. This can be seen by examining $P_m{}^b$.

In addition, work has already been done to explore the effects of actuator redundancies on fault tolerance (*Sarkar, et al 2002* [32], *Podder, et al 2000* [33]). Much of this work can be applied readily to the design presented in this thesis.

2.4. Control

2.4.1. Formulation of the Control Input

The control input τ is made up of four quantities:

$$\tau = \begin{bmatrix} T & N_x & N_y & N_z \end{bmatrix}^T \tag{21}$$

These are defined as: the total forward thrust T, the roll moment N_x, the pitch moment N_y, and the yaw moment N_z. With these definitions, the input matrix B is defined as:

$$B = \begin{bmatrix} \begin{bmatrix} 1 & 0 & 0 \end{bmatrix}^T & 0_{3\times3} \\ 0_{3\times1} & I_{3\times3} \end{bmatrix} \tag{22}$$

In order to transform the control moments to physical control inputs (for implementation), we must consider actuator dynamics. The three physical control inputs for the three moments are the pitch gimbal motor torque T_x, the roll gimbal motor torque T_y, the thrust from the left thruster T_1, and the thrust from the right thruster T_2. In regard to the moment produced by the thrusters, we must also define the difference in thrust between the two thrusters, $\Delta T = T_1 - T_2$, (called the thrust difference for the remainder of this thesis).

From (18), it is known that the total control moment is a sum of the moments from the motor torques and thruster forces and the moment produced by deflections of the eccentric mass.

$$P_m{}^b \begin{bmatrix} T_x \\ T_y \\ \Delta T \end{bmatrix} + T_c{}^b = \begin{bmatrix} N_x \\ N_y \\ N_z \end{bmatrix} \tag{23}$$

In this equation, $P_m^{\ b}$ is a matrix used to transform the motor torques and thrust difference into the body-fixed frame. It is defined as:

$$P_m^{\ b} = \begin{bmatrix} 1 & 0 & 0 \\ 0 & c_\phi & 0 \\ 0 & -s_\phi & D/2 \end{bmatrix} \tag{24}$$

The first two columns of $P_m^{\ b}$ correspond to the transpose of the Jacobian, $\mathbf{J}$, defined as:

$$\begin{bmatrix} d\phi \\ d\theta \\ d\psi \end{bmatrix} = \mathbf{J} \begin{bmatrix} d\phi_c \\ d\theta_c \\ d\psi_c \end{bmatrix} \tag{25}$$

In addition, the third column of $P_m^{\ b}$ is the third column of the identity matrix (multiplied by the lever arm $D/2$), since the thrust difference moment is already in the body-fixed frame. This is because the thrusters are mounted to the body of the ROV.

To solve for the motor torques and thrust difference, the effects of the deflection of the mass must be subtracted from the desired moments (which can be seen as a form of feedback linearization). This simply involves restating equation (23):

$$\begin{bmatrix} T_x \\ T_y \\ \Delta T \end{bmatrix} = \left(P_m^{\ b}\right)^{-1} \left(\begin{bmatrix} N_x \\ N_y \\ N_z \end{bmatrix} - T_c^b \right) \tag{26}$$

In implementation, this computation will be made once the desired moments N_x, N_y, and N_z are found. Then, the computed torque will be commanded to the gimbal motors, and thrusts will be commanded to the left and right thrusters according to the following equation:

$$\begin{bmatrix} T_1 \\ T_2 \end{bmatrix} = \frac{1}{2} \begin{bmatrix} 1 & 1 \\ 1 & -1 \end{bmatrix} \begin{bmatrix} T \\ \Delta T \end{bmatrix} \tag{27}$$

As mentioned previously, the motor torques induce the deflections that cause the moment T_c^b. We modeled these dynamics as a simple second order system, described by the following equations of motion:

$$-\begin{bmatrix} T_x \\ T_y \end{bmatrix} - A_m R_m{}^b \frac{D}{2}\begin{bmatrix} 0 \\ 0 \\ \Delta T \end{bmatrix} = -A_m \left(R_m{}^b\right)^T T_w{}^b A_m{}^T + D_m \begin{bmatrix} \dot{\phi}_c \\ \dot{\theta}_c \end{bmatrix}$$
$$+s\left(\begin{bmatrix} \dot{\phi}_c \\ \dot{\theta}_c \end{bmatrix}\right)\left(A_m \left(\left(R_m{}^b\right)^T R_e{}^b J_{ball} \left(R_e{}^b\right)^T R_m{}^b\right) A_m{}^T \begin{bmatrix} \dot{\phi}_c \\ \dot{\theta}_c \end{bmatrix}\right) \tag{28}$$
$$\left(A_m \left(\left(R_m{}^b\right)^T R_e{}^b J_{ball} \left(R_e{}^b\right)^T R_m{}^b\right) A_m{}^T\right)\begin{bmatrix} \ddot{\phi}_c \\ \ddot{\theta}_c \end{bmatrix}$$

where $D_m = diag\left(\begin{bmatrix} D_{x,motor} & D_{y,motor} \end{bmatrix}\right)$ is a damping matrix, $J_{ball} = diag\left(\begin{bmatrix} J_{x,weight} & J_{y,weight} & J_{z,weight} \end{bmatrix}\right)$ is the inertia matrix of the inner mass in the inertial frame, $T_c^b = R_e^b \cdot \begin{bmatrix} 0 & 0 & m_{weight} g \end{bmatrix} \times \left(\left(R_e^b\right)^{-1} R_m{}^b r_c^m\right)$ is the gravitational torques acting on the internal mass (m_{weight}), and A_m is a matrix for eliminating the elements corresponding to yaw rotation.

$$A_m = \begin{bmatrix} 1 & 0 & 0 \\ 0 & 1 & 0 \end{bmatrix} \tag{29}$$

2.4.2. Reduction of the Dynamics

By examining the input matrix B in (22), it can be seen that there are no actuators in the y and z directions. However, the model dynamics suggest small translations caused by the deflections of the center of mass as well as from the presence of lift. However, in implementation on a physical system as well as in simulation, these translations were observed to be negligibly small. As such, the dynamics in the y (sway) and z (heave) directions are assumed to be zero. With this understanding, the ROV can be seen as a vehicle with non-holonomic constraints, similar to a wheeled car. A wheeled car is incapable of making motions orthogonal to its wheel direction, and this vehicle is incapable of swimming in any direction other than forward in the body-fixed frame (in the current configuration, this is the x-direction)

Under this assumption, the dynamics may be represented in the following manner:

$$M_{T,red}\dot{V}_{red} + C_{T,red}V_{red} = B_{red}\tau \tag{30}$$

where $V_{red} = [u \quad p \quad q \quad r]^T$ and all matrices in the dynamics are transformed in the following manner:

$$M_{T,red} = A_{red} M_T A_{red}^{\ T}, C_{T,red} = A_{red} C_T A_{red}^{\ T}, \text{ and } B_{T,red} = A_{red} B_T A_{red}^{\ T} \tag{31}$$

where

$$A_{red} = \begin{bmatrix} 1 & 0 & 0 & 0_{1\times 3} \\ & 0_{3\times 3} & & I_{3\times 3} \end{bmatrix} \tag{32}$$

These reduced dynamics will prove useful in the development of a control law for the full order system, since we can only provide control inputs along the directions of the reduced system.

2.4.3. Open Loop Stability

For the stability analysis we computed the poles of the open loop system, linearized at various points, to examine the need for feedback control. To compute the poles of the system, the dynamics are linearized in the following manner:

$$A = \frac{\partial}{\partial V}\left(-M_T^{-1} C_T V\right)\Big|_{V=\bar{V}} \tag{33}$$

In order to examine the open loop stability of the system when the ROV is translating forward, this linearization was first taken about the following points:

$$\bar{V} = [\bar{u} \quad 0_{1\times 5}]^T \tag{34}$$

$\bar{u}$ (the forward velocity) is varied, producing different state matrices (since the linearization point is different). This corresponds to the robot moving forward at increasing speeds. The eigenvalues of these state matrices are plotted with respect to $\bar{u}$ (instead of the traditionally used control gain) in the upper left plot of Figure 12. For the physical parameters used in this stability analysis, refer to Table 6.

Instability also exists with rotational motions. As such, a linearization was taken about:

$$\bar{V} = [0.02m/s \quad 0_{1\times 2} \quad \underline{p} \quad 0_{1\times 2}]^T \tag{35}$$

In this, $\bar{p}$ was varied, and again the corresponding poles for the changing state matrices were plotted in the upper right plot of Figure 12. A non-zero forward velocity is needed in order to examine the full effects of rotational velocities. This was done for the two other rotational velocities as well. These linearization points are as follows.

$$\bar{V} = \begin{bmatrix} 0.02m/s & 0_{1\times 3} & \underline{q} & 0 \end{bmatrix}^T \tag{36}$$

This corresponds to rotations about the pitch axis (the y-axis).

$$\bar{V} = \begin{bmatrix} 0.02m/s & 0_{1\times 4} & \underline{r} \end{bmatrix}^T \tag{37}$$

This corresponds to rotations about the yaw axis (the z-axis).

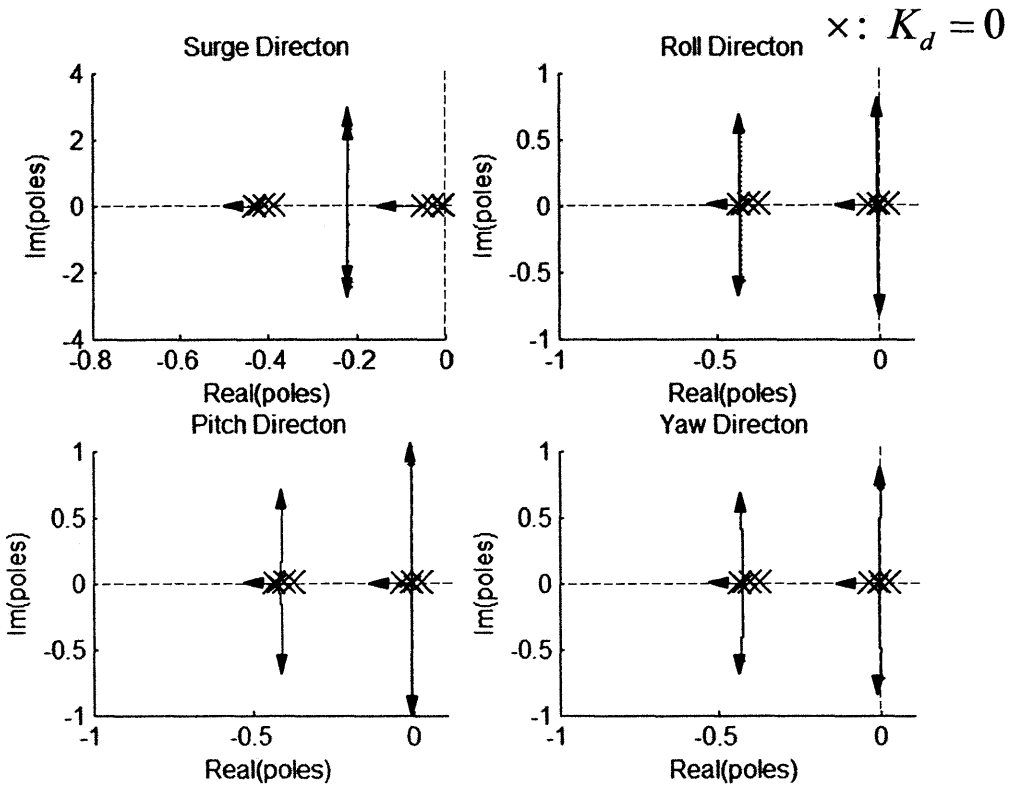

Figure 12 - Open loop poles of the reduced system with respect to forward velocity as well as to rotational velocity, with a constant forward velocity (20 cm/s). The forward velocity spans from 0 cm/s to 2 cm/s and all angular velocities span from 0 rad/s to $\pi/4$ rad/s.

Four poles are complex in all cases. As such, there will be an oscillatory motion which would prove problematic in camera positioning. To solve this problem, stability augmentation is

implemented through the use of an internal feedback loop to place these poles in the left half plane as close to the real axis as possible.

2.4.4. Stability Augmentation

The general control architecture for stability augmentation will take on a nested structure.

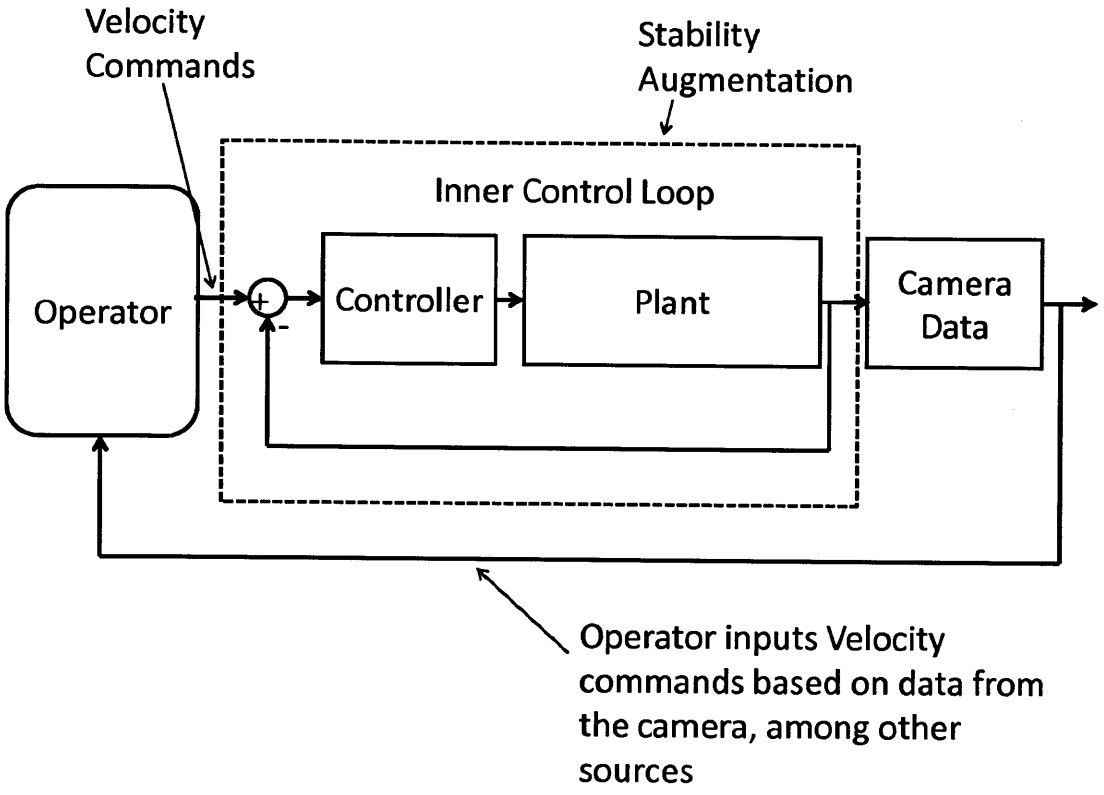

Figure 13 - Diagram of the general control system design.

Internally, the ROV will stabilize the system using input from the operator as a reference. The operator, in the external control loop, will input velocity references to the inner control loop based on video feedback.

In order to command the correct velocities to the inner control loop, we must understand the nature in which the operator will interact with the ROV. One action for the operator is to pan or tilt with the camera. This is done by rotating the vehicle in 2 directions. Another action is to move the vehicle forward and backwards.

Therefore, the commands from the operator are three in total. They consist of a linear velocity command, as well as two angular velocity commands (corresponding to the pan and tilt motions of the camera's view). These velocities are defined as $v_{forward}$, ω_{pan}, and ω_{tilt} respectively. They are transformed into body-fixed velocity references in the following manner (ignoring the sway and heave directions):

$$\begin{aligned} V_{ref} &= \begin{bmatrix} v_{forward} & -\frac{\sqrt{2}}{2}\omega_{tilt} & \omega_{pan} & \frac{\sqrt{2}}{2}\omega_{tilt} \end{bmatrix}^T \\ &= \begin{bmatrix} u_{ref} & p_{ref} & q_{ref} & r_{ref} \end{bmatrix}^T \end{aligned} \tag{38}$$

where u_{ref} is the x velocity reference and p_{ref}, q_{ref} and r_{ref} are the roll, pitch, and yaw velocity references. This is done assuming the camera is oriented 45° from vertical (as in Figure 4). This orientation is used so that when the ROV is navigating a pipe, it can simultaneously look forward, to navigate, and look downward, to inspect passing features.

2.4.5. Proportional Control

Once these input velocities are determined, we must implement a control system in order to coerce the ROV to follow the commands of the operator. The simplest way to implement stability augmentation is basic proportional control. This is especially simple due to the fact that only a few cost-effective sensors are needed for feedback (i.e., gyros, accelerometers).

Since the sway and heave directions are not actuated, we will examine the reduced system in (30) in order to formulate a control input (since the input matrix is invertible for the reduced dynamics). For proportional control on the reduced system, the following control input must be generated:

$$\tau = B_{red}^{-1}\gamma \tag{39}$$

where γ is the desired input into the system, defined as:

$$\gamma = \begin{bmatrix} -K_{u,P}(u-u_{ref}) \\ -K_{p,P}(p-p_{ref}) \\ -K_{q,P}(q-q_{ref}) \\ -K_{r,P}(r-r_{ref}) \end{bmatrix} = \begin{bmatrix} -K_{u,P}\tilde{u} \\ -K_{p,P}\tilde{p} \\ -K_{q,P}\tilde{q} \\ -K_{r,P}\tilde{r} \end{bmatrix} \tag{40}$$

In this, K_u, K_p, K_q and K_r are proportional gains and $\tilde{u}$, $\tilde{p}$, $\tilde{q}$, and $\tilde{r}$ are the error signals. When this is inputted into the full order system, the dynamics of the full order system become:

$$\begin{aligned} &M_T\dot{V} + C_T V = B\left(B_{red}\right)^{-1}\gamma \\ &= \begin{bmatrix} -K_{u,P}\tilde{u} & 0 & 0 & -K_{p,P}\tilde{p} & -K_{q,P}\tilde{q} & -K_{r,P}\tilde{r} \end{bmatrix}^T \end{aligned} \tag{41}$$

The following gains were used for simulation and experiments:

$$\begin{aligned} K &= \begin{bmatrix} K_{u,P} & K_{p,P} & K_{q,P} & K_{r,P} \end{bmatrix}^T \\ &= \begin{bmatrix} 3 & 0.0625 & 0.0625 & 0.0625 \end{bmatrix}^T \end{aligned} \tag{42}$$

To determine if the poles of the closed loop system are stable, the eigenvalues of the following state matrix are found:

$$A = \frac{\partial}{\partial V}\left(M_T^{-1}\left(-C_T V + B\left(B_{red}\right)^{-1}\gamma\right)\right)\Big|_{V=\bar{V}} \tag{43}$$

A table of several additional linearization points follows, showing the stability granted by using proportional control. For the physical parameters used in this stability analysis, refer to Table 6.

Table 2 – Linearization points and resulting eigenvalues after proportional control is applied

$\bar{V}$	Physical Meaning	Eigenvalues
$\bar{V} = [0.02 \text{ m/s} \quad 0_{1\times5}]^T$	Forward Velocity	$[-79.3 \quad -3.01 \quad -0.430 \quad -0.430 \quad -91.0 \quad -92.4]$
$\bar{V} = [0.02 \text{ m/s} \quad 0.1 \text{ rad/s} \quad 0_{1\times4}]^T$	Roll Velocity coupled with Forward Velocity	$[-79.3 \quad -3.01 \quad -0.430 \pm 0.0745i \quad -91.0 \quad -92.4]$
$\bar{V} = [0.02 \text{ m/s} \quad 0 \quad 0.1 \text{ rad/s} \quad 0_{1\times3}]^T$	Pitch Velocity coupled with Forward Velocity	$[-79.3 \quad -3.01 \quad -0.432 \quad -0.430 \quad -91.0 \quad -92.4]$
$\bar{V} = [0.02 \text{ m/s} \quad 0_{1\times2} \quad 0.1 \text{ rad/s} \quad 0_{1\times2}]^T$	Yaw Velocity coupled with Forward Velocity	$[-79.3 \quad -3.01 \quad -0.432 \quad -0.430 \quad -91.0 \quad -92.4]$

As shown with these example linearization points, proportional control stabilizes the full order system by placing all poles in the left half of the complex plane. In addition, the oscillatory nature seen in the open loop system has been stabilized, with only one pair of left-half plane, low frequency poles (seen in Table 2). This stability is assumed to persist for a region about the linearization point. Determination of the exact region is a possible topic for future study.

The fact that the full order system can be stabilized lends credibility to the assumption that the heave and sway velocities are essentially zero. Even though these directions are not actuated, they are stable.

2.5. Simulations

In order to simulate the ROV, the proportional velocity control system was implemented in simulation for the full order system. Step responses were simulated for a constant forward velocity and a constant pitch velocity. All parameter values can be found in Table I. In these simulations, the gains were those seen in (42). In addition, the physical parameters were those found in Table 6.

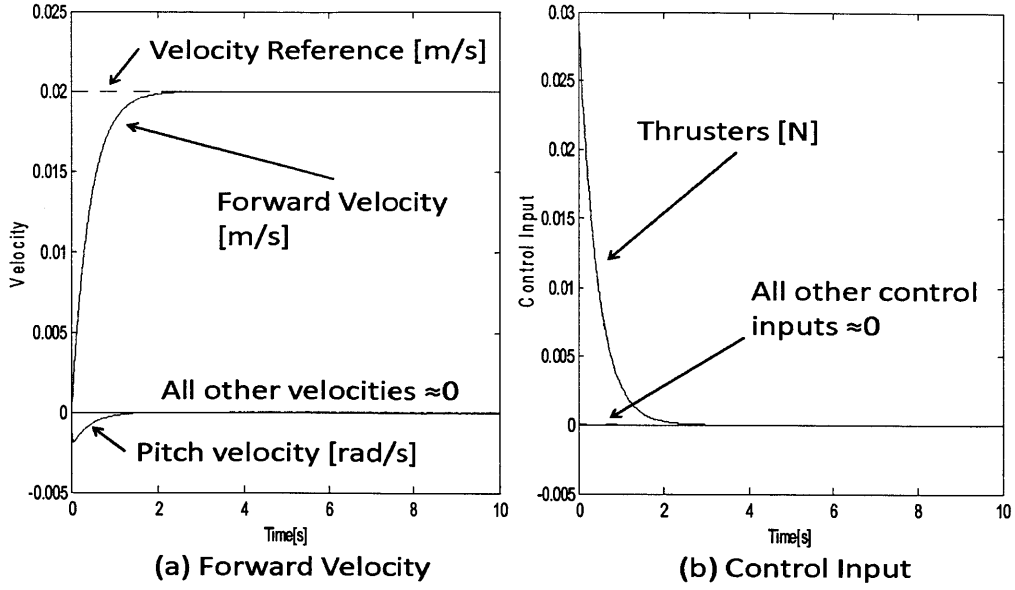

Figure 14 – Step response for commanded forward velocity.

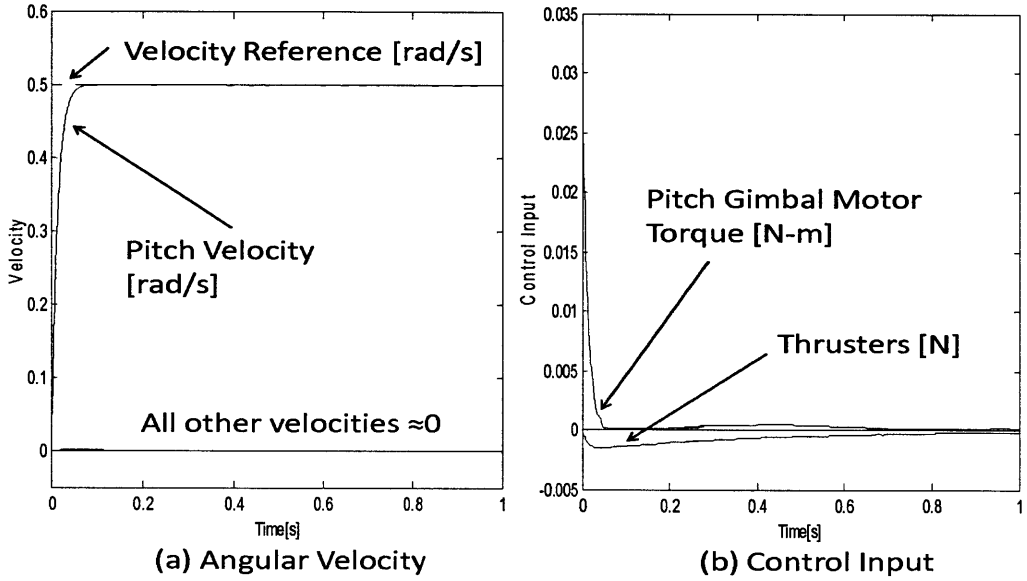

Figure 15 – Step response for commanded angular velocity about the y-axis (pitch).

One important verification to make is that the heave and sway velocities of the ROV are negligibly small. Below are two plots for these two values, taken in the case of both simulations seen previously, the first of which being a step command for the forward velocity and the second of which being a step command for a pitch velocity.

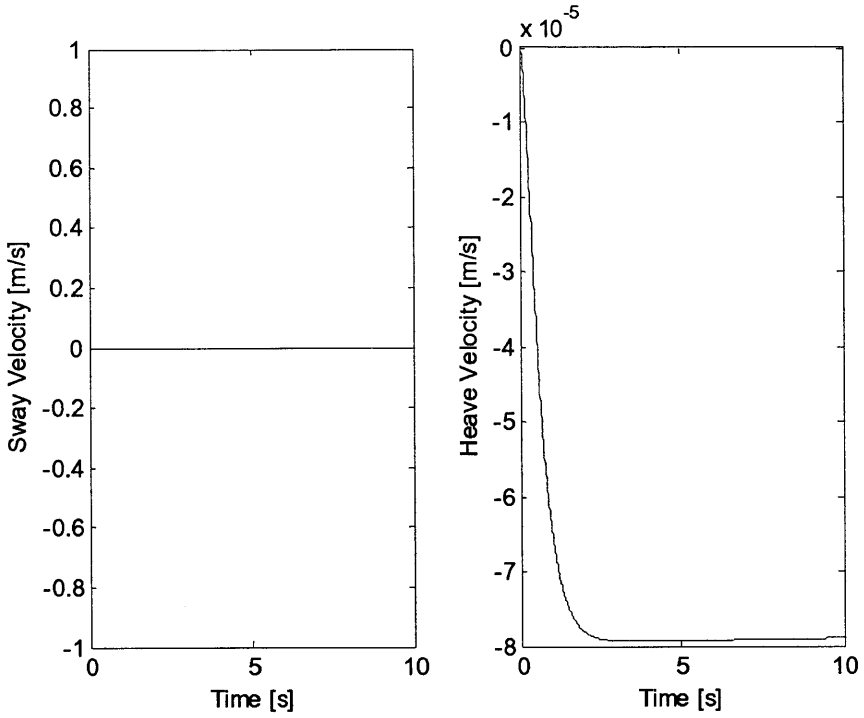

Figure 16 - Transverse velocities of the ROV when commanded to a constant forward velocity. The step response of the system under these simulation parameters can be seen in Figure 14.

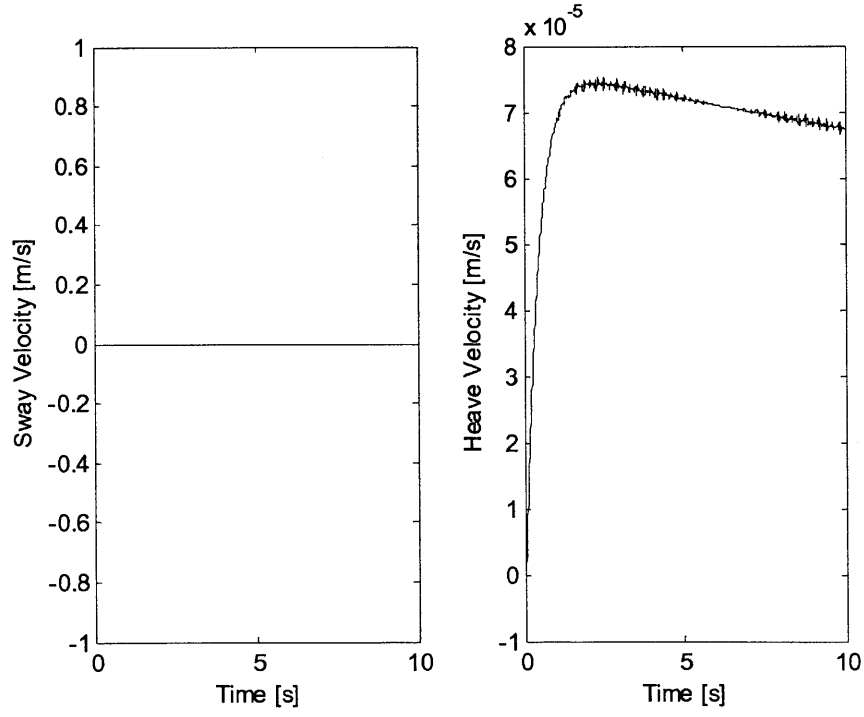

Figure 17 - Transverse velocities of the ROV when commanded to a constant pitch velocity. The step response of the system under these simulation parameters can be seen in Figure 15.

As can be seen, the induced velocities in the sway and heave directions are approximately four orders of magnitude smaller than the velocity commands put into the control system ($\sim 10^{-1} m/s$ vs. $\sim 10^{-5} m/s$). As such, the assumption of having each of these velocities as zero in our model is a valid one.

2.6. Experiments

A simple proof-of-concept prototype was built to test this design (see Figure 8). It consists of a tethered spherical robot with two outboard thrusters for translational control. It is equipped with a LPR530AL rate gyro for pitch and yaw rate measurements, and a LY530ALH rate gyro for roll rate measurements.

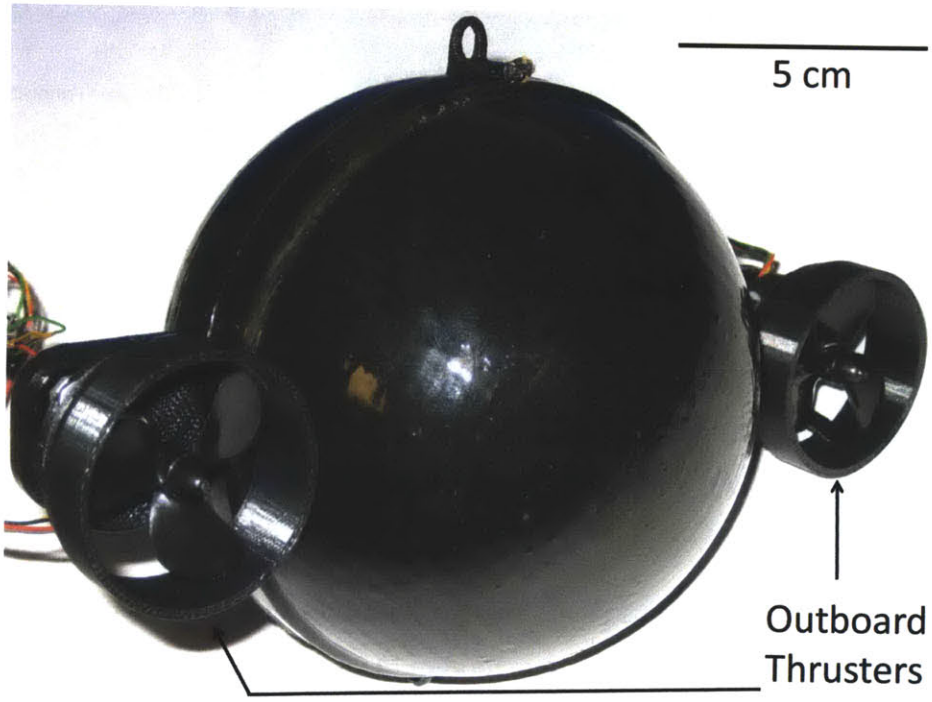

Figure 18 - Photo of the prototype used to test the model and control system. Note that for simplicity two outboard thrusters were used.

The orientation control is actuated, as described previously, using an internal 2-axis gimbal. A general outline of its assembly is shown below.

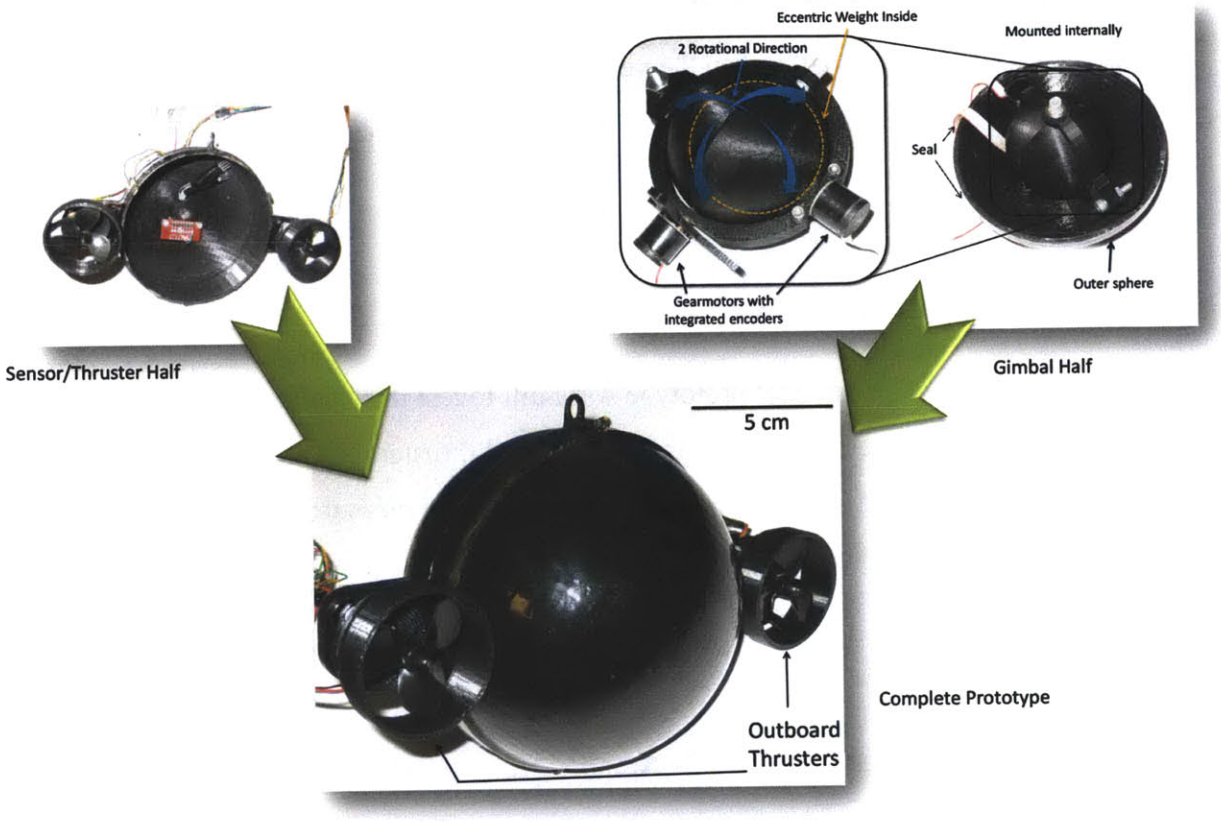

Figure 19 - Diagram of the assembly of the prototype. There are two halves, one with with propeller thrusters and gyroscopic angular rate sensors, and the other with the two-axis gimbal system. They are joined with a water-tight seal.

A camera was not included in testing in order to avoid complexity. In addition, the true focus of this work is not on the camera itself, but on the orientation control of the ROV and the camera, which has been explored in depth.

As an initial test, the eccentric mass was positioned to a certain pitch angle using PID control on the pitch gimbal motor. The orientation of the ROV was measured through integration of a rate gyro signal, and compared to the pitch angle. The motion of this is similar to the motion described in Figure 6. In this, we move the center of mass of the vehicle to a certain angle, and watch as the ROV follows, going to the exact same position. This shows how the stable point of the system can be changed. Note that the physical parameters of this system can be found in Table 6.

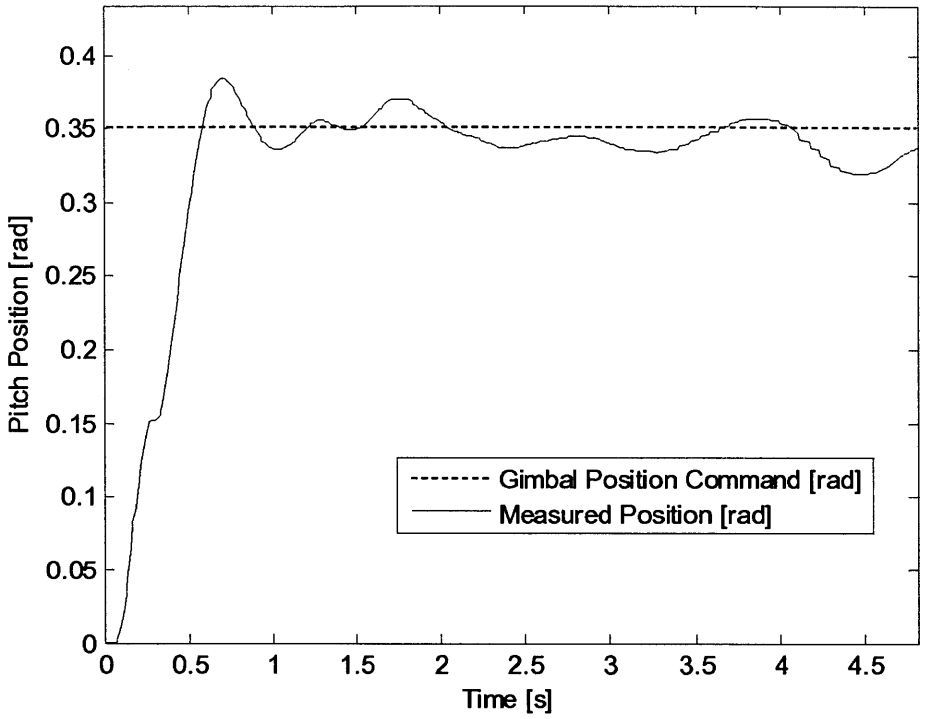

Figure 20 -Response of Vehicle to step input of the pitch gimbal motor.

This demonstrates the ability of the ROV for orientation change in what is essentially open loop control. As can be seen, the point to which the gimbal motor moves becomes a new stable point for the system.

Velocity control about the pitch axis was also carried out as a proof of concept (using the gains in (42)).

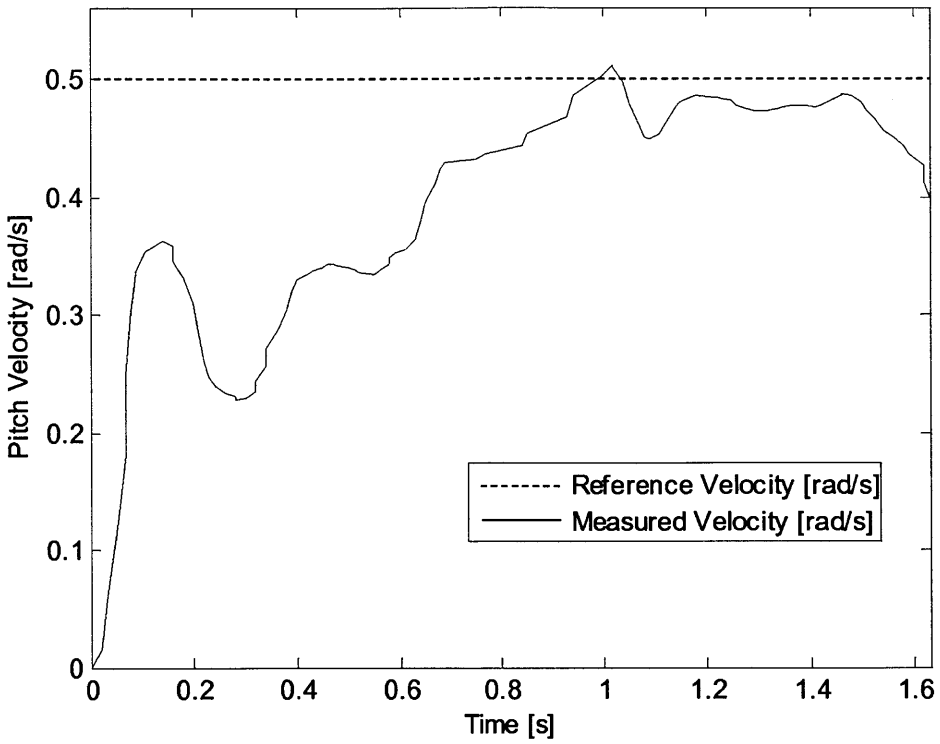

Figure 21 – Experimental and simulated step responses for a pitch velocity. There are some oscillatory disturbance effects from the presence of a tether.

This shows the feasibility of velocity control on the physical system. Future prototypes with internal thrusters are predicted to behave similarly, and the eventual addition of wireless communication will remove disturbances from the tether.

2.7. The Eyeball ROV: A Summary

This section of this thesis presents and demonstrates a novel design for a spherical ROV for the purpose of moving a camera fixed to the body of the vehicle. This is useful for underwater inspection tasks in which a small, agile robot is needed. The advantages of this design have been established in detail previously, as have the system dynamics and stability analysis. Among these advantages are the ability to rotate in place, passive collision avoidance due to a spherical outer shape, the ability to change the stable orientation of the vehicle (granting passive stability), and a readily scalable design.

A proportional controller is successful in implementing stability augmentation on the system, even though the system is underactuated. However, although the ROV is not actuated in two linear directions, these directions are shown in simulation to have induced velocities of remarkably small magnitude ($\sim 10^{-5} m/s$). This allows for a simple control architecture for controlling this complex mechanical system. This simplicity eases implementation, and is shown to be successful on a proof-of-concept prototype.

With stability established, this ROV design facilitates inspection of underwater structures by allowing for an operator to "look" in any direction with the vehicle with little translational motion and with an exceedingly simple external geometry (a sphere). In addition, this design could be used for stable orientation control of devices beyond a camera, including line-of-sight communication systems (which will be discussed in the subsequent sections). In addition, this actuation scheme can truly be applied to any underwater vehicle, and as such is a general design for continuous rotation orientation control.

Chapter 3

Visible Light Based Communication and Localization: A Dual-Use System

3.1. Underwater Wireless Communication

Due to the fact that a tether could potentially damage fragile sensors in the piping systems of the primary cooling system, a wireless communication system must be used. However, underwater communication systems remain a largely unresolved field. Unlike in-air communications, in which radio frequency systems have become an industry standard, underwater communications rely on a number specialized technologies, each with clear disadvantages. The most prevalent of these technologies is acoustic systems, which use modulated pressure waves in order to transmit data over long distances (~1 km) but at relatively low communication speeds (~10 kbps) [34]. Radio frequencies are also used in underwater applications, and while capable of very high data rates (>100 kbps), are severely limited in communication ranges underwater (<20 m).

For the application discussed in this thesis, that of inspection of the underwater structure of a nuclear reactor, both high data rates and long range are a requirement. High data rates are required to relay video, and long ranges in water are required to communicate in the more than 20m lengths of pipe in the piping systems of a typical reactor. As such, an underwater

communication system that provides long range communications at high data rates is required. To meet this requirement, visible light communication systems were explored.

Visible light communication systems have been explored by many due to the fact that the visible bands of light (430~540 nm) possess low absorption coefficients in water, suggesting an ability for extended communication ranges [35]. This can be seen in the proceeding figure, which shows the absorption coefficient of varying frequencies of electromagnetic radiation through water.

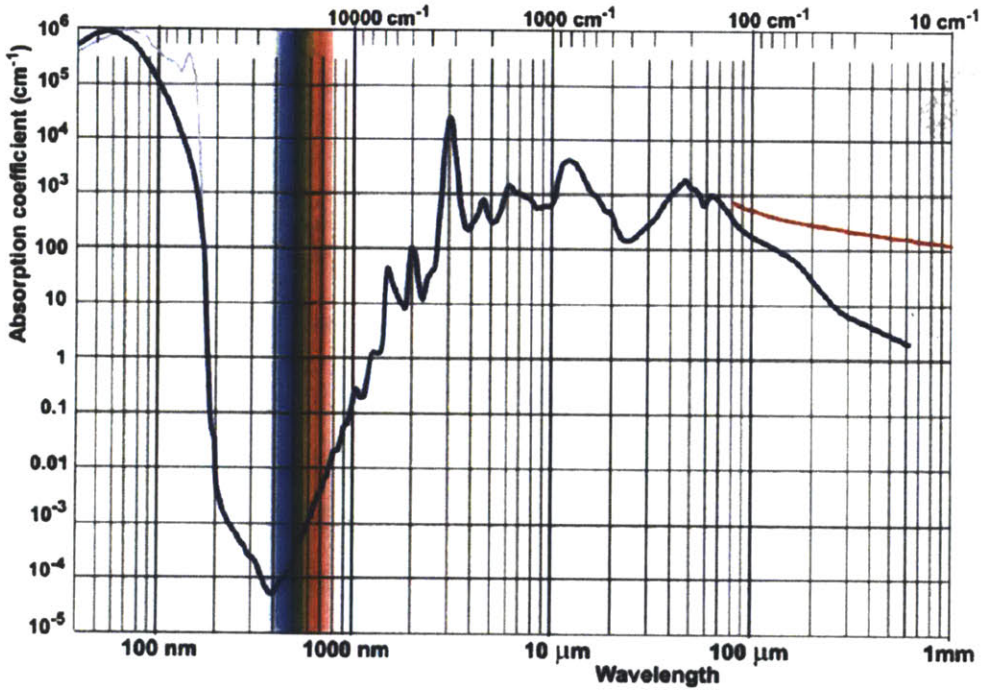

Figure 22 – Absorption coefficient of electromagnetic radiation in water versus wavelength. Note that there is a low point in this plot at the spectrum of visible light (~470nm) [36].

As can be seen in this figure, the wavelength of electromagnetic radiation that exhibits the lowest attenuation coefficient in water is ~470nm, which is blue visible light. What this means is that of all wavelengths of electromagnetic radiation, including conventional radio frequencies, blue light is the best wavelength to use for communication systems in water, since this suggests the possibility for the best possible range. In addition, since the "carrier frequency" of light is in the range of terahertz (10^{12}), bandwidth can be exceptionally high. In previous work

done by others, existing systems been shown to have data rates on the order of ~10 Mbps at ranges of ~40m [17].

3.2. Maintaining Line of Sight

A great deal of research has been done into optimizing both the range and data rates in these optical communication systems and reducing and quantifying the effects of interferences and disturbances [17], [18], [19], [37], [38] [39]. However, one major limitation of visible light communication systems is the necessity for line-of-sight contact between transmitter and receiver. In other words, both the transmitter and receiver must be "aimed" in order to establish a data link between an underwater robot and a distant operator. In order to accomplish this, the location of the transmitter must be known to the receiver system, and the location of the receiver must be known to the transmitter system. Some simplistic methods have been studied. Specifically, these methods include a photodiode array (similar to the work presented in this thesis), that simply utilizes the photodiode with the highest signal strength [17].

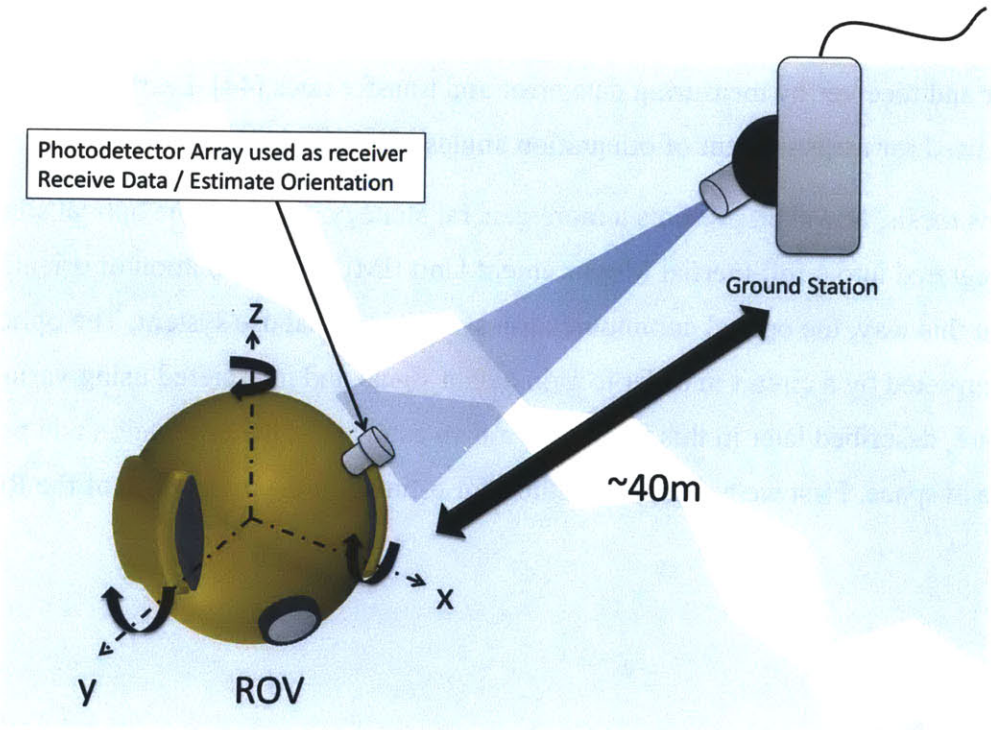

Figure 23 - Diagram of strategy used for the dual-use communication and orientation estimation system presented in this thesis. Note that the photodetector array mounted to the arbitrarily rotating ROV is used to both receive a signal from and locate the transmitter.

For this reason, knowledge of the orientation and position of the underwater ROV in this thesis must be known. This knowledge of the orientation and position of the ROV would allow the ROV to "point" its receiver, a photodetector of some sort, towards the transmitting light source. In addition, for bi-directional communication, the ROV must aim a light source of its own towards a receiver located at the distal ground station (see Figure 23).

This thesis proposes a method for estimating this orientation and position using the light source at the transmitter as a reference. In this way, the communication system takes on a dual purpose. In one respect it is a communication system. In the other it is used as a component in a system, detailed subsequently, for estimating the orientation and location of an ROV (localization).

This technique of using a communication system for localization has been applied to radio and sonar systems with significantly different hardware and algorithms [40]. Optical sources have been used as references for localizing robots for the purpose of docking [41]. In addition, optical localization techniques have been developed using a predetermined transmitted light pattern and various machine vision algorithms, include image "mosaic" approaches [42], [43]. A visible light communication system has been used to estimate distance between transmitter and receiver by measuring data error and transfer rates [44]. Lastly, laser rangefinders have been used for measurement of orientation angles of a body [45].

This thesis, however, presents a more general strategy, in which the optical source of light is integrated into a full Inertial Measurement Unit (IMU) for estimation of orientation and position. In this way, the optical communication system is a dual use system. The optical signal is both interpreted by a circuit in order to gain a data signal and interpreted using various sensors and software, described later in this thesis, to gain an estimate of the orientation and position of the vehicle in space. First we examine a method for estimating the orientation of the ROV.

3.3. Orientation Estimation

3.3.1. Traditional Orientation Angle Estimation

Traditional methods of orientation estimation typically consist of processing a variety of sensor signals using a Kalman Filter in order to determine 3-axis orientation estimation. This system is typically packaged in a piece of hardware known as an IMU (inertial measurement unit). The sensors used typically include a three-axis rate gyro, which can be integrated in order to determine the three orientation angles. Unfortunately, as with integration of any signal, drift can occur in the integration due to small DC errors in the rate signal. This is demonstrated in Figure 2, in which a rate gyro was affixed to a platform, the orientation of which was measured directly using an optical encoder (see Figure 29 for the system with which this data was taken).

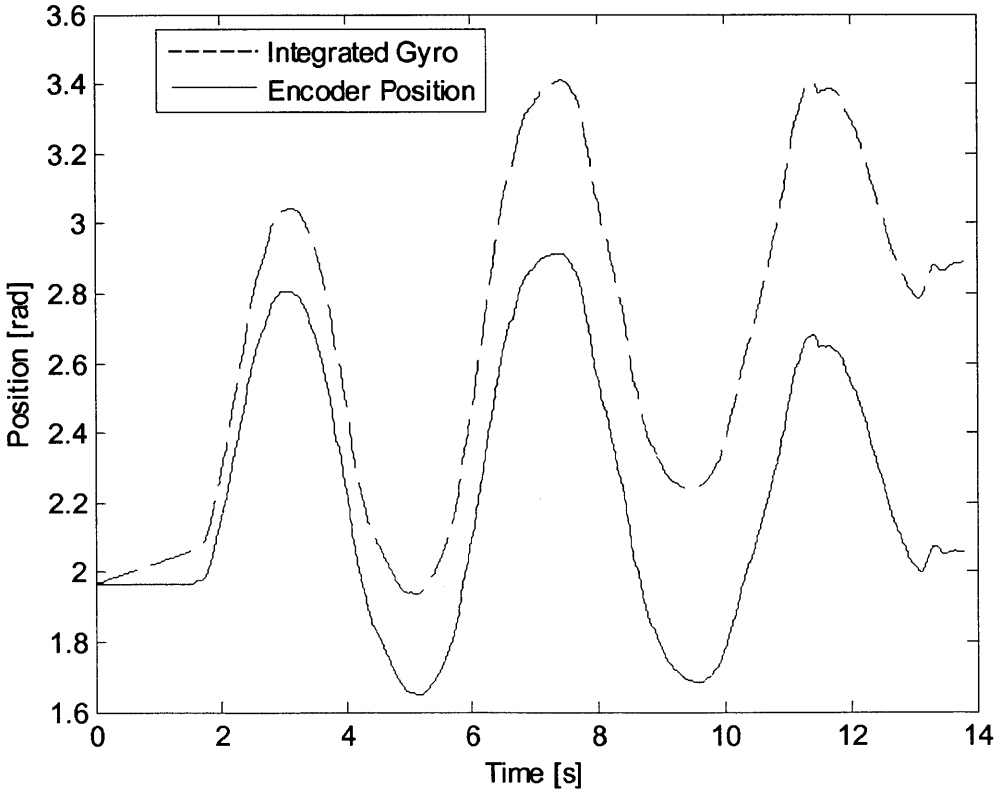

Figure 24 - Demonstration of rate gyro integration drift.

Usually, this integration drift is removed by updating the output of this integration, via Kalman filter, with a driftless, albeit noisy sensor. Traditional sensors include accelerometers, which measure driftlessly the direction of gravity, and magnetometers, which measure the direction of magnetic north.

For many applications, this strategy can be effective; however there are many cases in which magnetometers can be overly noisy or even completely ineffective. Most notably, these include industrial environments in which there is magnetic interference. The application pertinent to this thesis, that of the navigation and inspection of nuclear reactor and the associated piping systems, is one of these industrial applications. The entire workspace is encased in steel, and sometimes a layer of concrete. As such, a magnetometer is useless in this environment, since the Earth's magnetic fields penetrate the walls of this environment poorly.

Because of these potential failings, this thesis proposes that this driftless sensor in the orientation estimation procedure can be replaced by a sensor that measures orientation using a distant light source as a reference.

3.3.2. The Photodiode Array

The magnetometer, in IMU systems, is traditionally used to remove integration drift in the yaw direction (about the z-axis). We propose replacing this magnetometer with a circular photodiode array, which uses the relative signal strengths on each sensor to determine where approximately the transmitter light source is relative to the ROV, in the yaw direction (see Figure 25). The photodiodes in this array can also be used to receive data from the transmitting light source.

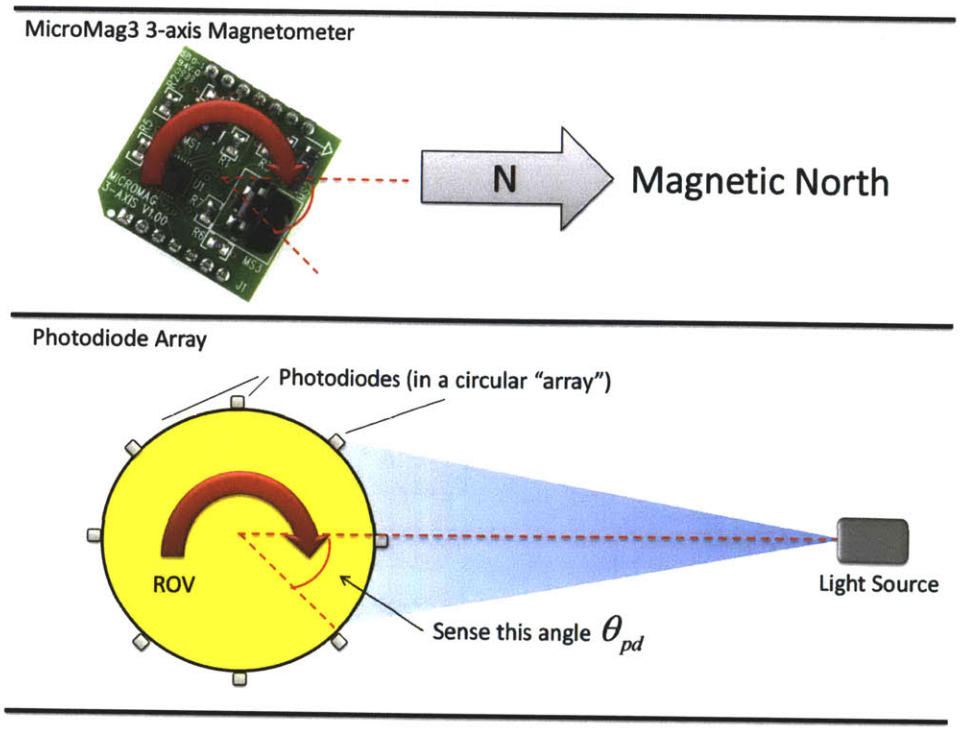

Figure 25 – Strategy for replacement of magnetometer with a photodiode array.

The yaw orientation of the ROV relative to the location of the light source is determined using a simple algorithm. For the purpose of this explanation, we will consider rotations only in the yaw direction, since additional rotations would require a photodiode array with greater complexity than the circular shape presented.

The three photodiodes in the circular array with the highest signal intensity are considered exclusively. This signal is derived by placing the photodiode as the input to a transimpedance amplifier, which converts the current generated by the photodiodes into a usable voltage signal (see Figure 32). This voltage signal is proportional to the intensity of the light striking the particular photodiode. In addition, this voltage signal would carry, along with a DC value proportional to the intensity of the light at that photodiode, a high frequency component that is to carry a data signal. This DC signal is extracted using a low pass filter.

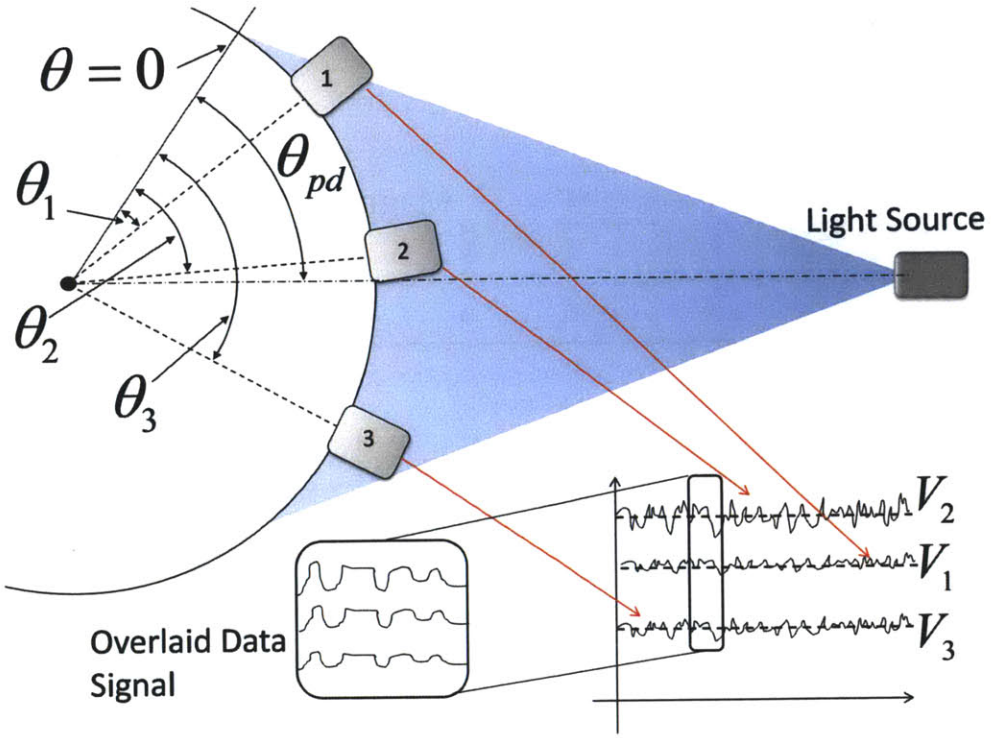

Figure 26 – Relative signal strengths of photodiodes in the circular array. Note that each signal contains the overlaid data signal.

Since each photodiode is fixed to the ROV, each can be assigned a particular angle (see Figure 26). Namely, this is the yaw angle of the ROV when each particular photodiode is pointed directly at the light source. With these orientation angles assigned, an approximation of the yaw orientation of the ROV can be made by taking a weighted average of these assigned orientation angles for the three photodiodes with the highest signal intensity. The weight for this weighted average is the DC signal intensity seen at the output of the transimpedance amplifier for each photodiode.

$$\theta_{pd} = \frac{\theta_1 V_1 + \theta_2 V_2 + \theta_3 V_3}{V_1 + V_2 + V_3} \tag{44}$$

The assumption is made in this thesis that the ROV does not move lateral to the receiver. This more complex case will be studied later in this thesis. For an example of this computation performed on data from the circular array seen in Figure 29 refer to Figure 27.

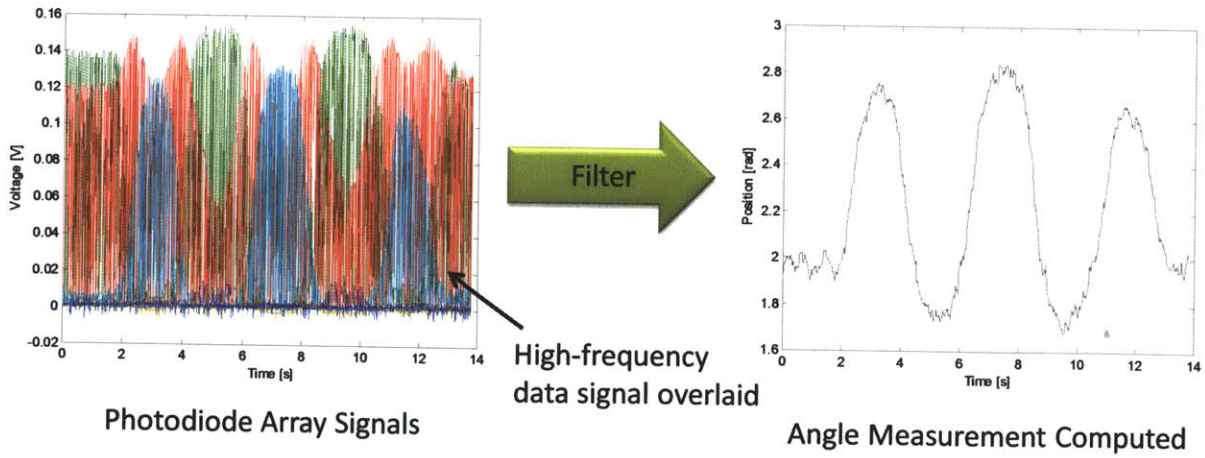

Figure 27 – Example computation of angle measured with the photodiode array.

This angle measurement will be used as a driftless measurement update in a discrete Kalman Filter used to measure the yaw orientation angle. This implementation of the Kalman Filter is detailed subsequently.

3.3.3. Kalman Filter Implementation

3.3.3.1. Kinematic Model

In order to implement the Kalman Filter, a model must be developed. This was done using a kinematic model, rather than a dynamic model of the system. As already stated, this thesis demonstrates the use of the optical communication system as an orientation reference with a simplified implementation, in which the yaw rotation angle alone is estimated. This eases implementation, as the dynamic model is linear in the case of a single rotation angle.

In order to determine this model, we must examine the nature of the integration drift in the signal. This integration drift is modeled as a constant bias to the angular rate signal, b. This corresponds to a linear error in the integrated position signal (see Figure 28)

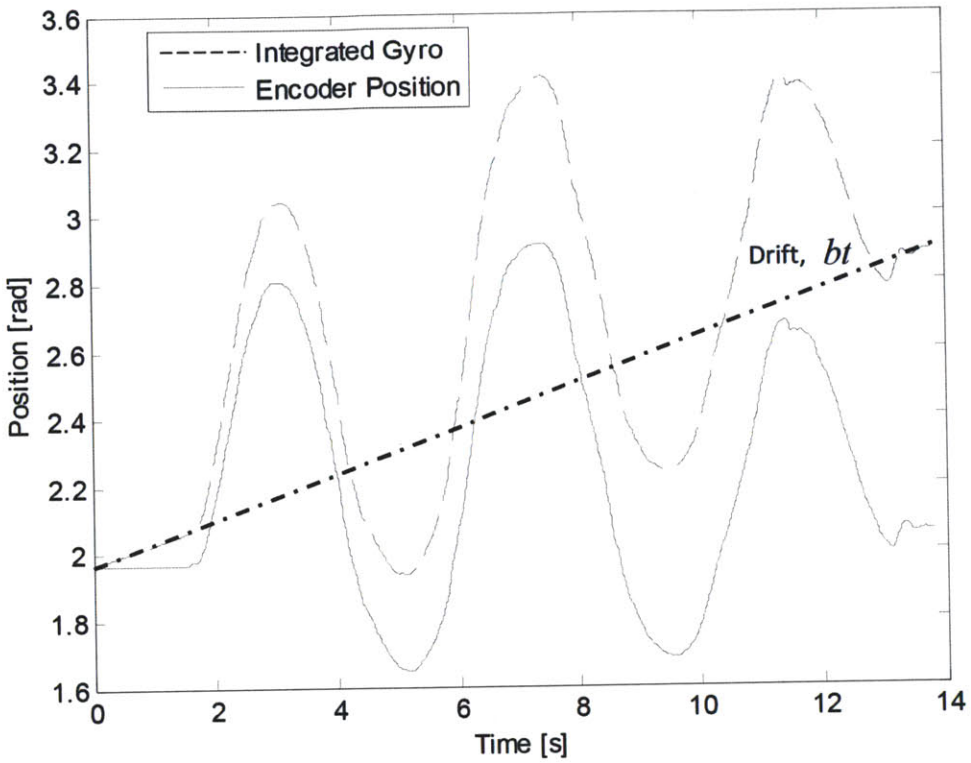

Figure 28 – Constant rate bias offset, seen after integration to achieve a position signal.

Operating under this assumption, we can state the signal outputted by the rate gyro as a sum of this constant bias and the actual angular velocity. In the example data in Figure 28, $b > 0$.

$$\dot{\theta}_{gyro} = \dot{\theta}_{act} + b \tag{45}$$

If we are to estimate the actual orientation angle ($\hat{\theta}$), $\dot{\theta}_{act}$ must be integrated via discrete-time integration:

$$\hat{\theta}_k = \hat{\theta}_{k+1} + \hat{\dot{\theta}}\Delta t = \hat{\theta}_{k+1} + \left(\dot{\theta}_{gyro} - \hat{b}\right)\Delta t \tag{46}$$

In this integration, k is a time index, $\hat{b}$ is an estimation of b, $\hat{\dot{\theta}}$ is an estimation of $\dot{\theta}_{act}$, and Δt is the time interval of each time step. In all data examined in this particular study, $\Delta t = 0.01s$.

This equation can be arranged into the classic state matrix form, if one includes b as a state. The state vector for this system is as follows:

$$x = \begin{bmatrix} \dot{\theta} & \theta & b \end{bmatrix}^T \tag{47}$$

Using this state matrix, the following discrete state equation can be found by rearranging (46):

$$x_k = \begin{bmatrix} 0 & 0 & -1 \\ \Delta t & 1 & 0 \\ 0 & 0 & 1 \end{bmatrix} x_{k-1} + \begin{bmatrix} 1 \\ 0 \\ 0 \end{bmatrix} \dot{\theta}_{gyro} + w(t) = Ax_{k-1} + Bu + w(t) \tag{48}$$

In this, $w(t)$ is the process noise. Note that in this implementation, the signal from the gyro is treated as the input to the system.

$$u = \dot{\theta}_{gyro} \tag{49}$$

In addition, for implementation of the Kalman filter, an output equation must be determined. Since the signal to be outputted by this orientation estimation algorithm is the orientation angle, the output equation must output this angle. Incidentally, the angle measured by the photodiode array mentioned previously should be approximately this angle as well. This allows for the update step of the Kalman filter, detailed subsequently, to be done using this same output equation.

$$\theta = \begin{bmatrix} 0 & 1 & 0 \end{bmatrix} \hat{x} + v(t) = H\hat{x} + v(t) \tag{50}$$

In this $v(t)$ is the measurement noise, corresponding to the noise inherent to the photodiode array.

3.3.3.2. Discrete Kalman Filter

With the dynamic model established, the discrete Kalman Filter can be implemented. It is done so in the classical manner, using the following recursive procedure [46]. The state estimate and error covariance matrix are initialized to the following values:

$$\hat{x}_0 = \begin{bmatrix} 0 & \theta_{pd_0} & 0 \end{bmatrix}^T, P_0 = I_{3\times 3} \tag{51}$$

The state is predicted using the model, as is the error covariance, according to the following equations:

$$\hat{x}_{k|k-1} = A\hat{x}_{k-1} + Bu_{k-1} \tag{52}$$

$$P_{k|k-1} = AP_kA^T + Q \tag{53}$$

The subscripts in $P_{k|k-1}$ and $x_{k|k-1}$ indicate that these are predictions for time step k based on time step $k-1$. Q is the covariance matrix for the process noise.

Once these predictions are made, they are updated using the following equations:

$$\hat{x}_k = \hat{x}_{k|k-1} + K_t\left(y_k - H\hat{x}_{k|k-1}\right) \tag{54}$$

$$P_k = \left(I_{3\times3} - K_kH\right)P_{k|k-1} \tag{55}$$

where K_k is the optimal Kalman gain, described by the following equation:

$$K_k = P_{k|k-1}H^T\left(HP_{k|k-1}H^T + R\right) \tag{56}$$

In (54), the measurement update corresponds to the measurement from the photodiode array.

$$y_k = \theta_{pd} \tag{57}$$

In addition, H is the output matrix, detailed in (50). R is the covariance matrix for the measurement noise.

3.3.4. Experimental Setup

In order to test this orientation estimation technique, a system was designed and built that featured this circular photodiode array, along with a rate gyro and an encoder used as a reference to compare the orientation estimate gained from the Kalman Filter detailed previously.

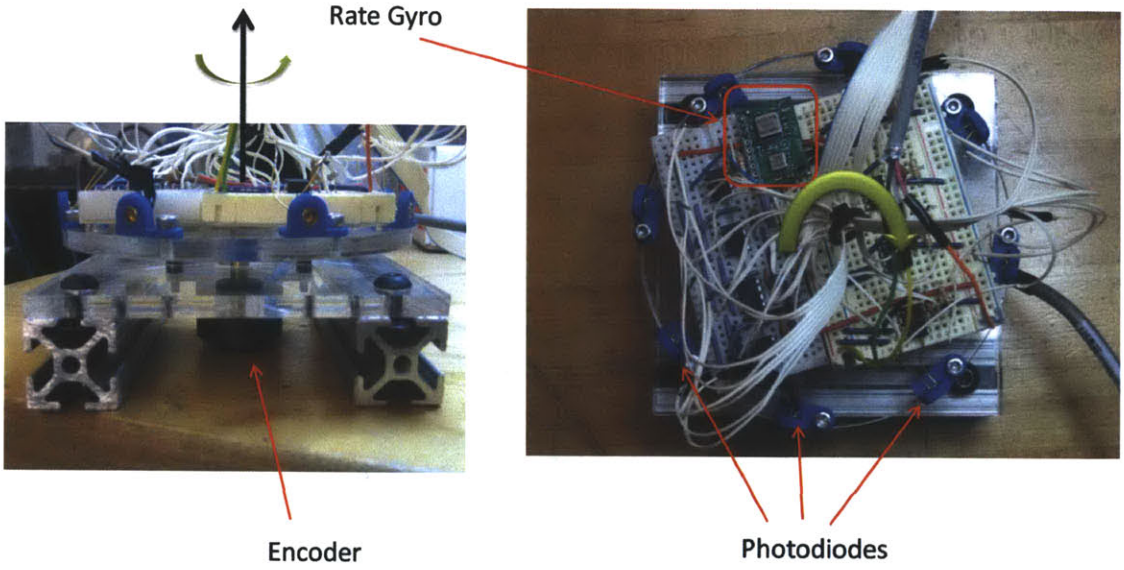

Figure 29 – Experimental setup for demonstration of yaw orientation estimation using an optical communication signal.

A blue (470nm) blue LED array was used as the light source in this setup. For simplicity, the tests were performed in air.

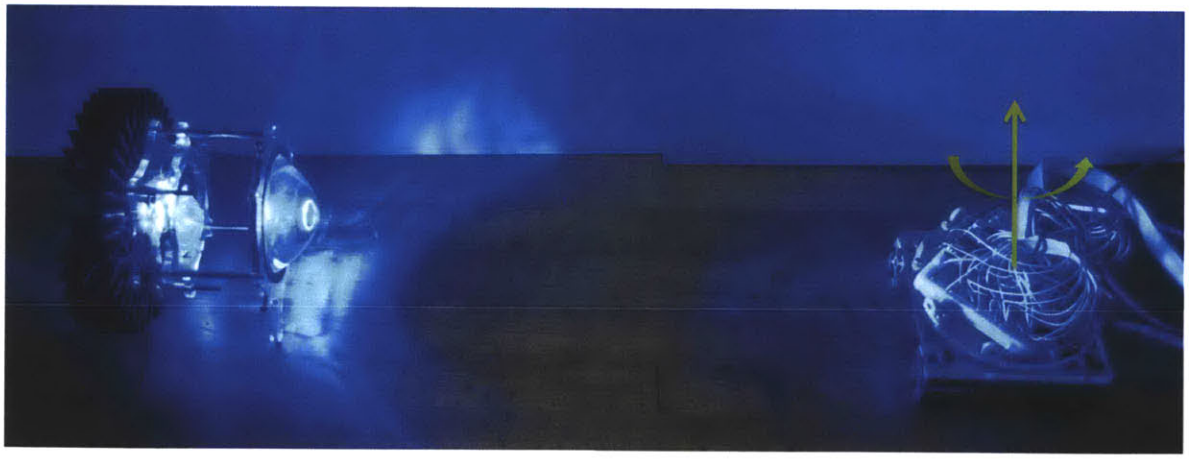

Figure 30 – In-air test setup of the photodiode array based orientation estimation.

Despite the fact that these tests were done in air, it should be noted that nearly identical components were used to establish a 112.5 kbps communication link at ~23m in water. A different photodiode was used in these tests.

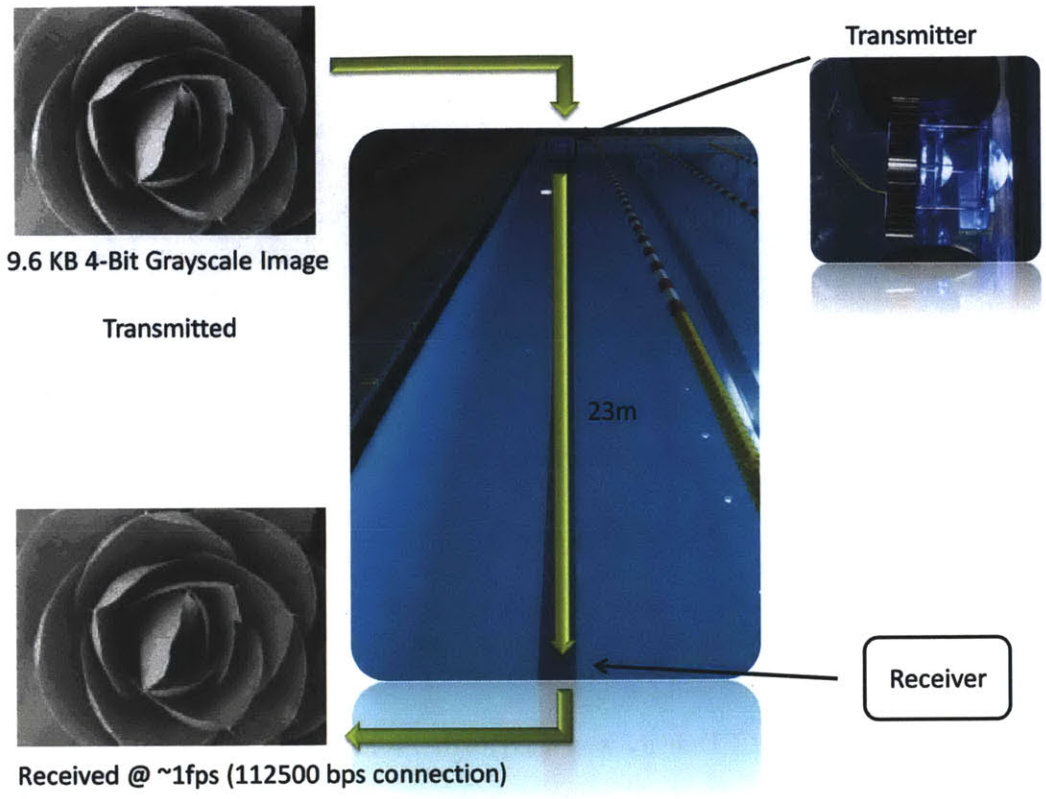

Figure 31 – Experiment for testing of data transfer.

The circular array features 8 transimpedance amplifiers for the 8 photodiodes. This is simply the first step of the filtering process in the receiver circuit used for the communication tests shown previously. The voltages V_n used to compute θ_{pd} are simply the output of this first stage.

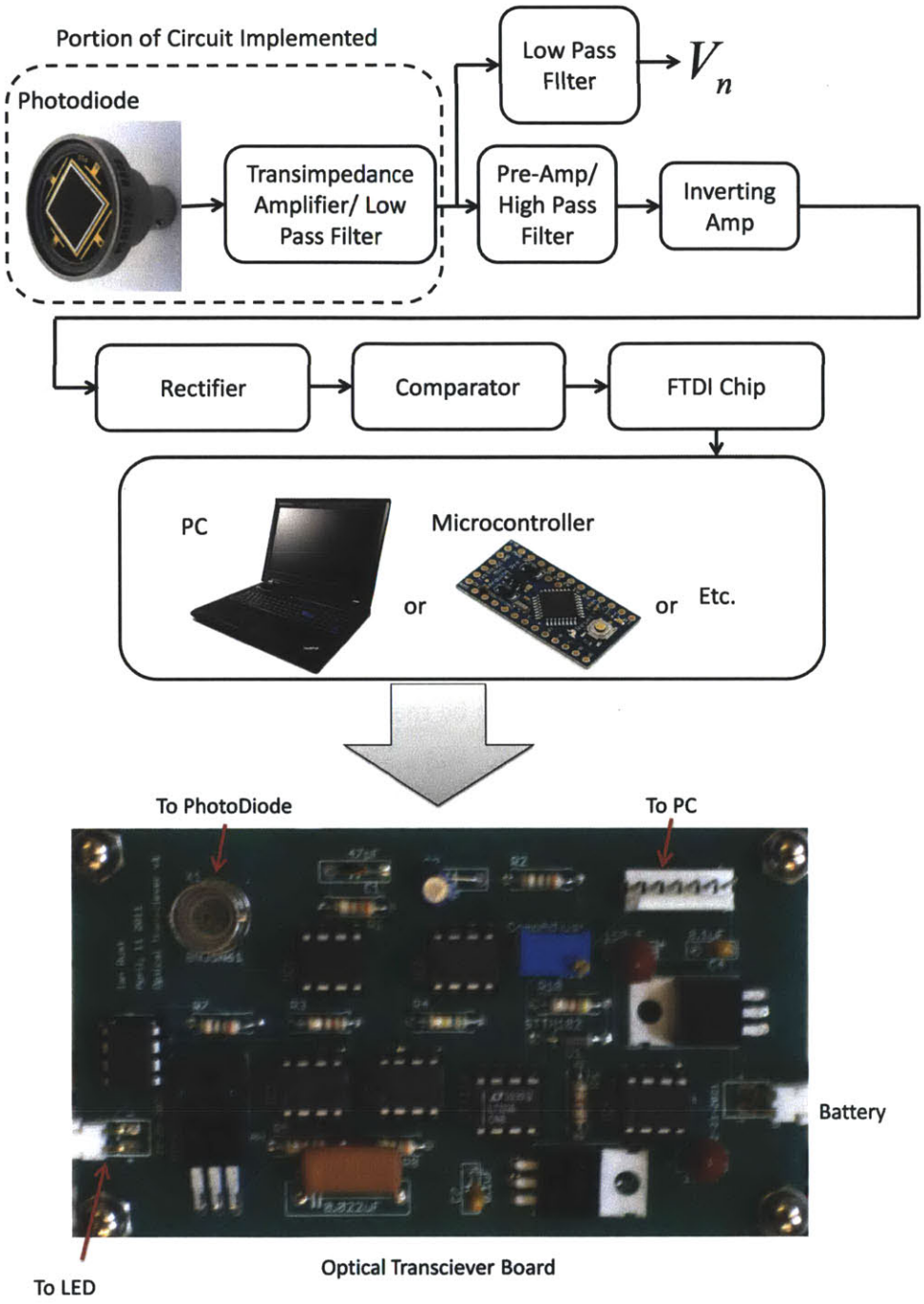

Figure 32 – Block diagram of receiver circuit used for communication and orientation estimation. Note that the portion surrounded by the dashed box alone was implemented during these experiments.

3.3.5. Comments On Range

Of course, as the distance from the light emitter increases, the voltage signals from the transimpedance amplifiers for the photodiodes will diminish to zero. As this occurs, the photodiode array angle measurement will become less reliable, as there will be no discernible difference between the voltage signals on the different photodiodes. This degradation of signal quality can be quantified by a signal to noise ratio:

$$SNR = \left(\frac{A_{signal}}{A_{noise}} \right)^2 \tag{58}$$

In this, A_{signal} is the amplitude of the photodiode signal and A_{noise} is the average amplitude of the noise on this signal. A_{noise} was observed to be approximately 12 mVpp. In order to see how the SNR degrades with distance from the emitter, signal strength values were determined for distances up to 23m. Signal strength was taken to be the peak to peak voltage of the signal from the transimpedance amplifier. The results follow, and are for tests in water:

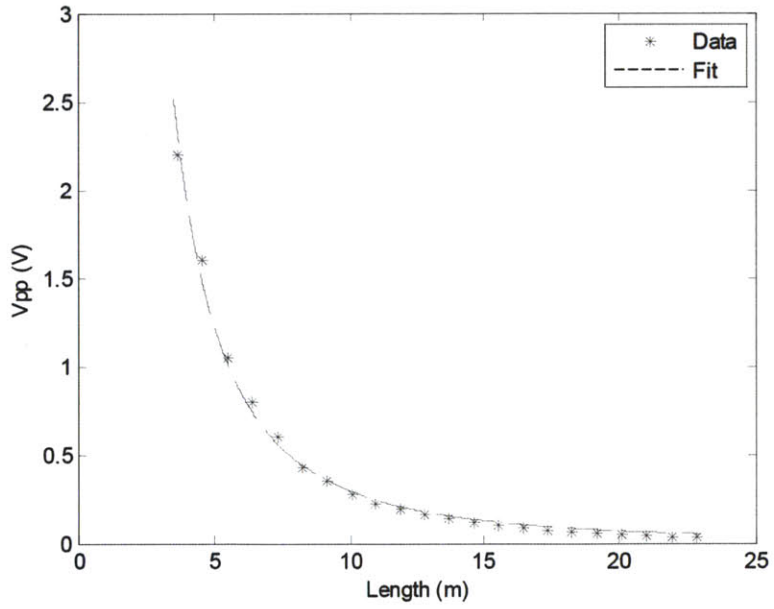

Figure 33 – Signal strength degradation as a function of distance between receiver and transmitter. An exponential fit is overlaid.

In accordance with the Beer-Lambert Law, this degradation was modeled as having an exponential form:

$$A_{sig} = V_{pp} = V_0 e^{-\sigma L} \tag{59}$$

In this V_{pp} is the peak to peak voltage from the transimpedance amplifier, L is the distance between the transmitter and receiver in meters, V_0 is a scaling constant, and σ is the attenuation coefficient. Using a Least-Squares Gaussian fit, V_0 was found to be 31.52 Vpp, and σ was found to be $5.986 \times 10^{-3} \frac{1}{m}$.

Using this fit for V_{pp}, the SNR can be found to be:

$$SNR = \frac{V_0^2}{144 m V_{pp}^2}\left(e^{-2\sigma L}\right) \tag{60}$$

Using this equation, the signal to noise ratio as a function of L can be found, as seen in the subsequent figure.

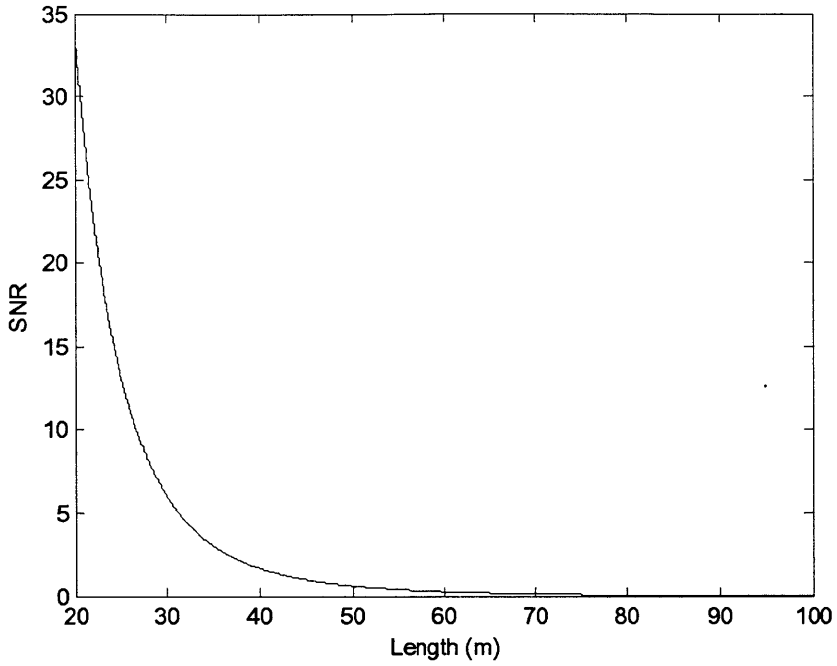

Figure 34 – Signal to Noise Ratio as a Function of Transmitter-Receiver Separation distance, as predicted by a Beer-Lambert Law Model.

Using this model, we are able to predict the distance at which the SNR is equal to 1. This distance is 44.8m. This is at the limit of current optical modems (40m) [3]. As such, this orientation estimation strategy is predicted to function for the same operation range as the communication system. This is to be expected, since this peak to peak voltage is used for the transmission of data, as well as for orientation estimation.

3.3.6. Results

Data was taken in which the platform pictured previously (see Figure 29) was rotated by hand, and the Kalman Filter was applied to the resulting gyro and photodiode array data. The light source was turned on, and the image data from Figure 31 was overlaid using On-Off Keying (OOK) encoding. A plot of these two signals, along with the resulting filtered output, is shown in Figure 35. The values for the noise covariance matrices can be found in Table 3, and were hand-tuned.

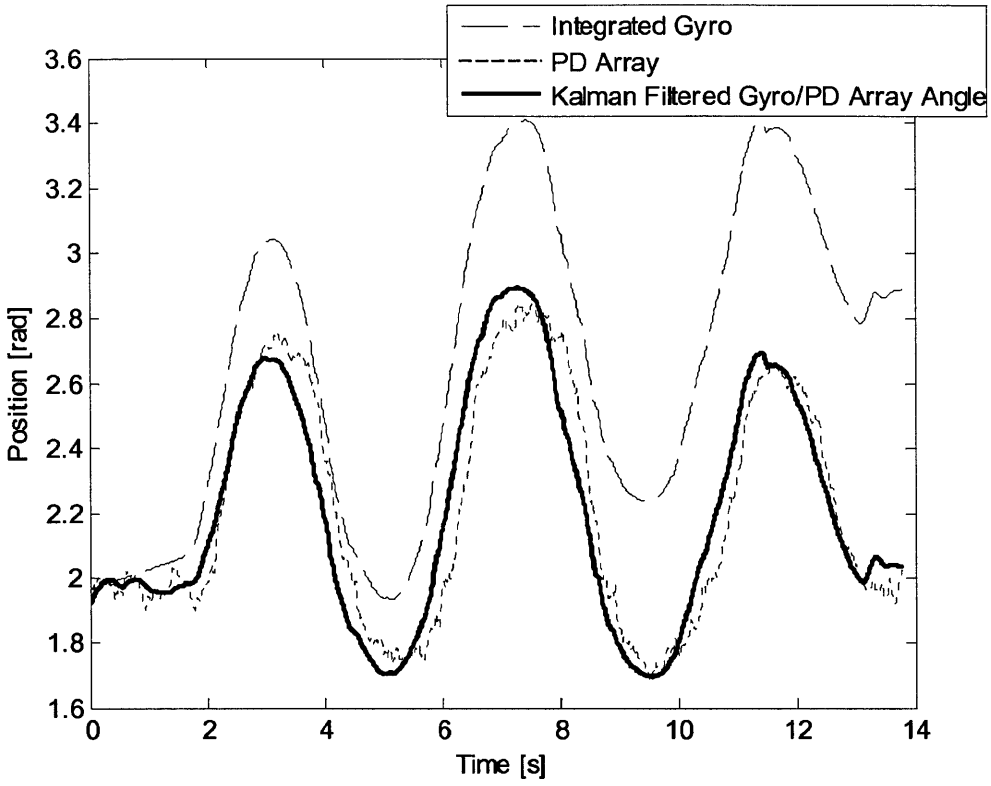

Figure 35 – Result of Kalman filter applied to optical orientation estimation system.

The following covariance matrices for the process and measurement noise were used. The measurement noise covariance was measured from data obtained from the photodiode array. The process noise was measured by measuring the noise on the rate gyro (for q_{11}). This process noise comes from a measurement because the dynamic model is based on kinematics, and the rate gyro is the input into this kinematic system. The other elements were tuned for best response of the filter, since this process noise was not directly measured. The process noise is assumed to be uncorrelated.

Table 3 – Covariance Matrices for Process and Measurement Noise used in the Discrete Kalman Filter Implementation

Matrix	Physical Meaning	Value
Q	Process Noise Matrix	$\begin{bmatrix} 1.28\times10^{-7} & 0 & 0 \\ 0 & 1\times10^{-11} & 0 \\ 0 & 0 & 1\times10^{-11} \end{bmatrix}$
R	Measurement Noise Matrix	9.4×10^{-4}

For a comparison, the output of the Kalman Filter was plotted alongside the true orientation measurement from the optical encoder (see Figure 36).

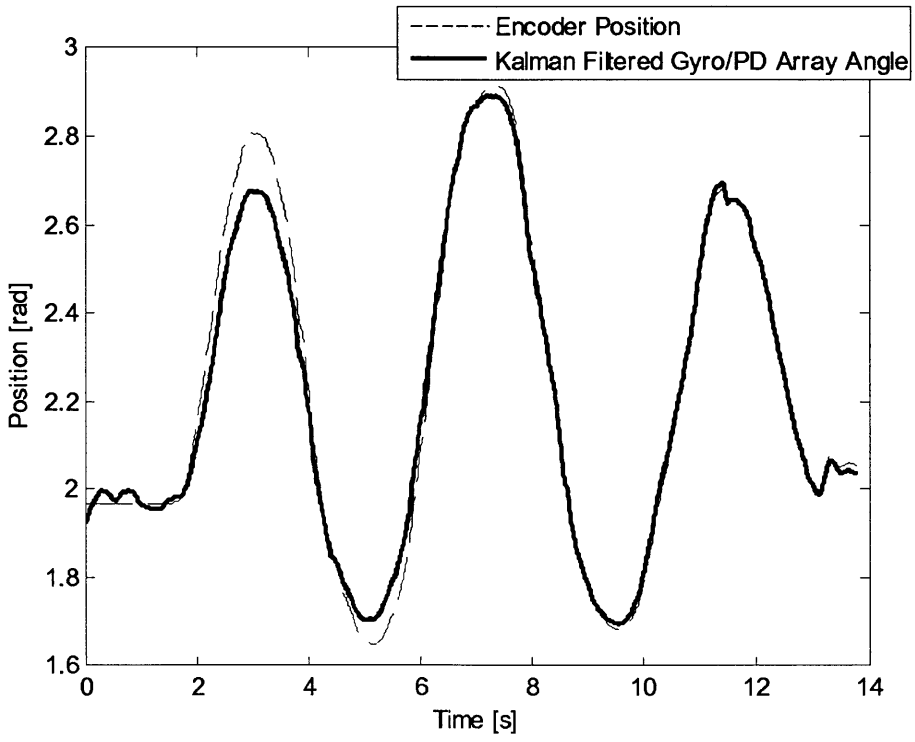

Figure 36 – Comparison of Kalman filter based Estimation of yaw orientation angle and the actual yaw orientation angle, measured by an encoder.

As can be seen, the Kalman Filter, using this photodiode array signal as the update signal, is able to successfully measure the orientation of the body in the yaw direction.

3.4. Full Planar Localization

3.4.1. Extension of the Dual Use System

These experiments demonstrate a method for orientation estimation for underwater vehicles using a dual-use system. By using the same components used for an optical communication system, this thesis presents a system for accurate orientation estimation using the light source with which data is transmitted. In this way, we present a dual-use system, one that is capable of both orientation estimation and long–distance, high-speed communications in water. Each of these is of vital importance to numerous underwater robotic applications.

However, there is one problem with this strategy, which has been mentioned previously. This comes from the fact that we assume for these initial experiments that the ROV does not translate. While useful in demonstrating and testing the concept of a dual use system using the visible light system, this is not a realistic system. The Eyeball ROV, or any other ROV which would use this system, would obviously need to translate and move in different directions in order to perform the tasks required of it (e.g. inspection). As such, we must modify the algorithm presented previously to take into account such translations.

3.4.2. Kinematic Model

To modify our localization algorithm, we must define two new coordinates for the system, the distance from the light source at the ground station to the ROV d, and the angle from the light source to the ROV, θ_d. The system is kept constrained to motion in the x-y plane in order to reduce complexity. Of course, we keep the gyro bias b as a state as well as the orientation of the ROV θ, renaming it θ_{ROV}. For a visual explanation of these variables, refer to the figure below:

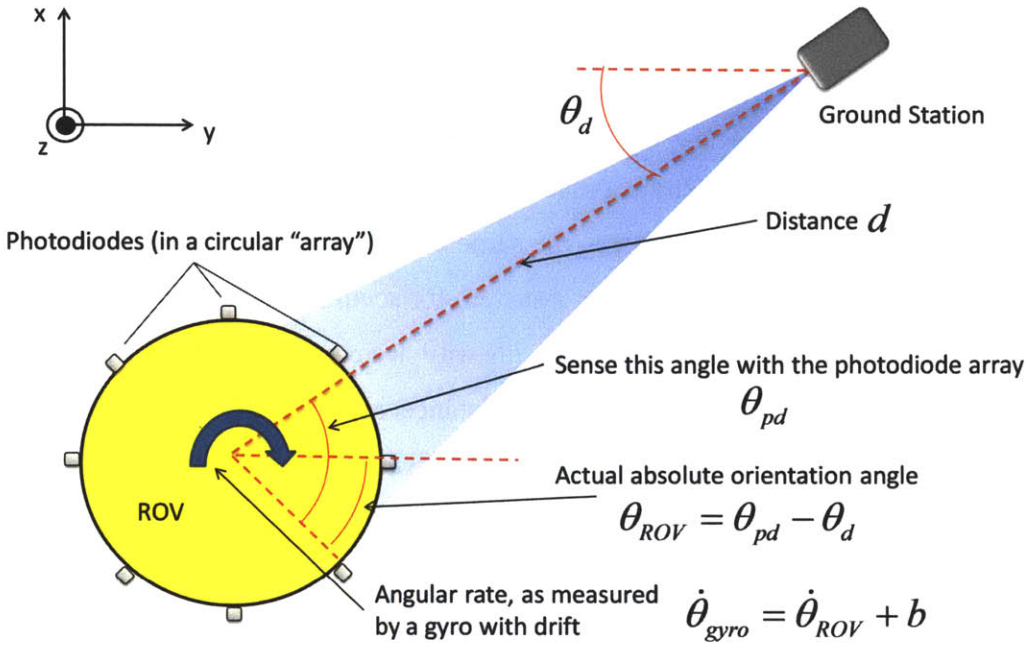

Figure 37 - Architecture for sensing absolute orientation angle θ_{ROV} of the ROV. This takes into account motions of the ROV, which is taken into account by the angle of the ROV relative to the light source, θ_d.

In this new system, the ROV would once again seek to estimate θ_{ROV}, and in doing so it must also estimate θ_d. To do this, we set up the following kinematic model, which once again integrates and removes the drift b from a gyro signal by referencing this with the driftless measurement from the photodiode array. We do this by using the rate gyro signal as an input, and then integrating this signal, while subtracting an estimate for b.

$$x_k = \begin{bmatrix} \theta_{ROV} \\ \dot{\theta}_{ROV} \\ \theta_d \\ b \end{bmatrix}_k = \begin{bmatrix} 1 & \Delta t & 0 & 0 \\ 0 & 0 & 0 & -1 \\ 0 & 0 & 1 & 0 \\ 0 & 0 & 0 & 1 \end{bmatrix} \begin{bmatrix} \theta_{ROV} \\ \dot{\theta}_{ROV} \\ \theta_d \\ b \end{bmatrix}_{k-1} + \begin{bmatrix} 0 \\ 1 \\ 0 \\ 0 \end{bmatrix} \theta_{gyro_k} + Gw(t) = Ax_{k-1} + Bu_k + Gw(t) \qquad (61)$$

$$y = \theta_{pd} = \theta_{ROV} + \theta_d + v(t) = \begin{bmatrix} 1 & 0 & 1 & 0 \end{bmatrix} x_k + v(t) = Hx_k + v(t) \qquad (62)$$

Unfortunately, if one examines the observability matrix of this system, we discover that the system is unobservable. Stated mathematically, we can qualify this in the following manner:

$$rank\begin{pmatrix} H \\ HA \\ HA^2 \\ HA^3 \end{pmatrix} < 4 = \dim(x_k) \tag{63}$$

This follows intuition, as there is seemingly no sensor to determine the angle θ_d. In addition, this model neglects entirely the distance from the ground station to the ROV, d. Therefore we must modify the model in order to account for these discrepancies.

3.4.3. Dynamic Model

The first modification to the model is to add dynamics to the model, since by the previous analysis a kinematic model is shown to be deficient in estimating both d and θ_d, and these can be predicted more readily with knowledge of the dynamics of the ROV.

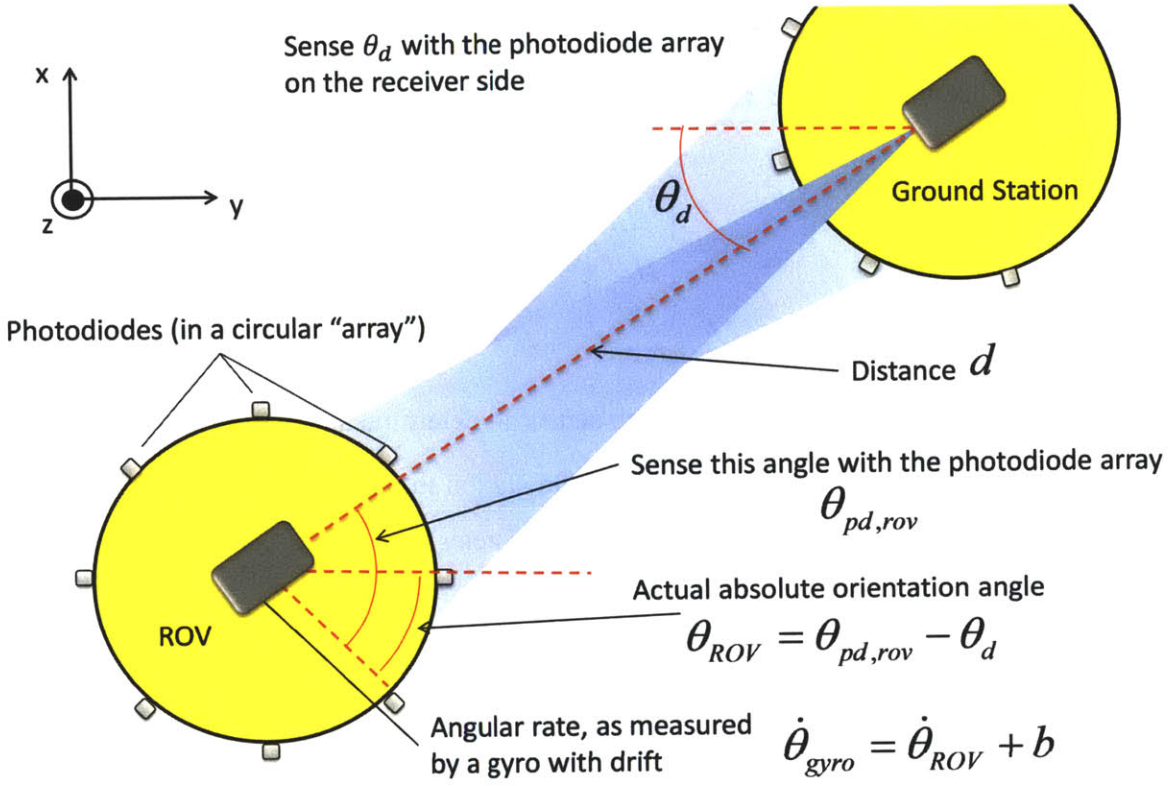

Figure 38 – Modified architecture for estimation of both the position (parameterized by d and θ_d), and orientation of the ROV. Note that there is a light source on both the ROV and ground station.

The second modification will be to add a second sensor to the system. Since a sensor is needed for the drift angle θ_d, it is simplest to add a sensor at the light source in order to measure this angle directly. Relying on the fact that there would be a bi-directional communication link (i.e. light sources on both the ROV and the ground station), we can place a photodiode array on the ground station (see Figure 38). This allows for direct measurement of θ_d. The presence of a bi-directional link not only provides an optical signal to measure the angle, but also the ability to transmit the angle reading to the ROV. This is essential due to the fact that ROV does not directly measure θ_d. Instead, the ground station does. Therefore, the ground station must relay this measurement to the ROV. Fortunately, since this is a system for both localization and communication, we can rely on the communication functionality of the system in order to relay the measurement of θ_d to the ROV.

The third modification is to add a sensor for the measurement of the distance d. There has been some work into measuring distance using an optical communication signal. One example of such work, carried out by *Schill, et al*, measured distance using data transfer and error rates [44]. In addition, other work on using signal strength for distance measurement has been done extensively for radio communications [47], [48], [49]. This thesis however, proposes that we use the signal strength from the optical transceiver to indirectly measure distance between the ROV and ground station.

Therefore, the sensor chosen for this once again relies on the optical signal. Specifically, the signal strength received by the photodiode array will function as this sensor, since it is related to the distance separating the sensor. Recalling equation (59), we can see that the signal strength is a function of the distance d, according to the following exponential relationship:

$$V_{pp} = V_0 e^{-\sigma d} \tag{64}$$

In this, σ is the attenuation coefficient, d is the distance between the transmitter and the receiver, and V_0 is essentially the signal strength at zero distance. This essentially follows from the Beer-Lambert law, which dictates the attenuation of an electromagnetic signal through a medium. In this equation, there are two parameters. The first, σ, is a well-known attenuation constant that can either be found in literature or measured directly. Unfortunately, V_0, the signal strength at zero distance, cannot be looked up or measured. This is because it is a function of a wide array of variables, including battery charge, condition of the photodiode or LED, etc. Therefore, we must estimate this parameter. As such, we will include it as a system state.

With these sensors established, we can reconstruct out state vectors to include the dynamics as well as the calibration parameters, b and V_0, which both must be estimated.

$$x = \begin{bmatrix} \theta_{rov} & \dot{\theta}_{rov} & d & \dot{d} & V_0 & b & \theta_d & \dot{\theta}_d \end{bmatrix}^T \tag{65}$$

Using Newtonian mechanics as well as knowledge of the calibration parameters, the dynamics of this new dynamic system can be defined as such:

$$\dot{x} = \begin{bmatrix} \dot{\theta}_{rov} \\ \dfrac{M - C_{rot}\dot{\theta}_{rov}}{I_{ROV}} \\ \dot{d} \\ d\dot{\theta}_d^2 - \dfrac{C_d\dot{d} + F_T\cos(\theta_{rov} - \theta_d + \theta_T)}{m} \\ 0 \\ 0 \\ \dot{\theta}_d \\ -2\dfrac{\dot{d}\dot{\theta}_d}{d} - \dfrac{C_d\dot{\theta}_d + \dfrac{F_T}{d}\sin(\theta_{rov} - \theta_d + \theta_T)}{m} \end{bmatrix} \tag{66}$$

In this, M is the control moment, F_T is the control thrust, θ_T is the direction of this control thrust relative to the ROV, C_d is the linear drag coefficient, C_{rot} is the rotational drag coefficient. I_{ROV} is the rotational inertia of the ROV, and m is the mass of the ROV. All of these parameters are assumed to be known.

By making a first order Euler approximation, the dynamics can be discretized in the following manner:

$$x_{k+1} = x_k + \dot{x}_k\Delta t + w_k = f(x_k, u_k) + w_k \tag{67}$$

In this, u_k is the control input.

$$u_k = \begin{bmatrix} M & F_T & \theta_T \end{bmatrix}^T_k \tag{68}$$

In this, w_k is the process noise in the system, with covariance $Q \in \mathbb{R}^{8x8}$.

The measurements used during the update phase of the Kalman Filter are the signal strength, rate gyro reading, as well as the angular position of highest signal strength (via the PD arrays) on both the ground station as well as the ROV. Note that this is made possible by using the communication link between the ROV and ground station in order to transmit a measurement of θ_d to the ROV.

Therefore the measurement equation is as follows:

$$y_k = \begin{bmatrix} V_{pp} \\ \dot{\theta}_{gyro} \\ \theta_{pd,rov} \\ \theta_{pd,rec} \end{bmatrix} = \begin{bmatrix} V_0 e^{-\sigma d} \\ \dot{\theta}_{rov} + b \\ \theta_{rov} - \theta_d \\ \theta_d \end{bmatrix} + v_k = h(x_k) + v_k \tag{69}$$

In this, v_k is the measurement noise, with covariance matrix $R \in \mathbb{R}^{4x4}$. In addition, V_{pp} is the signal strength, $\dot{\theta}_{gyro}$ is the angular rate of the ROV measured by a rate gyro, $\theta_{pd,rov}$ is the angle measurement from the photodiode array onboard the ROV, and $\theta_{pd,rec}$ is the angle measurement from the photodiode array onboard the ground station.

With the dynamics and measurement specified, we can implement the discrete Extended Kalman Filter (EKF). An EKF is necessary due the nonlinearity of the dynamics and measurements of the system. To implement the EKF, the state is first initialized to an initial value. This is an arbitrary choice, however the EKF performs better if the initialized state of the filter is close to the initialized state of the actual ROV. This is due to the nonlinear nature of both the dynamics and measurement equations. Since a linearization must be taken for the operation of the filter, the performance of the EKF depends highly on how close these linearizations are to the actual equations. Hence, if the dynamics are linearized at a different state than the actual state, for example in the case of having drastically different initialized states, the EKF will not accurately estimate the state.

Once this initialization is done, the EKF can be run recursively. First is the prediction phase, in which the a priori state $\hat{x}_{k|k-1}$ and covariance are computed in the following manner:

$$\hat{x}_{k|k-1} = f(\hat{x}_{k-1|k-1}, u_{k-1}) \tag{70}$$

$$P_{k|k-1} = F_{k-1} P_{k-1|} F_{k-1}^{\ T} + Q \tag{71}$$

F_{k-1} is the linearized state transition matrix, defined as follows:

$$F_{k-1}=\left.\frac{\partial f}{\partial x}\right|_{\hat{x}_{k-1|k-1},u_{k-1}}=\begin{bmatrix} 1 & \Delta t & 0 & 0 & 0 & 0 & 0 & 0 \\ 0 & 1-\Delta t\frac{C_{ROT}}{I_{ROV}} & 0 & 0 & 0 & 0 & 0 & 0 \\ 0 & 0 & 1 & \Delta t & 0 & 0 & 0 & 0 \\ \Delta t\frac{F_{T_k}\cos\theta_e}{m}\sin\left(\theta_{ROV_k}-\theta_{d_k}+\theta_T\right) & 0 & \Delta t\dot{\theta}_{d_k}^2 & 1-\Delta t\frac{C_d}{m} & 0 & 0 & \Delta t\frac{F_{T_k}\cos\theta_e}{m}\sin\left(\theta_{ROV_k}-\theta_{d_k}+\theta_T\right) & 2\Delta t d_k\dot{\theta}_{d_k} \\ 0 & 0 & 0 & 0 & 1 & 0 & 0 & 0 \\ 0 & 0 & 0 & 0 & 0 & 1 & 0 & 0 \\ 0 & 0 & 0 & 0 & 0 & 0 & 1 & \Delta t \\ -\Delta t\frac{F_{T_k}\sin\theta_e}{md_k}\cos\left(\theta_{ROV_k}-\theta_{d_k}+\theta_T\right) & 0 & -\frac{\Delta t}{d_k^2}\left[2\dot{d}_k\dot{\theta}_{d_k}+\frac{F_{T_k}\sin\theta_e}{m}\sin\left(\theta_{ROV_k}-\theta_{d_k}+\theta_T\right)\right] & -\frac{2\Delta t\dot{\theta}_{d_k}}{d} & 0 & 0 & \Delta t\frac{F_{T_k}\sin\theta_e}{m}\cos\left(\theta_{ROV_k}-\theta_{d_k}+\theta_T\right) & 1-\Delta t\left[\frac{C_d}{m}-2\frac{\dot{d}_k}{d_k}\right] \end{bmatrix} \tag{72}$$

This is essentially a linearized version of the dynamic model, where the linearization point is the last a posteriori state estimate.

Once these a priori estimates are made, the update procedure is carried. First the Kalman gain is calculated.

$$K_k = P_{k|k-1}H_k{}^T\left(H_kP_{k|k-1}H_k{}^T+R\right)^{-1} \tag{73}$$

Note that H_k is the observation matrix, defined as the linearization of the measurement equation. The linearization point is the last a posteriori state estimate.

$$H_k=\left.\frac{\partial h}{\partial x}\right|_{x=\hat{x}_k,u=u_k}=\begin{bmatrix} 0 & 0 & -\sigma V_{0_k}e^{-\sigma d_k} & 0 & e^{-\sigma d_k} & 0 & 0 & 0 \\ 0 & 1 & 0 & 0 & 0 & 1 & 0 & 0 \\ 1 & 0 & 0 & 0 & 0 & 0 & -1 & 0 \\ 0 & 0 & 0 & 0 & 0 & 0 & 1 & 0 \end{bmatrix} \tag{74}$$

Then the updated state estimate is computed.

$$\hat{x}_{k|k}=\hat{x}_{k|k-1}+K_k\left(z_k-h(\hat{x}_{k|k-1})\right) \tag{75}$$

Finally, the updated covariance matrix is computed.

$$P_{k|k}=\left(I_{8\times 8}-K_kH_k\right)P_{k|k-1} \tag{76}$$

These predict and update procedures are then repeated in this recursive manner.

With this dynamic model, the system is observable. This can be seen by examining the observability matrix.

$$rank\begin{pmatrix} H \\ HA \\ HA^2 \\ HA^3 \end{pmatrix} = 8 = \dim(x_k) \tag{77}$$

Once the state is estimated, some basic control tasks can be enacted using these estimated states as feedback variables. Firstly we use the estimates of θ_{ROV_k} and θ_{d_k} in order to point the thrust vector enacted on the ROV to a specific direction in inertial space. Specifically, this corresponds to setting the direction θ_T.

$$\theta_T = \hat{\theta}_{d_k} - \hat{\theta}_{ROV_k} + \theta_{desired} \tag{78}$$

Most importantly, we enact rotational control in order to "point" the LED affixed to the body of the ROV to toward the ground station. This is done by implementing the following proportional controller, with the control moment M as the control input. The control law is as follows:

$$M = -K_p\left(\hat{\theta}_{rov_k} - \hat{\theta}_{d_k}\right) \tag{79}$$

Essentially, this control algorithm attempts to control θ_{rov} to be identical to θ_d. This corresponds to pointing the ROV as well as the LED fixed to the ROV.

3.4.4. Simulation Results

This EKF localization algorithm was applied to the system in simulation. The process and measurement noise covariances were set according to the values seen in the subsequent table.

Table 4 - Covariance Matrices used in simulations of the EKF localization algorithm.

Matrix	Physical Meaning	Value
Q	Process Noise Matrix	$1\times10^{-6}\cdot I_{8\times8}$
R	Measurement Noise Matrix	$1\times10^{-3}\cdot I_{4\times4}$

As can be seen, the noise is assumed to be uncorrelated.

In simulation, the ROV state was initialized at a position, and the state estimate $\hat{x}_{k|k}$ was initialized to be approximately equal to the initial ROV state. The simulation was 3 minutes long, with 3 distinct phases. These correspond to 3 distinct directions for $\theta_{desired}$:

$$\theta_{desired} = \begin{cases} -\frac{\pi}{2} & \text{for } 0\text{s} < t \le 60s \\ -\frac{\pi}{4} & \text{for } 60\text{s} < t \le 120s \\ \frac{\pi}{2} & \text{for } 120\text{s} < t \le 160s \end{cases} \tag{80}$$

Note that the thrust force F_T is held at a constant 10mN.

In addition, rotation control was enacted, using the control law seen in (79). K_p was set to be 0.01. The results follow. For a table containing the physical parameters used in the simulation, including drag coefficients, masses, and moments of inertia, refer to Table 7.

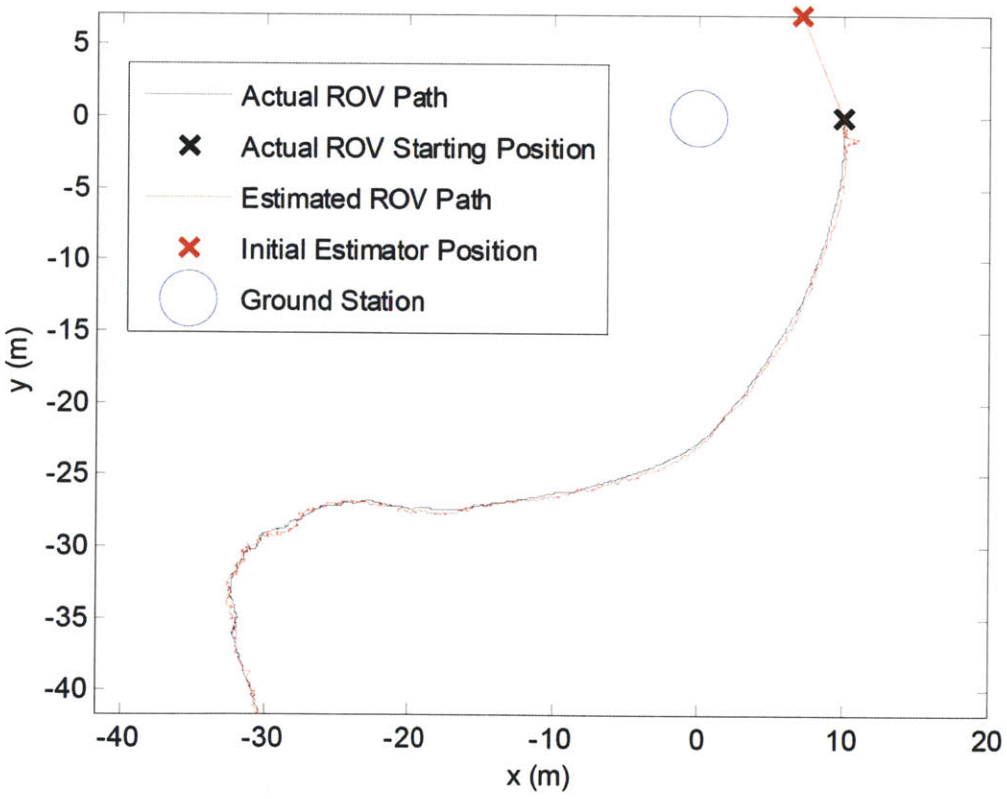

Figure 39 - Top-down view of the results of tracking the path of an ROV traveling in x-y space.

As seen in the above figure, the Extended Kalman Filter is successful in localizing the ROV. In addition, the "aiming" control used to point the LED on the ROV back to the ground station is successful, as shown in the following plot.

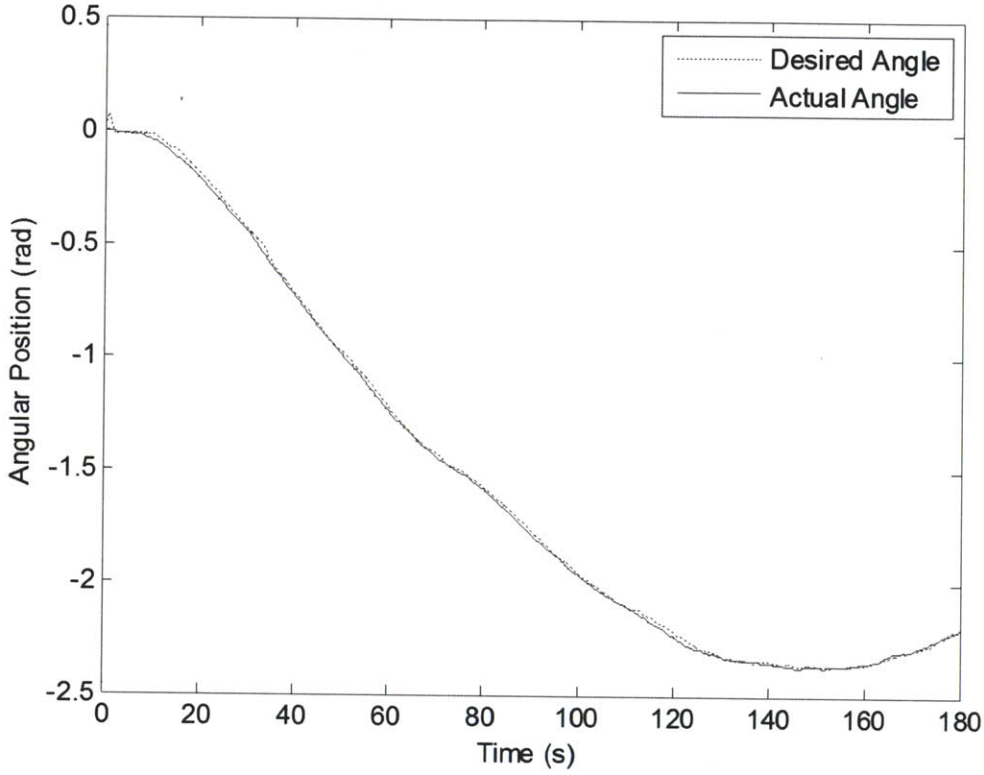

Figure 40 - Orientation control of the ROV using the EKF state estimate as feedback variables.

As can be seen, this EKF localization algorithm is successful in localizing the ROV. In addition, this state estimate can be used effectively as a feedback signal. This is done in a novel manner using an optical modem, and the associated visible light signal, as key components.

3.4.5. Experimental Results

In order to test the 2-D EKF localization algorithm presented in this thesis, we designed a wireless raft equipped with a bi-directional optical modem, a photodiode array, a rate gyro, and four thrusters.

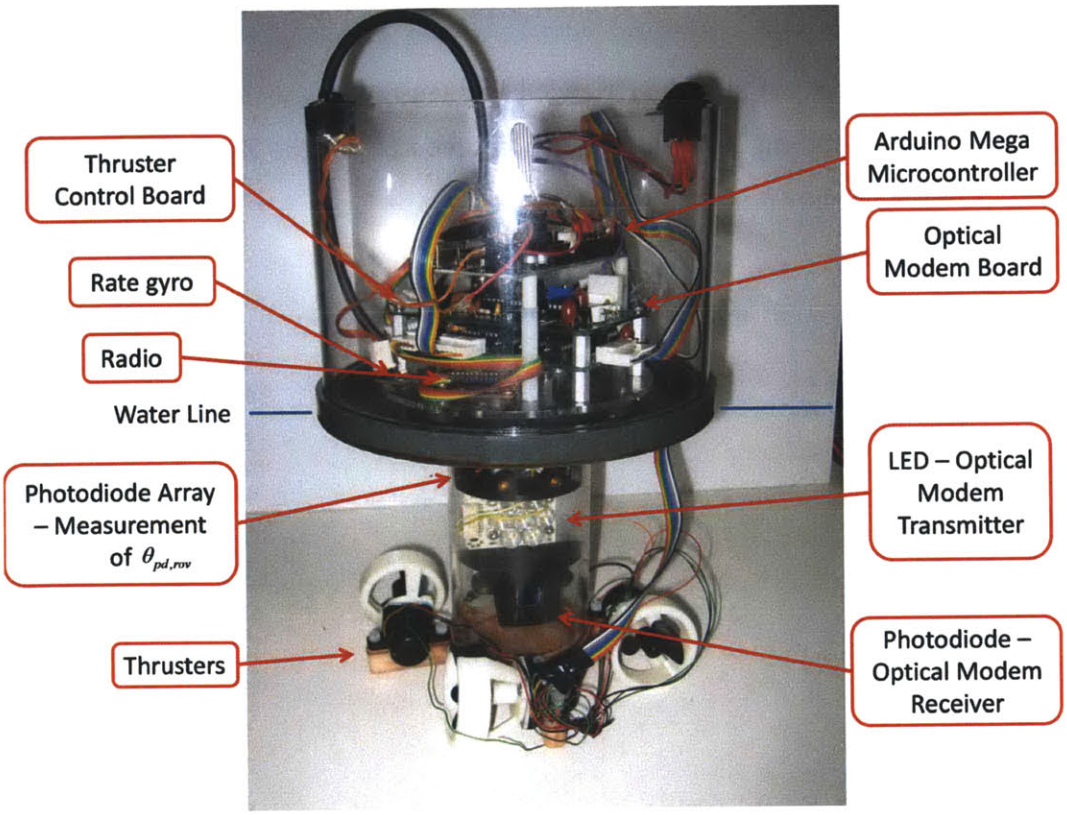

Figure 41 – Raft used to test the Extended Kalman Filter localization algorithm. Important components are annotated.

This raft had an associated ground station, which also featured a bidirectional modem and a photodiode array.

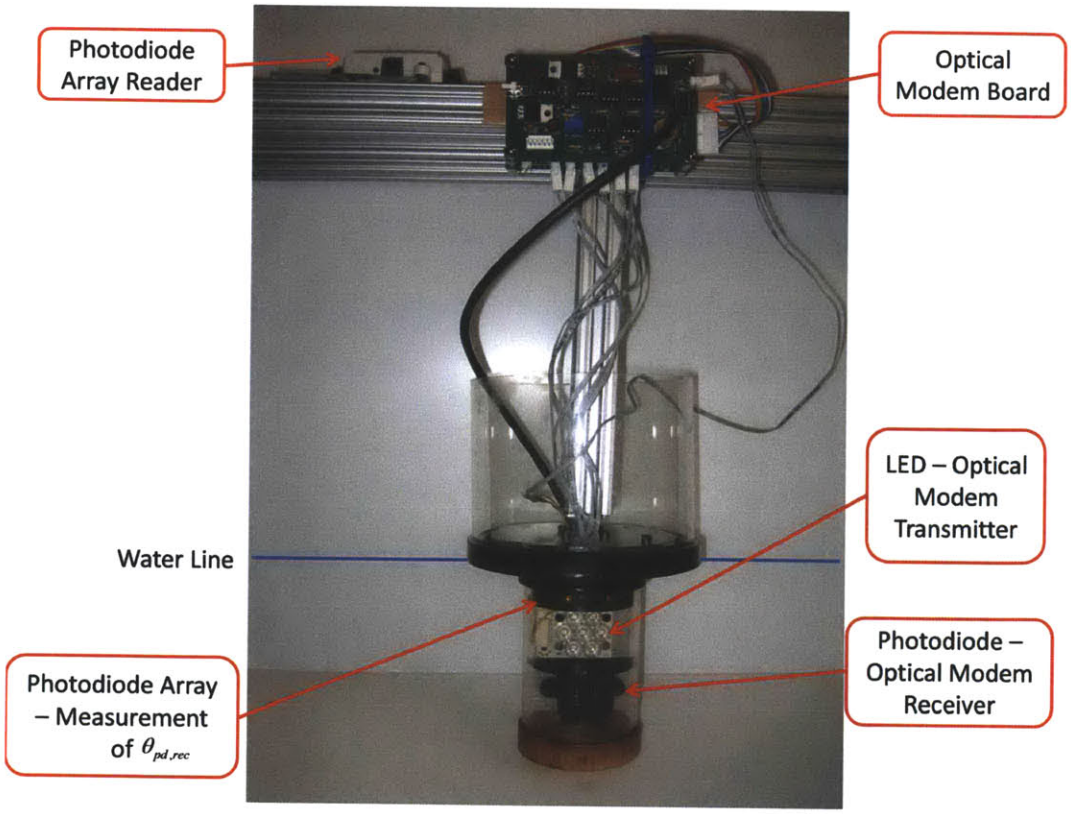

Figure 42 – Ground Station used to test the Extended Kalman Filter localization algorithm. Important components are annotated.

The objective of this raft was to estimate its own position relative to this ground station. In this way, we constructed the system to be identical to that seen in Figure 38.

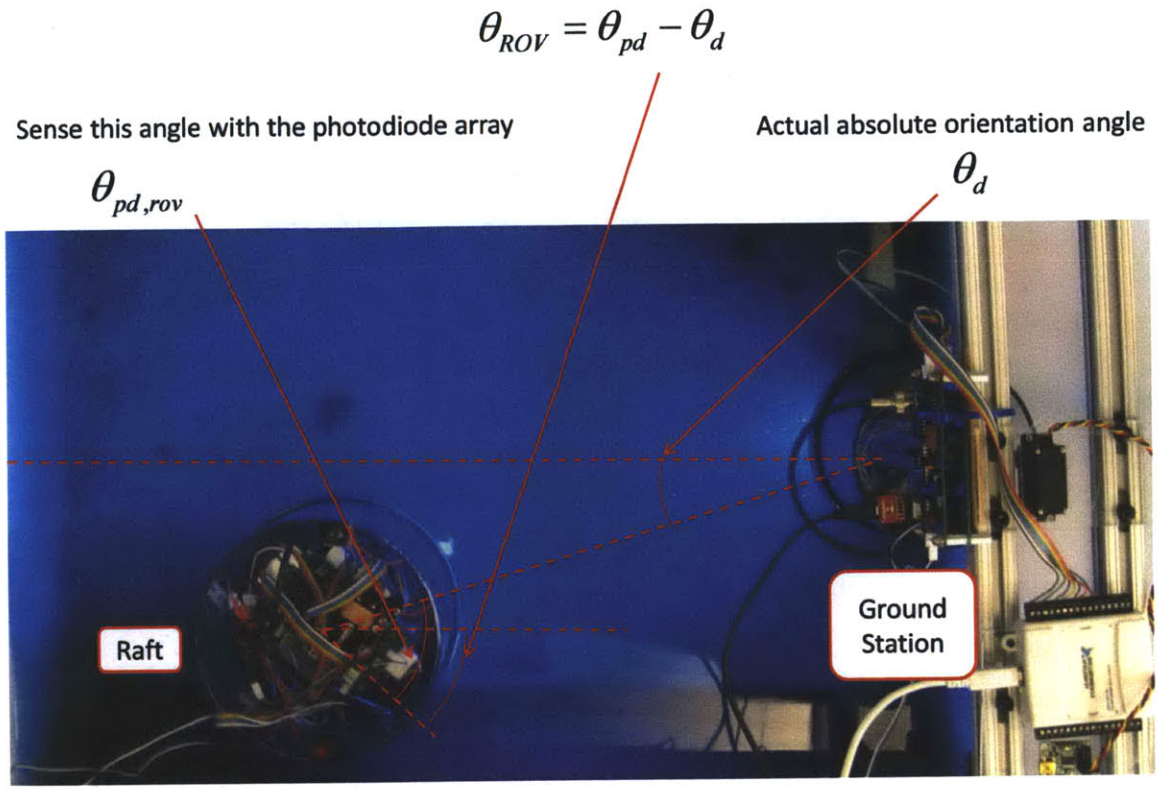

Figure 43 – Top-down view of the experimental setup used to test the Extended Kalman Filter (EKF) localization algorithm.

A nearly identical Extended Kalman Filter (EKF) localization algorithm as the one demonstrated previously was used. The only difference was that, for simplicity, the data processing and computation was done on a PC running MATLAB. This was the same PC used to pilot the vehicle. A full block diagram detailing the flow of data can be seen in the subsequent figure. All computation of the EKF was identical to that seen in (70)-(76).

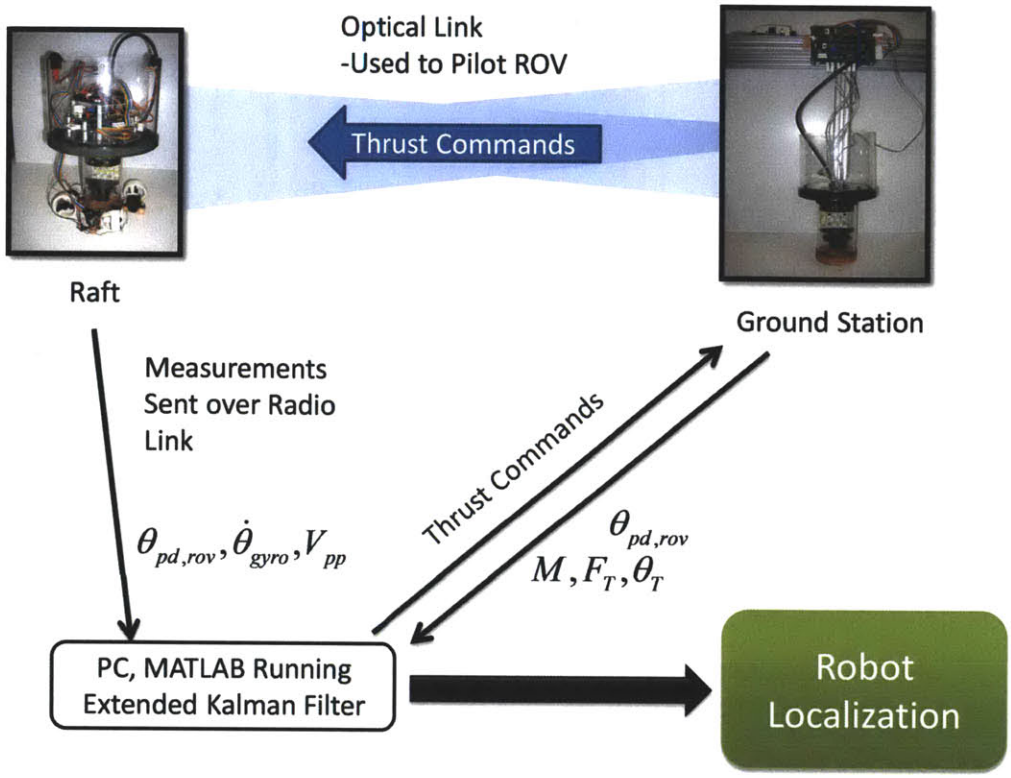

Figure 44 – Block diagram of the implementation of the EKF localization algorithm. Note that all computation for the robot location is done on a PC running MATLAB. As such, all measurements from the raft are relayed to the PC over a radio link.

The other difference was that the control law to "point" the raft back to the ground station was modified slightly. Instead of using the estimate computed using the EKF, as in (79), we used the direct measurement of the heading angle from the raft.

$$M = -K_p\left(\theta_{pd,rov}\right) \tag{81}$$

This was done in order to simplify implementation, as well as to solve a latency issue caused by performing computation on the PC.

In order to test the localization algorithm, the raft was required to move about the test tank. This was done using open-loop commands sent over the optical communication link. Keyboard inputs were translated into up, down, left, and right motions from the raft, and in doing so the raft was piloted in an arbitrary manner about the tank. The localization algorithm was used to estimate the position of the raft in the tank. The photodiode array on the ground station was

used to gain the measurement $\theta_{pd,rec}$. The photodiode array on the raft was used to gain the measurement $\theta_{pd,rov}$ as well as the measurement of the signal strength V_{pp}. In addition, the gyro onboard the raft was used to measure $\dot{\theta}_{gyro}$. These four measurements make up the measurement equation seen in (69).

Using these measurements, and the same model seen in (66), the EKF was implemented to localize the raft while the raft was piloted using a signal sent over the optical data link. The covariance model matrices can be seen in the following table. These values were hand-tuned.

Table 5 - Covariance Matrices used in experimental tests of the EKF localization algorithm.

Matrix	Physical Meaning	Value
Q	Process Noise Matrix	$diag\left(\begin{bmatrix} 1 & 1 & 1\times10^{-2} & 1\times10^{-3} & 1 & 1 & 1\times10^{-2} & 1\times10^{-3} \end{bmatrix}\right)$
R	Measurement Noise Matrix	$I_{4\times4}$

The results of the EKF can be seen in the following figure. For a table containing the physical parameters used in these tests, including drag coefficients, masses, and moments of inertia, refer to Table 8. The actual position was measured using a video camera mounted above the test tank.

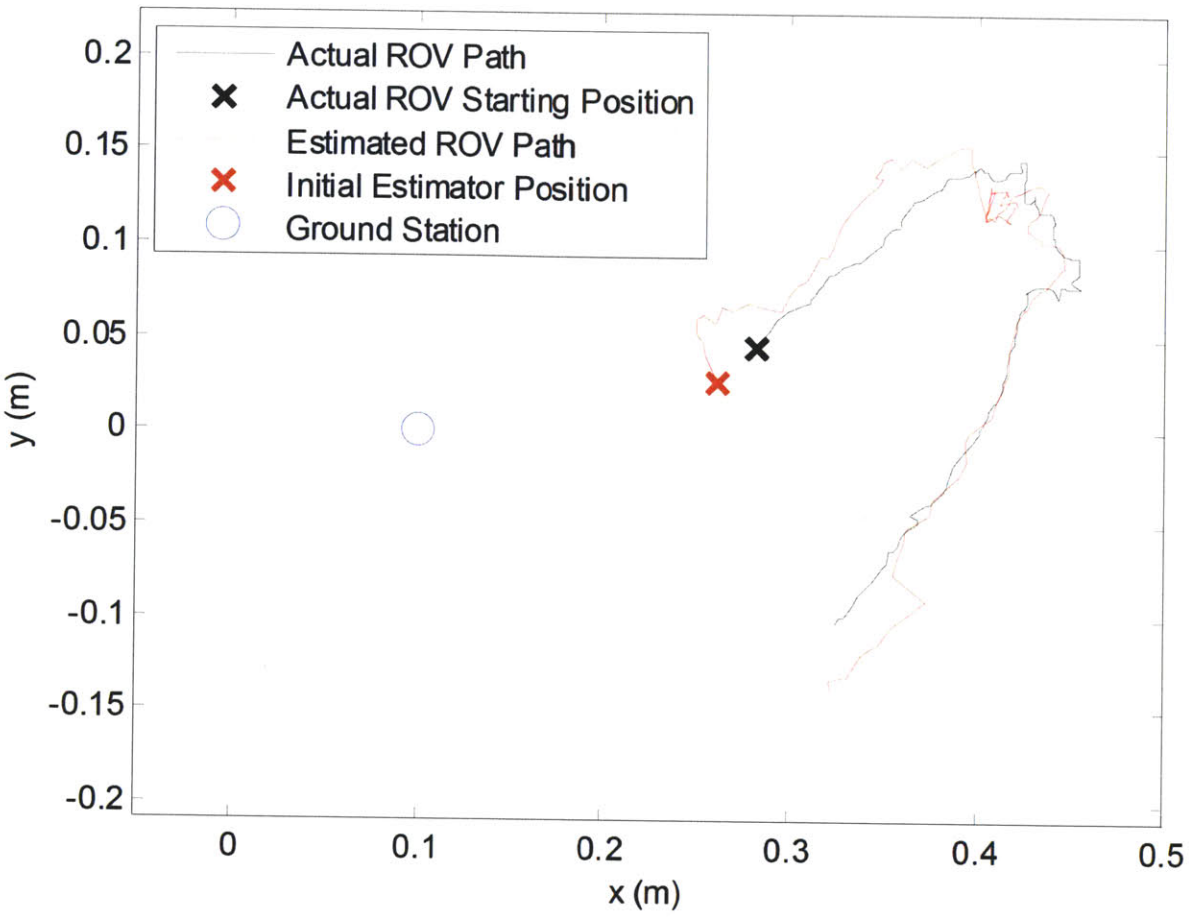

Figure 45 – Experimental results of the EKF localization algorithm.

A plot of the squared error of this EKF localization algorithm can be found the following plot.

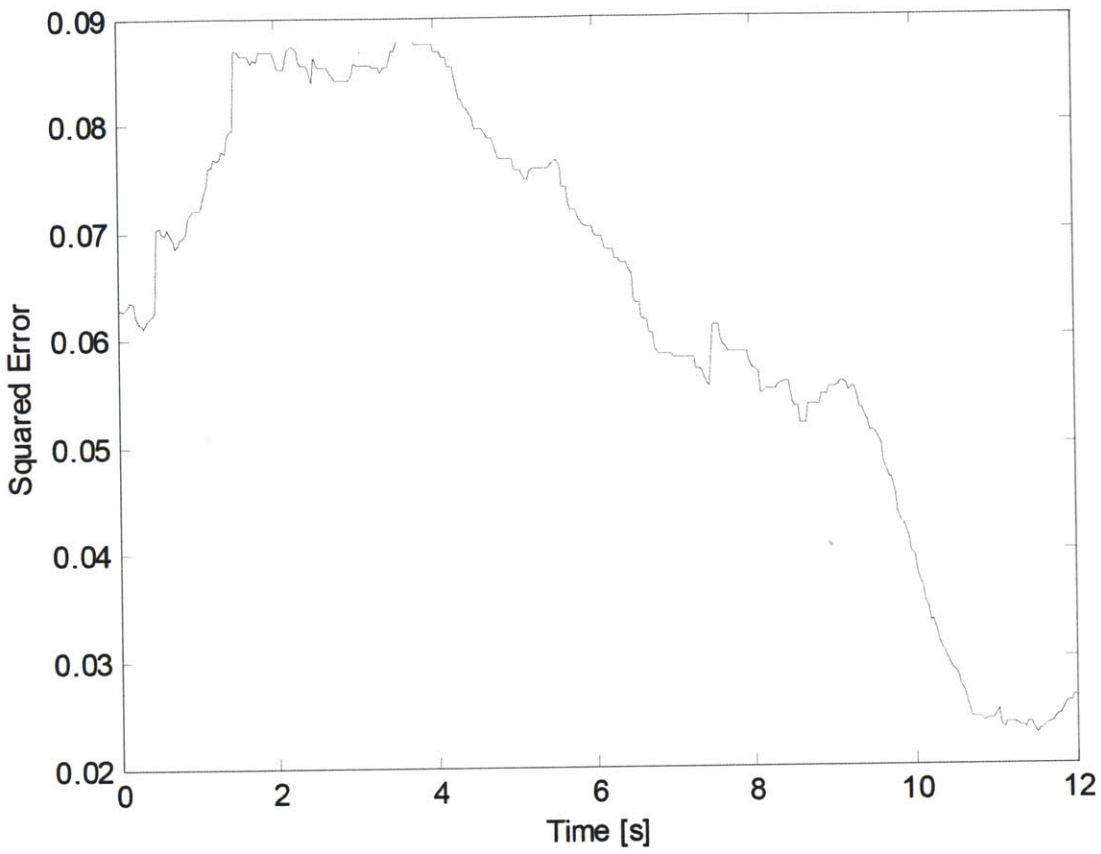

Figure 46 – Squared error of the EKF localization algorithm

As can be seen, the squared error is low.

As a comparison, the EKF was compared to two different methods of localizing the raft. On one extreme, the position of the raft was propagated through the model without the corrections from the measurements. In doing this, the model was initialized at the same point as the EKF, and the model was simulated according to the model seen in (66), using the same input thrusts and moments as those inputted into the EKF. On the other, the location of the raft was calculated directly from the model, using basic kinematics:

$$x_{kinematic} = d_{kinematic}\cos(\theta_{kinematic}) \tag{82}$$

$$x_{kinematic} = d_{kinematic}\cos(\theta_{kinematic}) \tag{83}$$

For this, only the signal strength V_{pp} and the angle measurement from the photodiode array at the ground station, $\theta_{pd,rec}$ were used. The calculations were made in the following manner:

$$\theta_{kinematic} = \theta_{pd,rov} \tag{84}$$

$$d_{kinematic} = -\sigma \ln\left(\frac{V_{pp}}{V_0}\right) \tag{85}$$

A comparison of these methods is shown in the following figure.

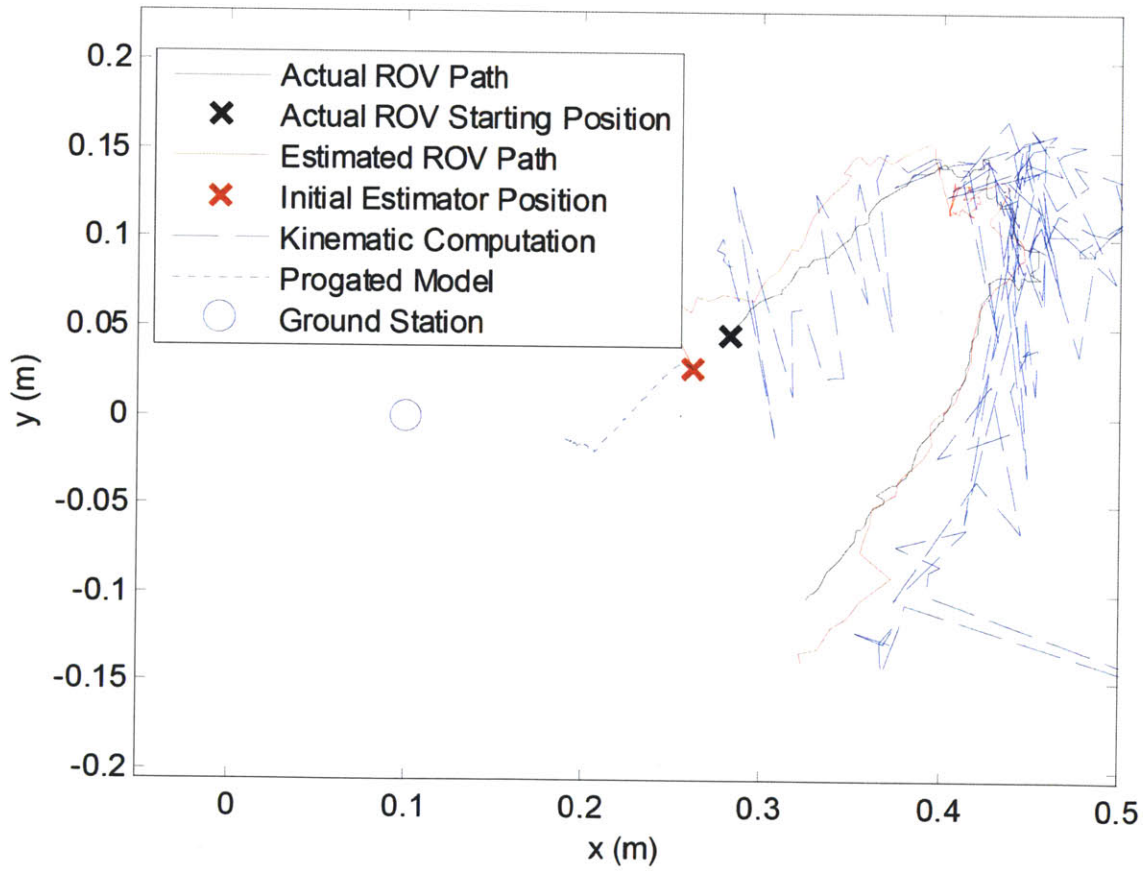

Figure 47 - A comparison of the various strategies for localizing the raft.

As can be seen, the EKF algorithm allows for the noise from the measurements (seen in the kinematic calculation, from (82)-(85)) and the built-up error from the pure model propagation to be removed, leaving a fairly accurate estimate of the location of the raft.

Lastly, as a last evaluation of the localization algorithm , we examined how well the raft was able to "point" back to the ground station. This is the intent of implementing the proportional control seen in (81). The actual orientation was measured using a video camera mounted above the test tank. The results follow.

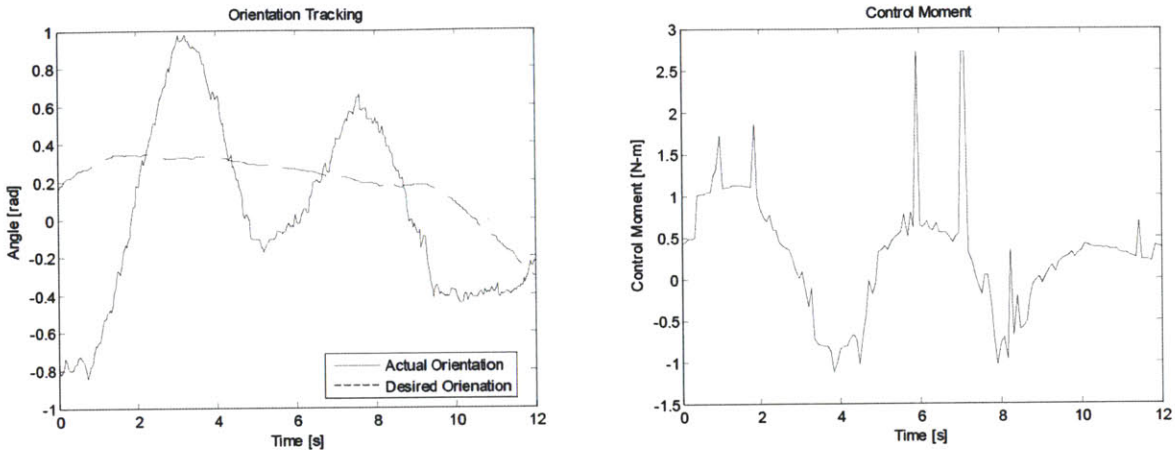

Figure 48 – Performance of the control system used to "point" the LED aboard the raft back to the ground station.

As shown in this figure, the basic proportional control system was able to point the LED aboard the raft back to ground, albeit with an oscillatory nature to the response. This is likely caused by the simple control system. To remove these oscillations, a more complex control system would be required, which is a topic of future study. This test acts as a proof of concept of the ability to point the LED aboard the raft back to ground.

In addition, we can show the accuracy of how well this heading error was estimated. This was done by comparing the actual heading of the raft to the estimated heading of the raft, seen in the following figure.

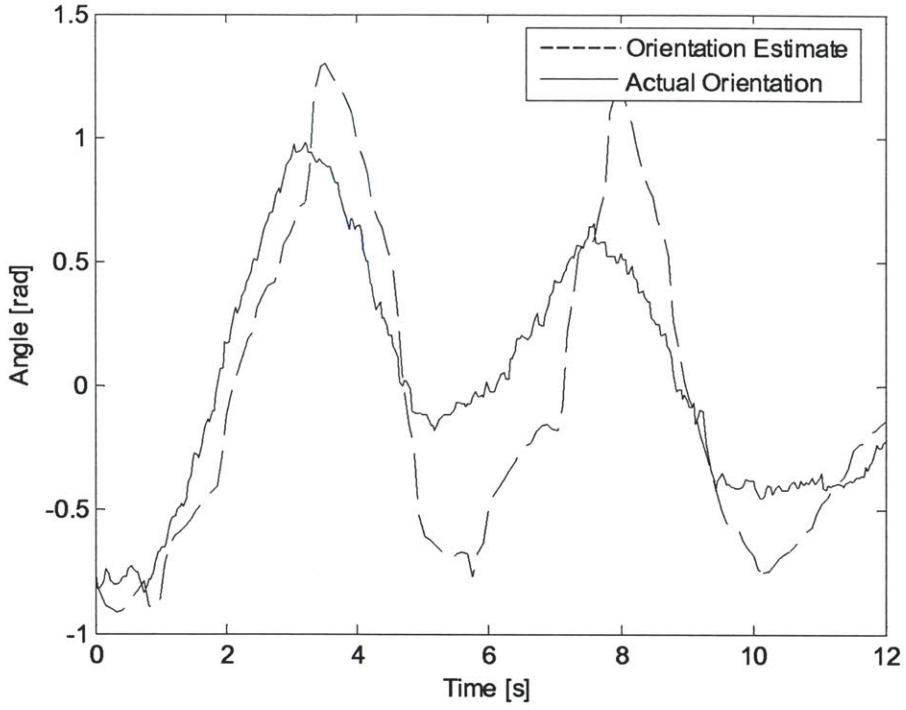

Figure 49 – Performance of the EKF localization in terms of estimating the orientation of the raft.

As can be seen, the EKF is able to estimate, with some error, the orientation of the raft. This will be an important feedback signal when more complex feedback control is implemented.

3.4.6. Conclusions from the Planar Localization Algorithm

As these simulations and experiments show, the localization algorithm presented is successful in demonstrating an expansion of the dual-use communication and localization system which is the focus of this portion of this thesis. In these tests, not only was the ROV successfully localized, in both experiment and simulation, but the dual use nature of the system was demonstrated as well. This is because, while the ROV was localized, the ROV was being piloted using the optical communication link.

Further work will include piloting the ROV using video data relayed over the communication link, as well as improving on the feedback control used to point the optical modem on the ROV back to the ground station. In addition, this localization will be modified for an environment where direct line of sight is impossible, for example in the various turns of the piping system. Fortunately, these pipes are made of stainless steel, and thus are reflective. As

such, the optical signal will reflect along these pipes, and localization will be attempted using this reflected signal.

Chapter 4

Conclusion

This thesis presents two bodies of work, each with the goal of designing a safe and reliable underwater Remotely Operated Vehicle (ROV) for use in the inspection of nuclear reactors. This was done with the overall design goal of piloting a wireless robot with a camera throughout the reactor and the associated piping systems of the primary cooling cycle of a Pressurized Water Reactor (PWR).

The first body of work consists of the design, modeling and control of an ROV with a spherical outer shape and camera fixed to the outer hull. Because of this design, the robot is called the Eyeball ROV. The novelty of this robot arises from its ability to enact orientation control with minimal translation, thus being able to turn in place. This is important because it contributes to safety of inspection. In addition, this is done using completely internal components, which allows the robot to have a smooth spherical shape. This is less likely to collide with obstacles in the piping systems of the reactor, and as such contributes to the safety of the operation of the vehicle. The ROV uses a two-axis gimbal in order to enact orientation control by changing the stable point of the systems as a whole. This was done by shifting the center of mass of the system, in what is called an Eccentric Mass Steering System. A simplified model was developed for this system, and was tested in simulation. Using basic proportional

control, the ROV was controlled to follow rotational commands, which directly correspond to the operator panning and tilting the camera affixed to the ROV. A proof of concept ROV was built, and the control system and actuation scheme were tested in experiment. These tests were hindered by the presence of a tether. Future work will consist of fabricating a wireless ROV with this eccentric mass steering system to further test control of this ROV. In addition, a full order model may be required for application of more complex control systems.

The second body of work was concerned with the wireless communication of the ROV with a ground station, where an operator would pilot the ROV. Due to range constraints in water of existing radio-frequency communication systems, and bandwidth limitations of acoustic modems, a visible light based communications system was used due to an ability for high bandwidth and extended ranges.

The primary focus of this thesis, however, was the development of a dual-use system for both communication and localization. Specifically, this is a system that uses the visible light signal to both relay data and compute the location of the ROV relative to some ground station, where an operator would control the robot. This is important for two reasons. The first is the general importance of localization for control of mobile robots. The second, and most immediately applicable, is the necessity for line of sight in optical communication systems. If the robot can be localized, then an LED or photodiode can be more reliably "pointed" to and from the robot. This contributes to the overall robustness of the communication system.

First, a kinematic model was presented for estimating orientation of the ROV. The estimation algorithm consisted of a linear Kalman Filter. This was tested experimentally. Expanding this to planar motion of the ROV, a dynamic model was used in order to estimate the position in the plane as well as the orientation of the ROV. This localization was done using an Extended Kalman Filter (EKF), since the dynamics of the ROV were non-linear. This was first tested in simulation to ensure the performance of the algorithm. Then, an experiment was developed using a raft which floated on the surface of the water in place of the ROV. With this hardware, we were able to successfully localize the raft. Further work will be concerned with extending this localization to three dimensional motions.

With these two bodies of work we present design and verification of three key components of this nuclear inspection robot: orientation control, communication, and

localization. The novelty of the research is two-fold. First, the design of the ROV (i.e. the spherical eyeball robot) is novel, and the method for orientation control is a new design based on existing strategies (i.e. continuous rotation through displacement of the center of mass of the vehicle). The communication systems feature what have come to be standard optical modems. However the extension of this system to be a dual-use one, both for communication and localization, is to the best of our knowledge the first of its kind. Therefore, this thesis, along with presenting results showing the functionality of these strategies, presents technologies that form a contribution to underwater ROV design and underwater robot localization. Future work will center on integrating these technologies into a unified prototype.

References

[1] Science Daily. (2007, October) Science Daily. [Online]. http://www.sciencedaily.com/releases/2007/10/071023103052.htm

[2] United States Nuclear Regulatory Commision. (2011, March) [Online]. http://www.nrc.gov/reactors/operating/map-power-reactors.html

[3] USNRC Technical Training Center, "Pressurized Water Reactor (PWR) Systems," United States Nuclear Regulatory Commission, Reactor Concepts Manual.

[4] United States Nuclear Regulatory Commision. (2011, May) [Online]. http://www.nrc.gov/reactors/operating/ops-experience/buried-piping-activities.html

[5] R Hardies et al., "NRC Action Plan - Revision 1," United States Nuclear Regulatory Commission, TAC NO. ME3939, 2010.

[6] M Odakura, Y Kometani, M Koike, M Tooma, and Y Namashima, "Advanced Inspection Technologies for Nuclear Power Plants," Hitachi, 2009.

[7] M Tooma and Y Nagshima, "Hitachi Inspection Technology for Nuclear Power Plant," *E-Journal of Advanced Maintenance*, 2009.

[8] Gabriel Ogundele. (2011, March) Kinectrics - Nuclear Buried Piping: Out of Sight, Out of Mind? [Online]. http://blog.kinectrics.com/nuclear-energy/nuclear-buried-piping-out-of-sight-out-of-mind-2/

[9] L Briones, P Bustamante, and M Serna, "Robicen: A wall-climbing pneumatic robot for inspection in nuclear power plants," *Robotics and Integrated Manufacturing*, vol. 11, pp. 287-292, December 1994.

[10] L Rodriguez, T Sattar, and T Shang, "Underwater wall climbing robot for nuclear pressure vessel inspection," 2008.

[11] S.G. Roh, S.M. Ryew, J.H. Yang, and H.R. Choi, "Actively steerable in-pipe inspection robots for underground urban gas pipelines," in *IEEE International Conference on Robotics and Automation*, 2001, pp. 761-766.

[12] Changhwan Choi and Seungho Jung, "Pipe Inspection Robot with an Automatic Tracking System Using a Machine Vision," in *SICE-ICASE*, 2006, pp. 1285-1290.

[13] S Kim et al., "Application of Robotics for the Nuclear Power Plants in Korea,".

[14] Cho Byung-Hak et al., "KeproVt: underwater robotic system for cisual inspection of nuclear reactor internals," *Nuclear Engineering and Design*, vol. 231, pp. 327-335, 2004.

[15] Shinji Yamamoto, "Development of Inspection Robot for Nuclear Power Plant," in *IEEE Internation Conference on Robotics and Automation*, 1992.

[16] J. Barry Fallon, Steven B. Shooter, Charles F. Reinholtz, and S. William Glass, "URSULA: Design of an Underwater Robot for Nuclear Reactor Vessel Inspection," in *Robotics for Challenging Environments*, 1994.

[17] Norman Farr et al., "Optical Modem Technology for Seafloor Observatories," in *Oceans*, 2006, pp. 1-6, 18-21.

[18] Marek Doniec, Iuliu Vasilescu, Carrick Detweiler, Daniela Rus, and Mandar Chitre, "Aquaoptical: A Lightweight Device for High-Rate Long-Range Underwater Point-to-Point Communication," in *Oceans*, 2009.

[19] James Bales and Chryssostomos Chryssostomidis, "High-bandwidth, low-power, short-range optical communication underwater," in *9th International Symposium on Unmanned Untethered Submersible Technology*, 1995.

[20] John W Giles and Isaac N Bankman, "Underwater Optical Communications Systems," in *MILCOM*, 2005.

[21] Frank Hanson and Tojan Radic, "High Bandwidth Underwater Optical Communication," *Applied Optics*, vol. 47, January 2008.

[22] A Halme, J Suomela, T Schonberg, and Y Wang, "A spherical mobile micro-robot for scientific applications," in *ASTRA*, 1996.

[23] A H Javadi and P Mojabi, "Introducing August: a novel strategy for an omnidirectional spherical rolling robot," *Systems and Controls Letters*, vol. 23, pp. 395-402, 1993.

[24] Henry Stommel, "The Stommel Mission," *Oceanography*, pp. 22-25, April 1989.

[25] J. Sherman, R.E. Davis, W.B. Owens, and J. Valdes, "The autonomous underwater glider "Spray"," *IEEE Journal of Oceanic Engineering*, vol. 26, no. 4, pp. 437-446, October 2001.

[26] C.C. Eriksen et al., "Seaglider: a long-range autonomous underwater vehicle for oceanographic research," *IEEE Journal of Oceanic Engineering*, vol. 26, no. 4, pp. 424-436, October 2001.

[27] Panagiotis Tsiotras and James M. Longuski, "Spin-axis stabilization of symmetric spacecraft with two control torques," *Systems & Control Letters*, vol. 23, no. 6, pp. 395-402, December 1994.

[28] T I Fossen, *Guidance and Control of Ocean Vehicles*. Chichester, United Kingdom: John Wiley and Sons, 1994.

[29] Gianluca Antolleni, *Underwater Robots: Motion and Force control of Vehicle-Manipulator Systems (2nd Ed.)*, B Siciliano, O Khatib, and F Groen, Eds. New York, New York: Springer-Verlag, 2006.

[30] A I Korotkin, *Added Mass of Ship Structures*. New York, New ork: Springer-Verlag, 2009.

[31] Frank M White, *Fluid Mechanics (4th Ed.)*. Boston: CB Mcgraw Hill, 1999.

[32] Tarun K Podder, G Antonelli, and N Sarkar, "Fault-Accommodating Thruster Force Allocation of an AUV Considering Thruster Redundancy and Saturation," *Transactions on Robotics and Automation*, April 2002.

[33] Tarun K Podder, G Antonelli, and N Sarkar, "Fault Tolerant Control of an Autonomous Underwater Vehicle Under Thrust Redundancy: Simulation and Experiments," in *IEEE International Conference on Robotics and Automation*, 2000.

[34] Milica Stojanovic, "On the relationship between capacity and distance in an underwater acoustic communication channel," in *ACM International Workshop on Underwater Networks*, 2006, pp. 41-47.

[35] O V Kopelvich, "Optical Properties of Pure water in the 250-600nm range," *Optics and Spectroscopy*, vol. 41, no. 4, pp. 391-392, October 1976.

[36] Martin Chaplin. (2011, June) Water Absorption Spectrum. [Online]. http://www.lsbu.ac.uk/water/vibrat.html

[37] S Karp, "Optical Communications Between Underwater and Above Surface (Satellite) Terminals," *IEEE Transactions on Communications*, vol. 24, no. 1, pp. 66-81, January

1976.

[38] Shlomi Arnon, "Underwater optical wireless communication," *Journal of Optical Engineering*, vol. 49, January 2010.

[39] B. Cochenour, L. Mullen, and A. Laux, "Spatial and temporal dispersion in high bandwidth underwater laser communication links," in *Military Communications Conference*, 2008.

[40] C L Lam, K T Wong, and Y I Wu, "The TOA-distribution of multipaths between an omni-directional transceiver and a mis-oriented directional transceiver," *IEEE Transactions on Communications*, vol. 58, no. 4, pp. 1042-1047, April 2010.

[41] S Krupinski, F Maurelli, G Grenon, and Y Petillot, "Investigation of autonomous docking strategies for robotic operation on intervention panels," in *Oceans*, 2008, pp. 1-10.

[42] M Carreras, P Ridao, R Garcia, and T Nicosevici, "Vision-based localization of an underwater robot in a structured environment," in *IEEE International Conference on Robotics and Automation*, 2003.

[43] R Garcia, J Puig, P Ridao, and X Cufi, "Augmented state Kalman filtering for AUV navigation," in *IEEE International Conference on Robotics and Automation* , 2002.

[44] F Schill, U Zimmer, and J Trumpf, "Visible Spectrum Optical Communication and Distance Sensing for Underwater Applications," in *ACRA*, 2004.

[45] L Yan, I M Chen, Z Guo, Y Lang, and Y Li, "A Three Degree-of-Freedom Optical Orientation Measurement Method for Spherical Actuator Applications," *Transactions on Automation Science and Engineering*, vol. 8, no. 2, pp. 319-326, April 2011.

[46] R E Kalman, "A New Approach to Linear Filtering and Prediction Problems," *ASME Journal of Basic Engineering*, vol. 82, pp. 99-108, March 1960.

[47] P. Bahl and V.N. Padmanabhan, "RADAR: an in-building RF-based user location and tracking system," in *Joint Conference of the IEEE Computer and Communications Societies*, 2000.

[48] N. Bulusu, J. Heidemann, and D. Estrin, "GPS-less low-cost outdoor localization for very small devices," *Personal Communications*, vol. 7, no. 5, pp. 28-34, October 200.

[49] Kamin Whitehouse, Chris Karlof, and David Culler, "A practical evaluation of radio signal strength for ranging-based localization," *SIGMOBILE Mob. Comput. Commun. Rev.*, vol. 11, no. 1, pp. 41-52, January 2007.

[50] Ian C Rust and H Harry Asada, "The Eyeball ROV: Design and Control of a Spherical Underwater Vehicle Steered by an Internal Eccentric Mass," in *IEEE Int. Conference on Robotics and Automation*, 2011.

[51] R E Kalman, "On the General Theory of Control Systems," in *IFAC*, 1960.

[52] Ian C Rust and H Harry Asada, "A Dual-Use Visible Light Communication and Orientation Estimation System for Underwater robots," in *ASME Dynamic systems and Control Conference*, 2011.

[53] H Okihana, K Iwata, and Y Miwa, "Remote Controlled Inpection Robot for Nuclear Facilities in Underwater Environment," in *ASME*, 2009, p. 99.

Chapter 5

Appendices

5.1. Appendix 1 – Physical Parameters of the Eyeball ROV

Table 6 - Physical Parameters and Values of the Eyeball ROV

Parameter	Description	Quantity
L	distance from the center of buoyancy to the center of mass	3.5 mm
D	diameter at which the propeller thruster are mounted	12 cm
$\forall$	volume of ROV	9.05×10^{-4} m^3
A	frontal area of the ROV	11.3×10^{-3} m^2
m	mass of the ROV	0.815 kg
m_{weight}	mass of the eccentric steel weight	0.550 kg
J_x	inertia of ROV about the x-axis in the inertial frame	7.81×10^{-4} kg·m^2
J_y	inertia of ROV about the y-axis in the inertial frame	7.81×10^{-4} kg·m^2
J_z	inertia of ROV about the z-axis in the inertial frame	7.78×10^{-4} kg·m^2
$J_{x,weight}$	inertia of the inner weight about the x-axis in the inertial frame	1.49×10^{-4} kg·m^2
$J_{y,weight}$	inertia of the inner weight about the y-axis in the inertial frame	1.49×10^{-4} kg·m^2
$J_{z,weight}$	inertia of the inner weight about the z-axis in the inertial frame	1.42×10^{-4} kg·m^2
$D_{x,motor}$	damping coefficient for the roll gimbal motor	0.5 N·s
$D_{x,motor}$	damping coefficient for the pitch gimbal motor	0.5 N·s
$c_{d,lin}$	Linear drag coefficient	0.001
$c_{d,rot}$	Rotational drag coefficient	0.002
$c_{d,lift}$	lift coefficient	0.2

5.2. Appendix 2 – Physical Parameters used in Simulation of the Localization Algorithm

Table 7 - Physical Parameters used in the Localization Algorithm Simulation

Parameter	Description	Quantity
m	mass of the ROV	1.315 kg
C_d	linear drag coefficient	0.758
C_{rot}	rotational drag coefficient	8.37×10^{-3}
I_{ROV}	moment of inertia of the ROV	0.036 kg·m^2
σ	attenuation coefficient of signal strength	$5.986\times10^{-3}\frac{1}{m}$

5.3. Appendix 2 – Physical Parameters used in Experiments of the Localization Algorithm

Table 8 - Physical Parameters used in the Localization Algorithm Experiments

Parameter	Description	Quantity
m	mass of the ROV	1.315 kg
C_d	linear drag coefficient	0.758
C_{rot}	rotational drag coefficient	8.37×10^{-3}
I_{ROV}	moment of inertia of the ROV	0.036 kg·m^2
σ	attenuation coefficient of signal strength	$10.75\frac{1}{m}$